IMAGE ANALYSIS METHODS FOR BRAIN TUMOR TREATMENT FOLLOW-UP

by
Andaç Hamamcı

Submitted to the Graduate School of Engineering and Natural Sciences
in partial fulfillment of the requirements for the degree of
Doctor of Philosophy
in Electronics Engineering

Sabancı University
August 2013

Image Analysis Methods for Brain Tumor Treatment Follow-up

APPROVED BY

Assoc. Prof. Dr. Gözde ÜNAL ....
(Thesis Supervisor)

Prof. Dr. Aytül ERÇİL ....

Prof. Dr. Ali Rana ATILGAN ....

Assoc. Prof. Dr. Hakan ERDOĞAN ....

Assist. Prof. Dr. Devrim ÜNAY ....

DATE OF APPROVAL: ....

dedeme

Acknowledgements

I would like to thank to my supervisor Assoc.Prof.Dr. Gözde Ünal for her focused and enthusiastic support and guidance, interest in transferring knowledge and maintaining excellent research conditions.

I would like to thank to the members of the thesis committee Prof.Dr. Aytül Erçil, Prof.Dr. Ali Rana Atılgan, Assoc.Prof.Dr. Hakan Erdoğan, Assist.Prof.Dr. Devrim Ünay and Assoc.Prof.Dr. Selim Balcısoy for their time and attention devoted; and also valuable comments and advices.

I would like to thank to Prof.Dr. Kayıhan Engin, Dr. Kutlay Karaman, Nadir Küçük, Radiation Oncology and Radiology departments of Anadolu Health Center (ASM) for sharing their clinical knowledge and the data.

I would like to thank to The Scientific and Technological Research Council of Turkey (TÜBİTAK Project No: 108E126), European Commission Seventh Framework Programme (EC-FP7 Project No: PIRG03-GA-2008-231052) and Turkish Academy of Sciences (TÜBA-GEBIP) for their partial funding of the thesis.

I would like to thank to my colleagues in our research group Süheyla Çetin, Ali Demir, Timur Aksoy, Rıza Alp Güler, Devran Uğurlu for their support, help and comments. I would like to thank to Övünç Uzun and Ahmet Erdem for their efforts on user interface development and GPU implementations.

I would like to thank to Drs.S.Warfield and N.Archip at Harvard Computational Radiology Laboratory for sharing the tumor dataset.

I would like to thank to Drs. Bjoern Menze (ETH Zurich), Andras Jakab (ETH Zurich / University of Debrecen), Stefan Bauer (University of Bern), Mauricio Reyes (University of Bern), Marcel Prastawa (University of Utah) and Koen Van Leemput (Harvard Medical School, Technical University of Denmark) for providing the BraTS dataset.

I would like to thank to my smart and sweet daughter, Irmak, for her emotional support.

IMAGE ANALYSIS METHODS FOR BRAIN TUMOR TREATMENT FOLLOW-UP

Andaç Hamamcı

EE, PhD Thesis, 2013

Thesis Supervisor: Gözde ÜNAL

Keywords: Brain tumor, Radiosurgery, Radiotherapy, Registration, Segmentation, Follow-up change detection in longitudinal MRI, Tumor mass effect

Abstract

Assessment of the progression of the tumors in current clinical practice is based on maximum diameter measurements, which are related to the volumetric changes. With the advent of the spatially localized radiotherapy techniques (i.e. Cyberknife, IMRT, Gammaknife, Tomotherapy) not only the volumes of the tumors but also the geometric changes need to be considered to measure the effectiveness and to improve the applied therapy.

In this thesis, image analysis techniques are developed for assessment of the changes of the tumor geometry between MRI volumes acquired after and before the therapy. Three main parts of the thesis are: Segmentation of brain tumors on MRI; change quantification in temporal MRI series of brain tumors; and deformable registration of brain MRI volumes with tumors.

The results obtained by the developed semi-automatic brain tumor segmentation method, Tumor-cut, are comparable with those of state-of-the-art techniques in the field. The quantification of tumor evolution using the invariants of the Lagrange strain tensor provide measures that are more correlated with the clinical outcome than the volumetric measures. The deformable registration of longitudinal data provides a novel framework to study brain deformations, in vivo, and more accurate assessment of the changes.

BEYİN TÜMÖRÜ TEDAVİ TAKİBİ İÇİN GÖRÜNTÜ ANALİZİ YÖNTEMLERİ

Andaç Hamamcı

EE, Doktora Tezi, 2013

Tez Danışmanı: Gözde ÜNAL

Anahtar Kelimeler: Beyin tümörü, Radyocerrahi, Radyoterapi, Çakıştırma, Bölütleme, MR değişim takibi, Tümör itme etkisi

Özet

Günümüz klinik uygulamalarında, tümörlü dokuların takibi, hacim değişimini yansıtan çap ölçümleriyle yapılmaktadır. Ancak, IMRT, CyberKnife, GammaKnife, Tomoterapi gibi lokalize radyoterapi tekniklerinin gelişimine paralel olarak, uygulanan terapinin başarısının değerlendirilmesi ve geliştirilmesi için lokal geometrik değişimlerin de değerlendirilmesine ihtiyaç duyulmaktadır.

Bu tezde, terapi öncesi ve sonrasında alınan MR hacimleri arasında tumor geometrisindeki değişimlerin değerlendirilmesine yönelik görüntü analizi teknikleri geliştirilmiştir. Tez üç ana parçadan oluşmaktadır: Beyin tümörlerinin MR görüntülerinde bölütlenmesi; MR serilerinde tümör değişiminin kuantifikasyonu; tümörlü beyin MR görüntülerinin çakıştırılması.

Geliştirilen yarı-otomatik beyin tümörü bölütleme yöntemi literatürdeki en başarılı tekniklere benzer sonuçlar sağlamaktadır. Tümör değişiminin Lagrange gerilme tensörü değişmezleri kullanılarak elde edilen ölçütlerle değerlendirmesi, hacim ölçütlerine kıyasla, klinik sonuçlarla daha iyi örtüşen sonuçlar sağlamaktadır. Farklı zamanlarda alınan MR görüntülerinin biçimlenebilir çakıştırması beyin deformasyonlarının canlı dokuda incelenmesini sağlayan bir çerçeve sunmakta ve değişimlerin daha hassas bir şekilde değerlendirilmesini sağlamaktadır.

Table of Contents

List of Figures

List of Tables

Chapter 1

Introduction

1.1 Brain Tumors

Brain tumors are a set of neoplasms, which are caused by uncontrolled cell proliferation, and do not necessarily arise from brain tissue (e.g., meningiomas and lymphomas) [3, 4]. World Health Organization (WHO) classification of Central Nervous System (CNS) tumors is based on the identification of different histopathologic groups and includes a scale of malignancy, ranging from grade I benign forms to grade IV forms with rapid growth and poor prognosis [5].

Approximately 40% of intracranial neoplasms are metastatic, which originate most frequently from lung, breast, melanoma, renal and colon cancers, whereas remaining are primary brain tumors. Gliomas are the most frequent primary brain tumors in adults and account for 70% of adult malignant primary brain tumors [4]. Nearly 50% of the gliomas are WHO grade IV tumors, which are called glioblastoma multiforme (GBM), exhibiting very rapid growth, with an average survival time of one year. Meningiomas, which arise from meningothelial cells that form the external membranous covering of the brain, are the most common extra-axial intracranial neoplasms, which account for 15-20% of intracranial neoplasms [3, 4].

The symptoms of a brain tumor depend mainly on its location and its size and consequently on the function of areas involved by the tumor, with a variety of nonspecific symptoms typical of a mass growing inside the skull with increased intracranial pressure. Common symptoms are persistent headache, nausea, vomiting (usually morning), disorders of retina like papilledema caused by the dilatation of cerebral vessels, focal deficit (hemiparesis, hemianesthesia, hemianopsia, diplopia, aphasia) and seizures due to tumor irritation effect (present up to one third of patients); moreover nonspecific neurologic symptoms such as clouding of consciousness and personality changes [6].

Ionizing radiation is the only unequivocal risk factor that has been identified for glial and meningeal neoplasms. Irradiation of the cranium, even at low doses, can increase the incidence of meningiomas by a factor of 10 and the incidence of glial tumors by a factor of 3 to 7 with a latency period of 10 years to more than 20 years after exposure. No other environmental exposure or behavior has been clearly identified as a risk factor. The use of cellular telephones, exposure to high-tension wires, the use of hair dyes, head trauma, and dietary exposure to N-nitro sourea compounds or other nutritional factors have all been reported to increase the risk of brain tumors; however, the data are conflicting and unconvincing [3].

The treatment of brain tumors is complex and depends on several factors such as histologic type, location and extension, age and general conditions of the patient. Brain tumors can be treated with surgery, radiation therapy (RT) and chemotherapy, often in combination, in relation to the needs of patient [7].

1.2 MR Imaging of the Brain Tumors

Although computed tomography (CT) is also used to diagnose the brain tumors, it can miss structural lesions such as nonenhancing tumors. Therefore, if a brain tumor is a diagnostic consideration, MRI with gadolinium enhancement is the test of choice [3].

MRI makes it possible to produce markedly different types of tissue contrast by varying excitation and repetition times, which makes it a very versatile tool for imaging different structures of interest. In current clinical routine, different MRI sequences are employed for the diagnosis and delineation of tumor compartments [4]. The brain tumor MR protocol, with and without contrast agent administration should include T2-weighted and T2-weighted fluid-attenuated inversion recovery (T2-FLAIR) sequences, best performed in 3D, generally in axial or coronal views, and T1-weighted sequences with and without contrast enhancement [6].

In MR imaging of glioblastoma, the solid part of the tumor shows hypointense signal in T1-weighted sequences and hyperintense in T2, with higher signal in areas of greater cellularity. Necrotic areas, which always appear hyperintense in T2, may be hypo-, iso- or hyperintense in T1 due to products of protein or hemoglobin degradation. Enhancement after administration of contrast medium is usually intense and irregular at the tumor margins and identifies the cellular proliferation component of the tumor. Punctate and serpiginous areas of no signal caused by flow associated with neovascularization are common. These newly formed pathologic vessels are devoid of blood-brain barrier (BBB), which explains both their marked enhancement and perilesional vasogenic edema, due to the passage of fluid in the extracellular space [6].

1.3 Current Medical Practice and Clinical Motivation

1.3.1 Radiotherapy Treatment

Radiation therapy (RT) is a nonsurgical treatment that uses radiation to eradicate tumor or to restrict its growth. For some cancer types particularly sensitive to radiation, RT often in combination with chemotherapy may be the only therapeutic approach required. In other cases, RT is used in combination with surgery to remove any residual tumor not removed during surgery. RT can also be used in nonoperable tumors to reduce metastatic spread or relieve symptoms.

Radiation can kill cells or block their ability to proliferate. Although, they act both on tumor cells and normal cells, tumor cells are more sensitive to radiation due to high proliferation rate, so it is possible to protect healthy cells by applying the dose as fractions (i.e. Intensity Modulated Radiotherapy). On the other hand, stereotactic radiosurgery (SRS) consists in the administration of highly collimated beams of radiation through multiple non-coplanar arcs that intersect at a single point (i.e. Cyber-knife, Gamma-knife etc.). This method involves the administration of the entire dose in a single session with a rapid fall of the dose to surrounding tissue. Stereotactic radiosurgery is feasible for small unifocal tumors (up to 4 cm), metastases, tumors which are unreachable by surgery or recurrence especially in patients already receiving the maximum tolerable radiation dose.

Generally brain cells are very resistant to irradiation, while other cell types (bone marrow cells, germinal cells, epithelium lining hollow organs) are very sensitive, which is why the approach is to restrict the radiotherapeutic target volume as much as possible [6]. Advanced radiotherapeutic devices allow the delivery of a high dose to a precisely defined target volume, whereas keeping the dose on normal tissue at minimum. Diagnostic imaging with CT and MR is essential for defining the target volume and planning treatment. MRI is used to define the target volume, which is the pathologic tissue irradiated with high dose, and organs at risk, which are protected from the high dose radiation. Planning CT scan is still necessary for it provides the attenuation coefficient map and serves as a reference for registration during the therapy.

In planning radiotherapy treatment of brain tumors, first, the MR images acquired with different sequences are registered to the contrast enhanced T1 images. Then each MR image is transformed to CT space by applying the transformation obtained by registering contrast enhanced T1 image to the CT image. The target volumes and organs at risk (OAR) are contoured manually or interactively on MRI using computer tools. In radiotherapy, the planning target volume (PTV) is defined in 3 stages: The gross tumor volume (GTV) is defined as the surgical cavity and any residual diseased tissue visualized with contrast enhancement in T1-weighted images of postoperative MR; the clinical target volume (CTV) is defined as GTV plus an expansion margin of 2 cm where there may be infiltration of tumor cells; the PTV is represented by CTV plus an expansion margin of 1 cm [6]. The treatment plan is determined on the CT image depending on the type of the therapy and tumor; and controlled by optical tracking or registering x-ray scans acquired during treatment. A similar procedure is applied in radiosurgery (i.e. CyberKnife), except with a more conservative and precise definition of the target volume (PTV=GTV), due to its less differentiation of tumor/healthy cells.

1.3.2 Image Analysis for the Radiotherapy Treatment

As described above, advanced image analysis techniques are involved in different stages of the radiotherapy treatment of brain tumors. Rigid/affine registration of multi-modal MR images to CT images, having different contrast characteristics, is performed. Rigid/affine registration using normalized cross correlation or mutual information based algorithms are quite mature and are applied confidently to the problem. Segmentation of the gross tumor volume (GTV), surrounding edema and necrosis within GTV, is a widely studied problem in the literature, which aims to reduce the intra-observer variability and workload in treatment planning.

Full-automatic tumor segmentation methods, commonly based on machine learning [8], require large training samples, and may miss "unlearned" heterogeneous structures. They also do not use the information provided by the radiological examination, e.g. the volume of interest (VOI) and sampling from the tumor tissue through line diameter measurements. Semi-automatic methods are more user-friendly and appropriate to the clinical workflow, where the clinician wants to interact with the segmentation process. The challenge in MR tumor segmentation is to develop highly accurate and precise algorithms which are robust to highly heterogeneous tumor characteristics. In this thesis, the brain tumor segmentation problem, which is a part of the planning stages of radiotherapy as well as radiosurgery, is addressed, both in a mono-modal and a multi-modal setting.

1.3.3 Tumor Follow-up

The advent of MRI scanning protocols has allowed accurate follow-up of tumor growth through volumetric measurements. Interpretation of the radiological evolution of the tumor appears of utmost importance for therapeutic management, especially for low-grade glioma. Indeed, patients are most of the time asymptomatic (except in the case of epilepsy) during the low-grade phase, and the tumoral evolution is only monitored by MRI follow-up, both prior and after treatment. However, such information about the tumor dynamics is usually not fully integrated with the therapeutic strategy, and the assessment of the tumor evolution is still limited to qualitative descriptions (recurrence, progression, regression, stability)[9].

The neuroradiologic follow-up protocol in treated patients usually includes the following MR examinations:

- within 2-3 days after surgery to evaluate the radicality of surgery;
- 30 days after surgery (often the first follow-up examination);
- 30 days after completing treatment;
- every 3 months (high-grade gliomas) and every 6 months (low-grade gliomas) to evaluate tumor growth.

After treatment, it is necessary to wait some time before evaluating the results of RT: during this period, in fact, tumor cells damaged during the course of treatment undergo apoptosis. Often this process produces a degree of edema which can cause symptoms similar to cancer and which in radiologic imaging can simulate tumor growth [6].

In tumor follow-up studies, the most widely used criteria for assessing response to therapy in high-grade gliomas are based on two-dimensional tumor measurements which is the product of the maximal cross-sectional enhancing diameters (the Macdonald Criteria) [10, 11]. Currently, one-dimensional tumor measurements, which were first introduced in “The Response Evaluation Criteria in Solid Tumors” (RECIST), have become the standard criteria to determine response. The Response Assessment in Neuro-Oncology Working Group (RANO), an international effort to develop new standardized response criteria for clinical trials in brain tumors, considers also the non-enhancing tumors [12].

Limitations of two dimensional measurements include the difficulty of measuring irregularly shaped tumors, interobserver variability, the lack of assessment of the nonenhancing component of the tumor, lack of guidance for the assessment of multifocal tumors, and the difficulty in measuring enhancing lesions in the wall of cystic or surgical cavities because the cyst/cavity itself may be included in the tumor measurement. Given the limitations of two-dimensional tumor measurements, there is significant interest in volumetric anatomic assessment. The use of volumetric assessment would allow more accurate determination of the contrast-enhancing and nonenhancing volumes and overcome the limitations of two-dimensional measurements of lesions surrounding a surgical cavity [12].

Furthermore, with the advent of the spatially localized radiotherapy techniques (i.e. Cyberknife, IMRT, Gammaknife, Tomotherapy) not only the volumes of the tumors but also the geometric changes need to be considered to measure the effectiveness and to improve the applied therapy.

An accurate determination of the actual tumor evolution requires full 3D segmentation on digital images. Manual segmentation by an expert is still considered as the reference method, but is a time consuming task with high inter and intra-observer variability[9]. Konukoglu et. al. suggested a registration method for monitoring slowly evolving meningiomas, which performed semiautomatic tumor segmentation, non-rigid registration and change detection consecutively [13]. They argued that their volume-change measurements were less user-biased than manual measurements.

1.3.4 Image Analysis for the Tumor Follow-up

Computational methods used in tumor follow-up usually involve registration, segmentation and change quantification steps. Three different image registration problems arise as: intra-patient multi-modal registration at a time; longitudinal registration of images; inter-patient spatial normalization of brain tumor images to a brain atlas. Spatial normalization is commonly used for atlas-based segmentation [14] or constructing statistical tumor atlases [15, 16]. Intra-patient multi-modal MR registration is a common problem and can be solved successfully by a rigid registration algorithm using mutual information based similarity measure. However, for the longitudinal registration problem, not only the change of the appearance of the tumor in time, but also the deformation of the surrounding healthy tissue due to the mass effect of the tumor should be considered. This would require a deformable registration of the volumes to obtain a proper correspondence. Although, the inter-patient spatial normalization of tumor images also requires a deformable registration to be employed, the deformation in this case is not only due to the well defined mechanical effects but also includes interpersonal anatomical variability. Furthermore, the presence of a tumor in images represents a challenge for atlas registration algorithms:

the assumption of an intensity relationship between homologous structures does not hold, as the presence of a tumor in the image changes the MR signal in invaded areas. The initial approach to tackle this problem consisted in discarding the tumor region from the similarity criteria [17]. Another more sophisticated approach employs tumor growth simulations to generate a similar tumor on the atlas image [15, 18].

The problem of segmentation of the tumors on multi-modal MR images is similar to radiotherapy planning as described in 1.3.2. Another open problem in follow-up is the quantification and visualization of the changes, locally. The challenge here is both to understand the clinical needs and develop mathematical techniques to meet those requirements.

1.4 Thesis contributions and Overview

In this thesis, image analysis techniques are developed for treatment planning and assessment of the changes of the tumor geometry between MRI volumes acquired after and before the therapy. Three main parts of the thesis are: Segmentation of brain tumors on MRI, deformable registration of brain MRI volumes with tumors, and change quantification in temporal MRI series of brain tumors. The outline of the thesis is as following:

In this Introduction chapter, current medical practice of radiotherapy treatment and follow-up of brain tumors; and related image analysis methods are summarized in general.

In Chapter 2, a novel semi-automatic method, namely "Tumor-cut", to segment the core of the brain tumors on contrast enhanced T1-weighted MR images by evolving a level-set surface on a probability map obtained using cellular automata algorithm is presented. The Cellular Automata (CA) algorithm is re-examined to establish the connection of the CA-based segmentation to the graph-theoretic methods to show that the iterative CA framework solves the shortest path problem with a proper choice of the transition rule. The performance is evaluated qualitatively and quantitatively on synthetic and clinical datasets. This chapter appeared as a journal article in *IEEE Transactions on Medical Imaging, 31(3), pp.790-804, 2012.*

In Chapter 3, the ”Tumor-cut” method is extended to process multi modality MR images. The performance of the algorithm is evaluated on BraTS multi-modal brain tumor dataset available online. The results obtained are compared to the state-of-the-art techniques participated in the BraTS challenge. The work presented in this chapter appeared in *Proceedings of MICCAI-BRATS 2012 October 1st, Nice, France* and is in preparation for joint paper submission.

In Chapter 4, local tumor response criteria to quantify the change of the tumor are proposed based on the invariants of the Lagrange strain tensor. The value of the proposed technique is evaluated on synthetically created phantoms and clinical MR cases, compared to the volumetric changes and the radiological assessments. The work presented in this chapter appeared in the *European Society of Magnetic Resonance in Medicine and Biology (ESMRMB) Conference, 2012.*

A novel method for deformable registration of intra-patient longitudinal MR volumes, using hyper-elastic brain deformation models, is presented in Chapter 5. Preliminary part of this work presented in this chapter appeared in the *Computational Biomechanics for Medicine, pp. 101-114, Springer, 2013* and the current version is in preparation for submission as a journal article.

The thesis is summarized in the last chapter and the methods developed are discussed, providing the possible future directions.

Chapter 2

Tumor-Cut: Segmentation of Brain Tumors on Contrast Enhanced MR Images for Radiosurgery Applications [1]

2.1 Introduction

Segmentation of brain tissues in gray matter[19], white matter[20], and tumor[21] on medical images is not only of high interest in serial treatment monitoring of "disease burden" in oncologic imaging, but also gaining popularity with the advance of image guided surgical approaches. Outlining the brain tumor contour is a major step in planning spatially localized radiotherapy (e.g. Cyberknife, iMRT) which is usually done manually on contrast enhanced T1-weighted Magnetic Resonance Images (MRI) in current clinical practice. On T1 MR images acquired after administration of a contrast agent (gadolinium), blood vessels and parts of the tumor, where the contrast can pass the blood-brain barrier are observed as hyper intense areas. There are various attempts for brain tumor segmentation in the literature which use a single modality, combine multi modalities and use priors obtained from population atlases [9].

---

[1] This chapter appeared as a journal article in *IEEE Transactions on Medical Imaging, 31(3), pp.790-804, 2012.*

Modalities which give relevant information on tumor and edema/infiltration such as Perfusion Imaging, Diffusion Imaging or Spectroscopic Imaging provide lower resolution images compared to T1 or T2 weighted sequences, and the former are generally not preferable for geometric measurements. One of the main reasons to use multi-modality images such as T2 weighted MRI is to segment edema/infiltration region which is generally not observable in T1 images. Although the glial tumors infiltrate beyond the enhanced margin and edema/infiltration region might be of interest to fractionated radiotherapy in general, it is not possible to distinguish edema and infiltration, so usually this region is not included in primary target planning of radiosurgery, particularly in Cyberknife [22, 23, 24].

On the other hand, population atlases provide an important prior to improve segmentation by measuring the deviation from the normal brain. Deformable registration of brain images with tumor to the population atlas is an extremely challenging problem and still an active research area due to intensity variations around the tumor mainly caused by edema/infiltration, and the tumor mass effect, which also deforms the healthy tissue morphology [18]. In some studies, affine registration has been used for this purpose, however misalignment issues arise, especially where there is a large deformation of the brain structures [22, 25].

Comparison to the works in the literature that use different approaches and other image types is difficult as that would require the use of the same datasets by different groups with evaluation performed by similar measures. For this reason, only the results of some studies are given, instead of a detailed comparison. Although, using manual expert segmentations as the ground truth, different performance measures such as Dice Overlap, Jaccard Index, False Positive and Negative Volume Fractions (FPVF, FNVF) were used in the literature, (Dice) Overlap is used as a common measure for a comparison to previous methods here (see Appendix A for definitions and conversions). With their automatic, multi-modal, atlas based method, Prastawa et.al. have reported 86.7% average overlap on a small dataset of only 3 patients with an average 1.5 hour processing time [22]. In more recent studies, Menze et.al. reported 60% average overlap on 25 glioma patients and Gooya et.al. reported 74.5% average overlap on 15 glioma patients with about 6-14 hours of processing time [25, 18]. In contrast, Liu et.al. reported 95.6% average overlap on only a subset of well-performing 5 patients over a 10 patient dataset using fuzzy clustering on only FLAIR images. It should be noted that the latter method needs intensive user interaction and correction as 8.4 minutes per patient on the average [23].

The popular trend in the area, as in the aforementioned approaches, is to be able to combine information from different sources to obtain a better segmentation. However, attempts to develop better algorithms from the image processing perspective that work on a particular MRI protocol continue in parallel not only to obtain proper information from each channel to be combined, but also due to the practical need to routinely quantify tumors in a clinical environment [23]. Therefore, in this study, we focused on an efficient and robust segmentation of brain tumors on Contrast Enhanced T1-weighted MR images with minimal user interaction.

Region-based active contour models are widely used in image segmentation [26]. In general, these region-based models have several advantages over gradient-based techniques for segmentation, including greater robustness to noise. However, classical active contours had the problem of being “only as good as their initialization”, even when using level-set surfaces in 3D. Because the tumor class does not have a strong spatial prior, many small structures, mainly blood vessels, are classified as tumor as they also enhance with contrast. Ho et.al. used fuzzy classification of pre and post contrast T1 images to obtain a tumor probability map to evolve a level-set surface [27]. Liu et.al. have adapted the fuzzy connectedness framework for tumor segmentation by constructing a rectangular volume of interest selected through identifying the first and last slice of the tumor and specifying a set of voxels in the tumor region [23].

Interactive algorithms have become popular for image segmentation problem in recent years. Graph based seeded segmentation framework has been generalized such that Graph-cuts (GC) [28], random walker (RW) [29], shortest paths, and power watersheds [30] have been interpreted as special cases of a general seeded segmentation algorithm, which solves a minimization problem involving a graph’s edge weights constrained by adjacent vertex variables or probabilities. In [31], the connection between GC, RW, and shortest paths was shown to depend on different norms: L_1 (GC); L_2 (RW); L_∞ (shortest paths), in the energy that is optimized. Geodesic distances between foreground and background seeds were also incorporated into other shortest path-based segmentation algorithms by [32] and [33].

Although it was reported that the shortest paths and RW produce relatively more seed-dependent results, it can be argued that the global minimum of an image segmentation energy is worth as good as the ability of its energy to capture underlying statistics of images[34], and a local minimum may produce a solution closer to the ground truth than that of a global minimum. Hence, with good prior information provided as in the case of a seeded image segmentation problem, efficiently finding a good local minima becomes meaningful and worthwhile.

On the other hand, cellular automata (CA) algorithm motivated biologically from bacteria growth and competition, is based on a discrete dynamic system defined on a lattice, and iteratively propagates the system states via local transition rules. It was first used by Vezhnevets et.al. [35] (Grow-cut) for image segmentation, which showed the potential of the CA algorithm on generic medical image problems. However, Grow-cut was not designed for specific structures, such as tumors, which display heterogeneous content such as necrotic and enhancing tissue. Moreover, anatomic structures typically have relatively smooth boundaries, however, Grow-cut tends to produce irregular and jagged surface results, and only an ad-hoc way of smoothing was introduced.

In this chapter, we re-examine the CA algorithm to establish the connection of the CA-based segmentation to the graph-theoretic methods to show that the iterative CA framework solves the shortest path problem with a proper choice of the transition rule. Next, as our application is in the clinical radiosurgery planning, where manual segmentation of tumors are carried out on contrast enhanced T1-MR images by a radio-oncology expert, we modify the CA segmentation towards the nature of the tumor properties undergoing radiation therapy by adapting relevant transition rules. Finally, a smoothness constraint using level set active surfaces is imposed over a probability map constructed from resulting CA states. Following a brief background on seeded segmentation methods in Section 2.2, we present our framework for brain tumor segmentation in Section 2.3, and demonstrate its performance via validation studies on both synthetic, and radiation therapy planning expert-segmented data sets in Section 2.4, followed by conclusions in Section 2.5.

2.2 Background

2.2.1 Seeded Image Segmentation

Given an undirected graph $G = (V, E)$ with vertices $v \in V$ and edges $e \in E$, a weighted graph assigns a value w_{ij} (typically real and non-negative) to each edge e_{ij} between vertices v_i and v_j. In image segmentation problems, vertices are corresponding to image pixels, while edge weights are similarity measures between neighboring pixels based on image features (e.g. intensities). Each vertex v_i has an attribute x_i, which is an indicator of the probability of a label (e.g. a foreground and a background label). With the foreground F and background B seeds supplied by the user, the labeling problem is solved by:

$$\begin{aligned} x^{opt} = arg \min_{x} \Big[\sum_{e_{ij} \in E} (w_{ij}|x_i - x_j|)^q \Big]^{\frac{1}{q}} \\ \text{s.t. } x(F) = 1, x(B) = 0, \end{aligned} \tag{2.1}$$

In the final solution, the vertices which have the value $x_i \geqslant 0.5$ are labeled as foreground and $x_i < 0.5$ are labeled as background. The solution has been shown to converge to Graph-cuts for $q = 1$, random walker for $q = 2$, and shortest paths for $q = \infty$ [31]. The Eq. 2.1 represents the general optimization problem of labeling in graph-theoretic image segmentation. We will show that this optimization problem for $q = \infty$ can be solved by a CA-based algorithm.

2.2.2 Cellular Automata in Image Segmentation

A cellular automata is basically a computer algorithm that is discrete in space and time, and operates on a lattice of cells [36]. Since it was first proposed by Von Neumann and Ulam [37], Cellular Automata has attracted researchers from various fields in both physical and social sciences because of its simplicity, and potential in modeling complex systems [38].

Each individual cell is in a specific state and changes synchronously depending on the states of some neighbors as determined by a local update rule [39]. They are parallel, local and homogeneous, since the state of any cell depends only on the states of the local neighbors at the previous time step and the update rules are same for every cell.

Formally, a cellular automaton (CA) is a triple $A = (S, N, \delta)$, where S is a nonempty set, called the state set, N is the neighborhood, and $\delta : S^N \to S$ is the local transition function (rule); S^N, which is the argument of δ, indicates the states of the neighborhood cells at a given time, while S, which is its value, is the state of the central cell at the next time step[36].

Although the usual definition for "Cellular Automata" is in favour of a finite state set (discrete and bounded), continuous state sets in which the states are real numbers are also used in CA literature under the name "Continuous CA" or "Coupled Map Lattices" [40, 41, 42, 35, 43, 44]. A detailed discussion and some of the issues that can arise while using a continuous state set on a finite machine are given in [40, 41].

There are various attempts of using CA in image processing problems including: Image enhancement (sharpening and smoothing) [45], image filtering, edge detection [36], and image segmentation (Grow-cut) [35].

Grow-cut method uses a continuous state cellular automata to interactively label images using user supplied seeds. The cells are corresponding to image pixels, and the feature vector is RGB or gray scale intensities. The state set $S(\theta, l, \vec{C})$ for each image pixel consists of a "strength" value θ in a continuous interval $[0, 1]$, a label l and an image feature vector $\vec{C}$. The automata is initialized by assigning corresponding labels at seeds with a strength value between 0 and 1 where a higher value reflects a higher confidence in choosing the seed. Strengths for unlabeled cells are set to 0. A pseudo code for the Grow-cut algorithm is given below [35]:

```
// For each cell ...
for $\forall p \in P$
    // Copy previous state
    $l_p^{t+1} = l_p^t$
    $\theta_p^{t+1} = \theta_p^t$
    // Neighbors try to attack current cell
    for $\forall q \in N(p)$
        if $g(\|\vec{C}_p - \vec{C}_q\|_2) \cdot \theta_q^t > \theta_p^t$
            $l_p^{t+1} = l_q^t$
            $\theta_p^{t+1} = g(\|\vec{C}_p - \vec{C}_q\|_2) \cdot \theta_q^t$
        end if
    end for
end for
```

where g is a pixel similarity function bounded to $[0, 1]$ depending on the image features i.e.

$$g(x) = 1 - \frac{x}{\max \|\vec{C}\|_2} \tag{2.2}$$

where the argument x is for instance, the absolute difference between the intensities of two neighboring pixels.

The surprising success of this simple algorithm, especially on medical images, motivated us to further analyze the algorithm. We showed that the result of the iterations of this algorithm converges to that of the shortest paths algorithm by modifying the similarity function used: $g(x) = e^{-x}$ (see Section 2.3.1). We note that, the original similarity function used in Grow-cut (Eq. 2.2) is a first order approximation to the one we utilized. In connecting shortest paths to cellular automata framework, maximizing the product of the edge weight w_{ij} (defined in Eq. (2.12) in the Section 2.3.1), was shown to be equivalent to minimizing the sum of the $-log w_{ij}$'s, i.e. $||\nabla_{ij}||$'s, resulting in the shortest path between a seed node to any non-seed node in the graph over the negative logarithm edge weights. These weights can be interpreted similarly to the reciprocal weight w_{ij}^{-1} defined in Sinop and Grady [31], which was shown to infer a connection between the shortest path algorithm and the general seeded segmentation optimization Eq. (2.1) with L_∞ norm minimization.

Simultaneously and independently from our work, it has also been shown that the Grow-cut algorithm is equivalent to the Belman-Ford algorithm, which calculates the shortest paths on a weighted graph [44]. However, there, the motivation and emphasis was on fast hardware implementation of the CA algorithms, due to both increasing availability of low cost graphical hardware (GPUs), and CA algorithm's suitability to run on parallel processors.

Shortest path idea was utilized in other works such as [46], where the Eikonal equation was solved with two different boundary conditions constructed from foreground and background seeds. Image-dependent speed functions were inserted into the right handside of the Eikonal equation, whose solutions led to two distance functions: shortest paths of each pixel from the foreground seeds and the background seeds. For each pixel, the smaller distance to the foreground seeds produced the resulting segmentation.

2.3 Method

In this section, the complete segmentation framework to segment brain tumors and the necrotic regions enclosed is presented in detail. Shortest path calculation using cellular automata iterations is given in Section 2.3.1. An overview of the algorithm with the pseudo-code of the implementation is given in Section 2.3.2. Major steps of the algorithm is explained in detail in sections 2.3.3, 2.3.4, 2.3.5 and 2.3.6 followed by the datasets and methods used for performance evaluation in Section 2.3.7.

2.3.1 Cellular Automata: its Connection to Graph Theoretic Methods

A graph consists of a pair $G = (V, E)$ with vertices (nodes) $v \in V$ and edges $e \in E \subseteq V \times V$. The weight of an edge, e_{ij}, is denoted by w_{ij} and is assumed here to be nonnegative and undirected (i.e., $w_{ij} = w_{ji}$). We will use closed neighborhood $N_G[v]$ where $v_i \in N_G(v_i)$. The edge weights are similarity measures calculated using measured data (e.g. voxel intensity) for vertices: $w_{ij} = f(I_i, I_j) \in (0, 1]$ and self-similarity $w_{ii} = 1$. State of a vertex $s(v_i) = s_i$ is specified with a real value $x(v_i) = x_i \in [0, 1]$ and a label $l_i \in \{BG, FG, \cdots\}$ pair. Starting with initial states of vertices, in each iteration, vertices of graph G is updated by the following rule:

$$l_i^{t+1} = l_{i^*}^t \text{ and } x_i^{t+1} = w_{i^*i} x_{i^*}^t \text{ where } i^* = \arg\max_{j \in N_G[v_i]} w_{ji} x_j \tag{2.3}$$

Note that since the vertex itself is also included in its neighborhood, Eq. (2.3) also covers the static case:

$$s_i^{t+1} = s_i^t \text{ if } x_i \geq w_{ji} x_j \text{ for } \forall v_j \in N_G[v_i] \setminus v_i \tag{2.4}$$

Vertex states are initialized by user supplied seeds $p_i \in P$ such as:

$$s^0(v_i) = (1, l(p_i)) \text{ for } v_i \in P \text{ and } s^0(v_i) = (0, \emptyset) \text{ for } v_i \notin P \tag{2.5}$$

This map converges since $\sum_i x_i$ is upper-bounded and monotonically increasing:

$$\lim_{t \to \infty} s_i^{t+1} = s_i^t \text{ for } \forall v_i \in V \tag{2.6}$$

Now, let us derive some properties on the final map. Consider any vertex v_i of a graph G, and assume that a latest update occurred on this vertex at time t_i. The vertex which updates v_i is v_{i^*}. Final state for v_i is:

$$s_i^{t \geq t_i} = (w_{i^*i} x_{i^*}^{t_i}, l_{i^*}^{t_i}) \tag{2.7}$$

If any update occurs on v_{i^*} at time $t_{i^*} \geq t_i$ by $v_{i^{**}}$, this should satisfy the condition:

$$x_{i^*}^{t_{i^*}} = w_{i^{**}i^*} x_{i^{**}}^{t_{i^*}} > x_{i^*}^{t < t_{i^*}} \text{ that gives } w_{i^*i} x_{i^*}^{t_{i^*}} > w_{i^*i} x_{i^*}^{t < t_{i^*}} \tag{2.8}$$

However, this will also cause an update on v_i at $t > t_{i^*} > t_i$, which violates the condition in (2.7). Then, at the converged map, there exists a neighbor v_{i^*} for each vertex v_i such that:

$$s_i = (w_{i^*i} x_{i^*}, l_{i^*}) \tag{2.9}$$

If we go one step further:

$$s_{i^*} = (w_{i^{**}i^*} x_{i^{**}}, l_{i^{**}}) \text{ and } s_i = (w_{i^*i} w_{i^{**}i^*} x_{i^{**}}, l_{i^{**}}) \tag{2.10}$$

We can follow this path for any vertex until we reach a seed which is never updated:

$$s(v_i) = (\prod_{\Omega(p_i \to v_i)} w_{jk}, l(p_i)) \tag{2.11}$$

Therefore, this algorithm cuts the graph G to independent subgraphs for each seed, consisting of spanning trees with seeds at root nodes.

If we set edge weights depending on similarity of image ($I : R^3 \rightarrow R$) neighborhoods as:

$$w_{jk} = e^{-\beta||\nabla_{jk}I||} \tag{2.12}$$

where $||\nabla_{jk}I||$ denotes a Euclidean norm on the difference between intensities of two adjacent vertices v_j and v_k. Maximization of the product of w_{jk}'s along the path Ω becomes equivalent to minimization of the summation of $||\nabla_{jk}I||$'s along the same path. $\sum_{\Omega(p_i \rightarrow v_i)} ||\nabla_{jk}I||$ is a discrete approximation to a geodesic or shortest path between the seed p_i to a voxel v_i. Each voxel is then assigned to the foreground label if there is a shorter path from that voxel to a foreground seed than to any background seed, where paths are weighted by image content. With this interpretation, cellular automata algorithm solves the shortest paths energy form formulated in [31].

The equivalence, which we showed, between CA updates by Eq. (2.3) and shortest path algorithm is illustrated in Fig. 2.1.

The main advantage of using CA algorithm is its ability to obtain a multilabel solution in a simultaneous iteration. Another advantage is that the local transition rules are simple to interpret, and it is possible to impose prior knowledge, specific to the problem, into the segmentation algorithm.

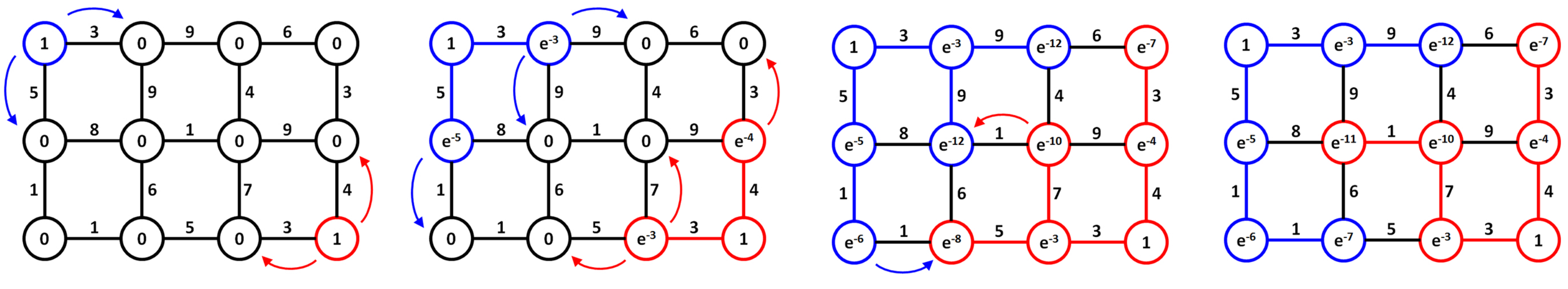

(a) (b) (c) (d)

Figure 2.1: (a) The graph is initialized with similarities as edge weights and vertex values 1 for seeds, 0 elsewhere; (b-c) intermediate propagation steps for CA; (d) shows the final vertex values obtained from CA which can also be obtained as the shortest path from each vertex to a seed.

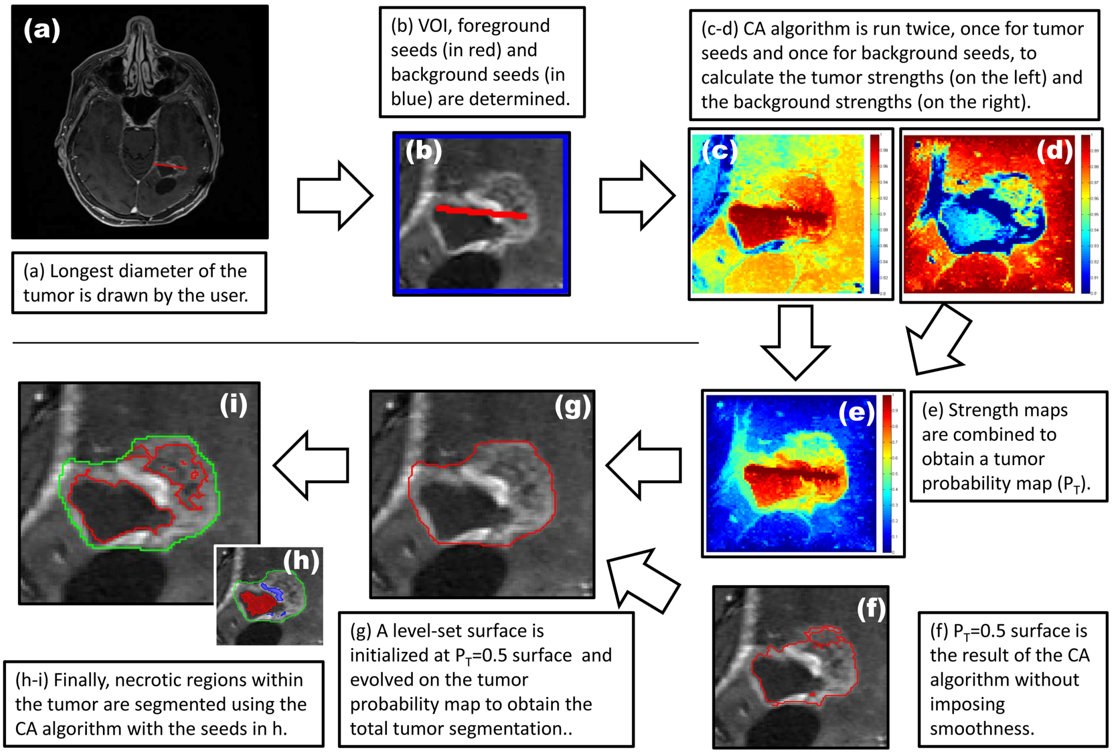

(a) Longest diameter of the tumor is drawn by the user.

(b) VOI, foreground seeds (in red) and background seeds (in blue) are determined.

(c-d) CA algorithm is run twice, once for tumor seeds and once for background seeds, to calculate the tumor strengths (on the left) and the background strengths (on the right).

(e) Strength maps are combined to obtain a tumor probability map (P_T).

(f) P_T=0.5 surface is the result of the CA algorithm without imposing smoothness.

(g) A level-set surface is initialized at P_T=0.5 surface and evolved on the tumor probability map to obtain the total tumor segmentation..

(h-i) Finally, necrotic regions within the tumor are segmented using the CA algorithm with the seeds in h.

Figure 2.2: Steps of the proposed tumor segmentation method: see text for explanations.

2.3.2 Tumor-cut Algorithm

Steps of the proposed cellular automata based tumor segmentation algorithm is shown in Fig. 2.2. First, (a) the user draws a line over the largest visible diameter of the tumor; (b) using this line, a VOI is selected with foreground(red)-background(blue) seeds; (c-d) tumor CA algorithm is run on the VOI for each two sets of seeds (for the foreground and background) to obtain strength maps for foreground (c) and background (d) at each voxel; (e) two strength maps are combined to obtain the tumor probability map P_T (Eq. (2.16)); (f) a level set surface is initialized at $P_T = 0.5$ and the map P_T is used to evolve the surface which converges to the final segmentation map (g). Finally, (i) the necrotic regions of the tumor is segmented using a CA-based method with the chosen enhanced and necrotic seeds in (h).

A pseudo code of the Tumor-cut algorithm is given below:

```
for $\forall l \in \{Tumor, Background\}$
    // Initialize
    for $\forall p \in P$
        if $p$ is a seed of class $l$, $x^0_{l,p} = 1$, else $x^0_{l,p} = 0$
    end for
    Do until convergence
    // For each cell ...
    for $\forall p \in P$
        // Neighbors try to attack current cell
        for $\forall q \in N(p)$
            Find $q^*$: q with maximum $g(p,q) \cdot x^t_{l,p}$
            $x^{t+1}_{l,p} = g(p,q^*) \cdot x^t_{l,q^*}$
        end for
        // Copy previous state
        $x^{t+1}_{l,p} = x^t_{l,p}$
    end for
    end do
end for
// Combine strengths for tumor and background to obtain
  tumor probability map
$P_T = ln(x_{Bg})/(ln(x_{Bg}) + ln(x_T))$ Eq. (2.16)
// Evolve the tumor surface via a level set embedding
$\frac{\partial S}{\partial t} = (u-v)(u+v-2P_T)N$
// where $u, v$ are the means inside and outside the surface,
  and $N$ is the unit normal vector to surface $S$.
// Segment necrotic parts within the segmented tumor
  volume.
```

2.3.3 Seed Selection Based on Tumor Response Measurement Criteria

In “Response Evaluation Criteria In Solid Tumors” (RECIST), which is a widely used procedure to evaluate the treatment response of the solid tumors, tumor progress is classified by measuring the longest in plane tumor diameter in one dimension (axial, coronal, sagittal)[47]. Our seed selection algorithm employs the same idea to follow the familiar clinical routine to which the clinicians are used to: the volume of interest (VOI), the tumor seeds and the background seeds are determined by using the line already drawn by the user to measure the longest diameter of the solid tumor. Similarly, focusing on tumor segmentation problem, the seed selection procedure starts with a single line drawn by the user along the longest visible diameter of the tumor. Afterwards, the VOI and the seeds are computed as follows: (i) The line is cropped by 15% from each end and thickened to 3 pixels wide to obtain tumor seeds; (ii) VOI is selected as the bounding box of the sphere having a diameter 35% longer than the line; (iii) One-voxel-wide border of this VOI is used as background seeds(see Fig. 2.2a, 2.2b).

Since the VOI is completely bounded by the background seeds, each path connecting inside and outside the VOI is blocked by a seed. Then, the result of labeling using only the data inside the region is equivalent to using the whole volume whereas the computation time is significantly reduced.

One obvious drawback is that the user draws the line on only a single slice of the tumor volume, hence it is not guaranteed that the depth of the tumor will also coincide with the VOI. For determining the enlargement ratio for the bounding box size, the percentage of the volume enclosed in the sphere to the total tumor volume is calculated for different enlargement ratio values, and the results are plotted in Fig. 2.3. For our data set, %100 coverage was achieved with 2.00 times enlargement. We used 1.35, which covers %99 of all tumors with 5 different initializations, which gave a reasonable trade-off between the 3D inclusion of the whole tumor versus the computation time increase due to enlargement of the volume. Furthermore, the average Dice Overlap between the sphere drawn around the longest diameter line and the tumor is found to be 56.7 ± 16.1 percent, which confirms the sphericity assumption on solid tumors.

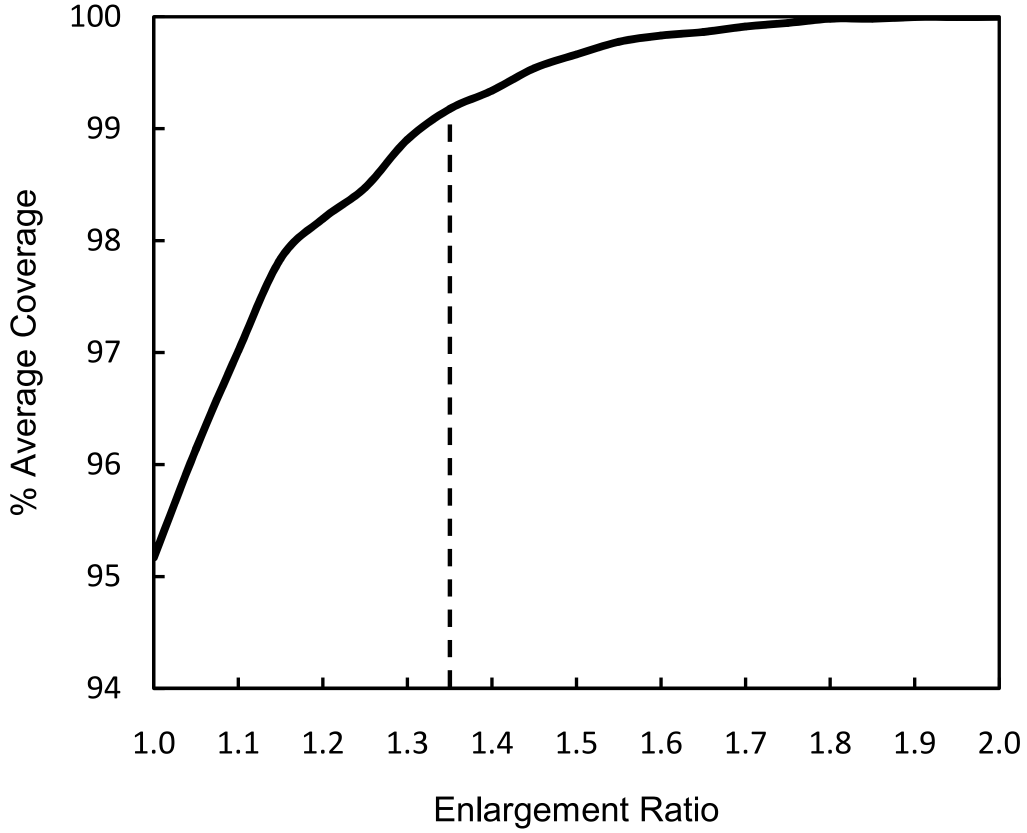

Figure 2.3: Change of average coverage with enlargement ratio.

In occasional cases of slightly concave-shaped tumors, the maximum diameter line will not be enclosed by the tumor completely. Even in these cases, the algorithm can perform the segmentation successfully if an input 1D line is correctly drawn to fall inside the tumor region. The line enlargement parameter selected for VOI formation is determined by taking such cases into account, hence, the VOI contains the whole tumor.

2.3.4 Adapting Transition Rule to Tumor Characteristics

In the tumor segmentation application, the cells or nodes in cellular automata framework correspond to the MRI volume voxels in 3D. A 26-cell cubic neighborhood is used in 3D. MRI intensities are used as image features. The automata is initialized with user supplied tumor and background seeds as explained in section 2.3.3 and iterated by the following rule:

$$l_i^{t+1} = l_{i^*}^t \text{ and } x_i^{t+1} = g(i, i^*) x_{i^*}^t \text{ where } i^* = \arg\max_{j \in N_i} g(i, j) x_j^t \tag{2.13}$$

where g is a pixel similarity or transition function bounded to $[0, 1]$, which is equivalent to the edge weight function w_{ij} in the seeded segmentation framework. A typical symmetric edge weight function depending on the image features, is given by the absolute intensity difference or gradient magnitude between neighboring nodes i and j:

$$g(i, j) = e^{-\|I_i - I_j\|} \tag{2.14}$$

where I_i denotes the MR image intensity at node i.

In the seeded tumor segmentation application over contrast enhanced T1-weighted MRI for heterogeneous tumors, which mostly consist of a ring enhancing region around a dark necrotic core (and also irregular borders), most of the foreground seeds fall in the necrotic region. This sometimes causes the segmentation algorithm to get stuck at necrotic to enhancing tumor transition borders. To overcome such problems, prior knowledge that tumor voxels are brighter in post contrast T1-MRI can be utilized. This can be achieved by modifying the transition function $g(i, j)$ by inserting a spatially-varying parameter:

$$g(i, j) = \begin{cases} e^{-\beta\|I_i - I_j\|} & \text{if } I_i > I_j \text{ and } l_j = Tumor \\ e^{-\|I_i - I_j\|} & \text{otherwise} \end{cases} \tag{2.15}$$

The intuition here is based on the observation that the enhancing tumor cells are brighter than the normal tissue, and more centrally located necrotic core is darker. Therefore, by adjusting the β parameter, the weight reduction (i.e. the strength loss) of a tumor state while passing through a ramp up gradient is adjusted to be lower than other cases.

The effect of β parameter on the segmentation performance in terms of Dice overlap measure is demonstrated in Figure 2.4. Although, some of the properties we derived for the algorithm is no more valid, as due to asymmetric edge weight values, we can no longer interpret the algorithm in the undirected graph framework as in

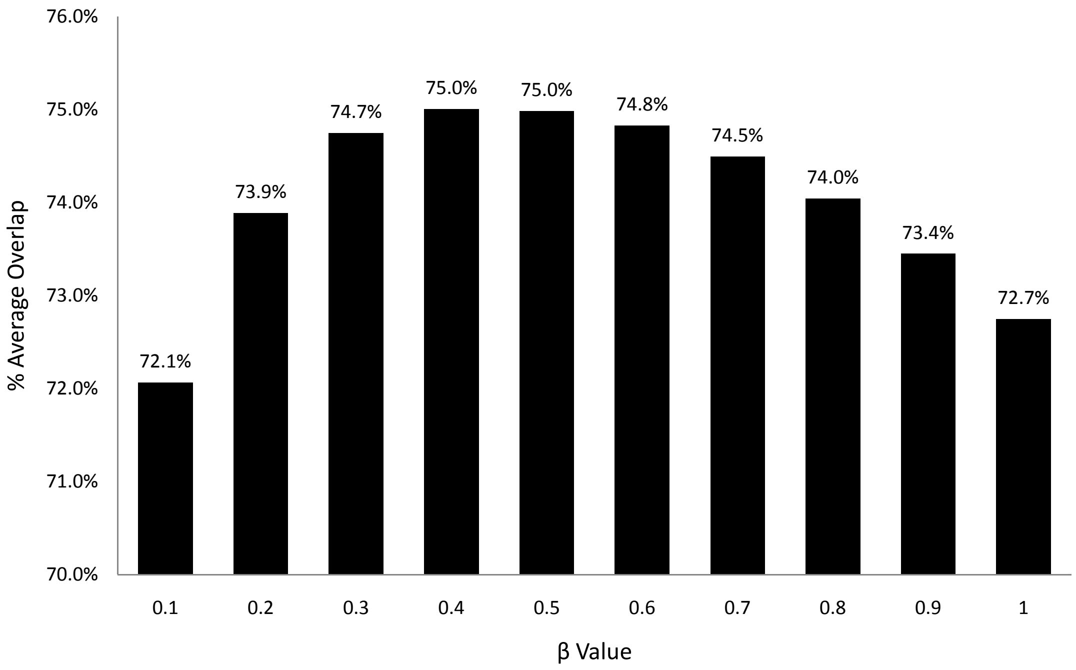

Figure 2.4: Effect of β on the segmentation performance.

the Section 2.3.1, our experimental results revealed that the new tumor CA (tCA) algorithm significantly improved the results obtained, especially on glioblastomas [43].

2.3.5 Level Set Evolution on Constructed Tumor Probability Map

Smoothing is an important prior in segmentation of brain tumors from post contrast T1 images, because of three main reasons: First, an area surrounded by tumor tissue is considered as a tumor region even the intensity characteristics are likely to be healthy. Secondly, it is possible to include misclassified necrotic regions to tumor region, which are usually surrounded by enhanced tissue. Finally, it is possible to exclude nearby vascular structures that are enhanced by administration of the contrast agent.

CA algorithm has the advantage of finding distance of each cell to the nearest seed in a simultaneous iteration. However, the resulting strength map has only onesided information, that is the distance to the other label classes is not available. In order to create a probabilistic map, which can be used in an active surface (e.g. a level set surface) evolution, the algorithm is run for each class with corresponding class seeds (tumor and healthy) separately. Geodesic distances to the class seeds can be calculated by $D = -ln(x)$. Therefore, the tumor probability map is obtained by combining the distances for tumor (D_T) and background (D_B) as:

$$P_{Tumor} = \frac{D_B}{D_T + D_B} \tag{2.16}$$

The intuition with this probability construction, is that probability of being a tumor is proportional to its distance normalized to the closest background seed. This leads to choosing a higher probability of being a tumor when the distance to the background seeds is large, and vice versa.

After obtaining the tumor probability map using the foreground and background strength maps, an implicit 3-D level-set surface is initialized over the volume V whose inside is given by $\{(X, Y, Z) : P_{Tumor} > 0.5\}$. The level set function whose zero-level set represents an initial estimate of the tumor surface, S, is evolved on P_{Tumor} with a piecewise constant region assumption of [26], however by using a local Gaussian kernel to define inner and outer regions around the propagating surface in order to compute regional statistics of the map, which constitute the inside and outside sample means in this case. When the surface evolution converges, the final tumor segmentation map is obtained.

The level-set-based smoothing over the constructed tumor probability map in Eq. (2.16) constitutes an important part of the proposed method, as the clinical expert segmentation, particularly in radiation oncology, mainly outlines the tumor borders using contouring for radiotherapy planning as opposed to pixel by pixel labeling of the tumor carried out in some validation studies. As a result, our interactive tumor segmentation includes an appropriate intelligent smoothing of the tumor borders based on the labeling results obtained from a graph-theoretic approach. This is a process that is expected to simulate the expert's manual contouring. The qualitative effect of adding the smoothing step over the CA result is shown in Fig. 2.5, which exemplifies how the borders are smoothed after level set evolution over the tumor probability map displayed in (b).

In order to determine the optimal choice for β parameter and smoothing weight-

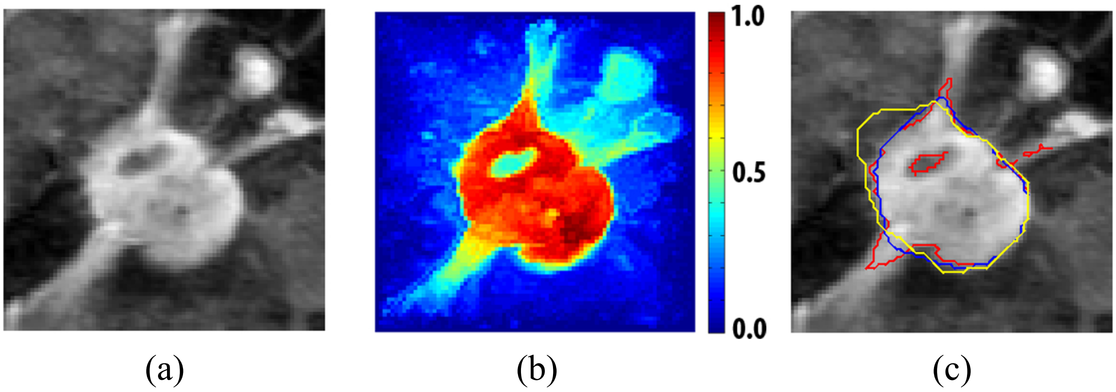

Figure 2.5: Effect of Smoothing. Example of tumor slice with vascularization and necrotic part (a). Tumor probability map obtained by CA algorithm (b). Segmentation result before smoothing (red), after smoothing (blue) and expert (yellow) (c).

ing pair for tumor segmentation application, the algorithm is run for each β parameter value varying between 0.4 to 1.0 whereas the smoothing weighting varies from 0.0 to 0.8. Using manual expert segmentations as ground truth, average Dice overlaps obtained by each β parameter and smoothing level pair are plotted in Fig. 2.6. It can be observed that $\beta = 1$ with 0.2 smoothing weight, which are used for validation studies throughout the rest of the paper, give the best overlap performance.

2.3.6 Enhancing/Necrotic Segmentation

Quantification of the necrotic regions within a whole tumor is an important problem in assessment of the tumor progress. Delayed radiation necrosis, which typically occurs 3 months or more after treatment, is the primary risk associated with stereotactic radiosurgery [48]. Necrosis of the tumor can occur as a result of the radiosurgery as well as by the tumor progress itself like in high grade gliomas. Furthermore, following some radiosurgery treatment sessions (i.e. CyberKnife treatment of acoustic neuromas), increase of the necrotic regions can be observed, which accompanies the clinical improvement, without a significant change of the tumor core.

Necrotic class naturally arises in segmentation using multi protocol (T1, CE-T1, T2, DWI etc.) intensity classifiers due to its different intensity characteristics

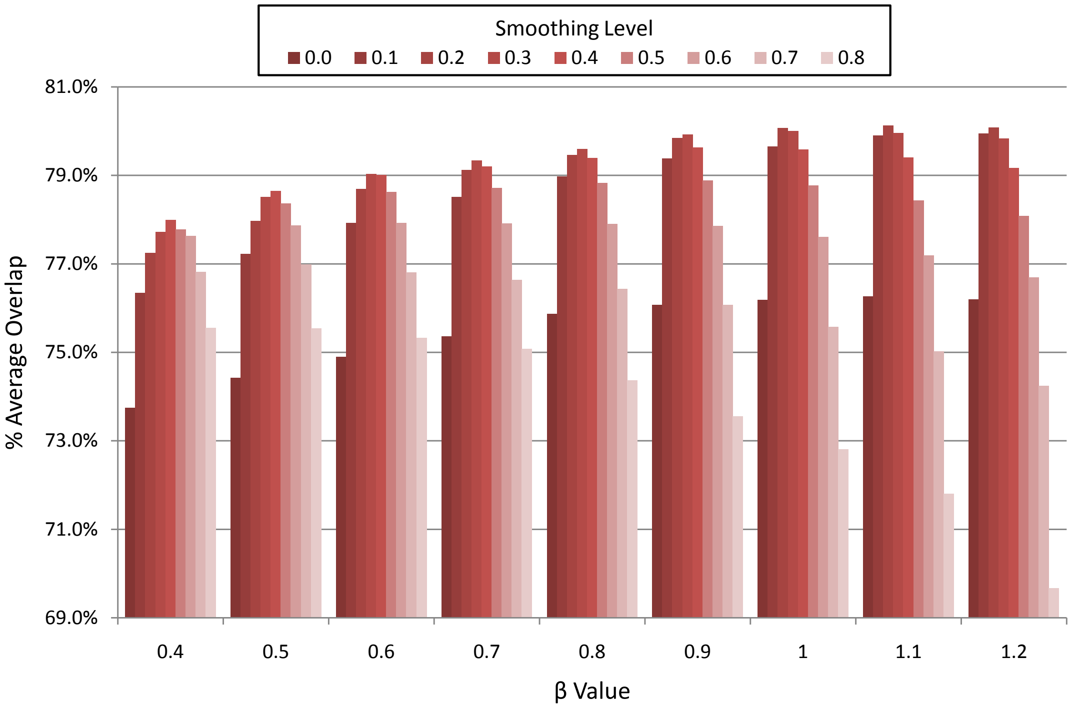

Figure 2.6: Effect of β for different smoothing levels (increasing from dark to light) on the average dice overlap performance on our clinical data set.

in different modalities. However, our aim in this study is to quantify the necrotic and enhanced parts of the tumor using solely contrast enhanced T1 weighted MRI volumes. This can be achieved by a two step sequential algorithm. Firstly, tumor volume (including both enhanced and necrotic tissues) is segmented by the method as described in sections 2.3.3-2.3.5 and then the necrotic and enhanced classes are separated inside the whole tumor volume.

In CE-T1 MR images, necrotic parts of the tumor are observed as hypo-intense for there is no blood flow into these regions where enhanced parts are hyper-intense. Without any prior information, segmentation using an intensity threshold can be applied by assigning necrotic label to the voxels lower than the chosen threshold and enhanced label to those that are higher. To choose the threshold, we explored using expectation maximization [49] and Otsu's methods [50]. However, usually the two classes are not separable on the intensity histogram even though they could be separated easily on the image as seen on the sample case in Fig. 2.7.

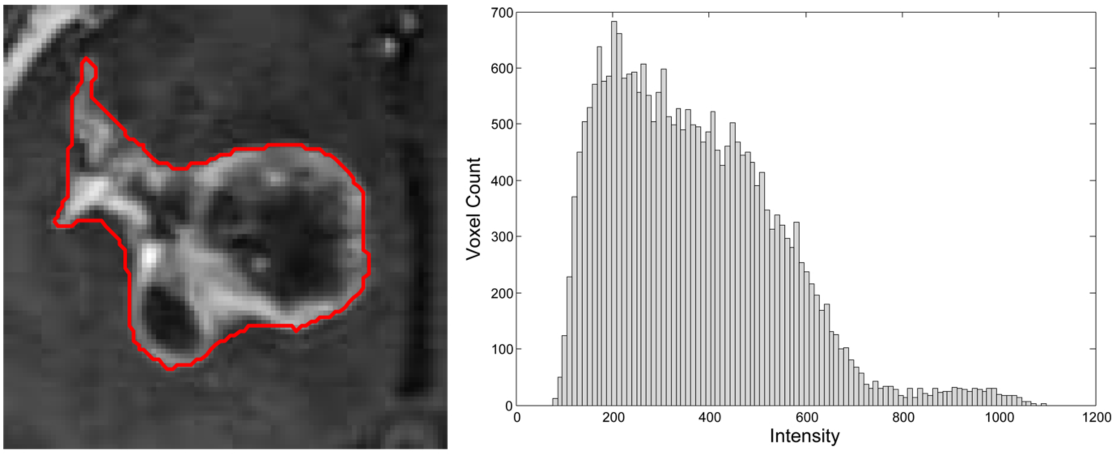

(a)

(b)

Figure 2.7: (a) Tumor contour calculated by the proposed method, overlayed on a sample MRI slice. (b) MRI intensity histogram of the 3D tumor volume.

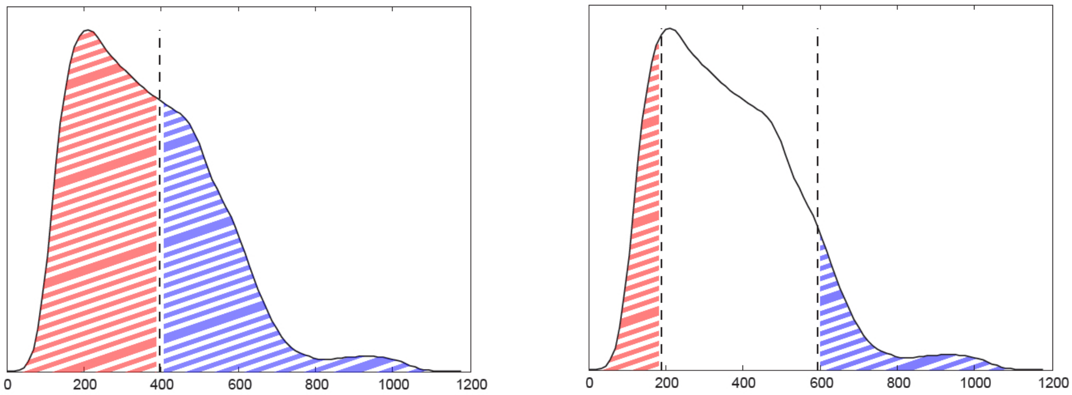

(a)

(b)

Figure 2.8: (a) Segmentation with a single threshold. (b) Necrotic and enhanced thresholds to determine initial seeds.

Instead of using simple tresholding, connectedness was imposed by using the CA algorithm with two thresholds as follows: Initially the voxels lower than a necrotic threshold are labeled as necrotic seeds and higher than an enhanced threshold are labeled as enhanced seeds as in Fig. 2.8. Next, the voxels at remaining mid-intensities are labeled by assigning the label of the nearest seed using the CA algorithm.

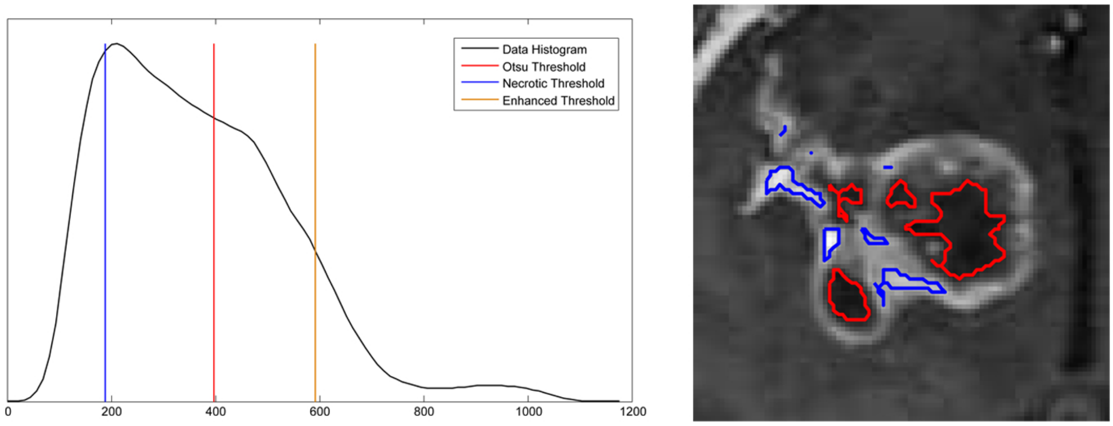

(a) (b)

Figure 2.9: (a) Thresholds calculated by Otsu's method and double thresholds calculated by the proposed necrotic/enhanced segmentation method. (b) Enhanced and necrotic seeds determined by the proposed method, used as an input to the CA segmentation algorithm (Necrotic seeds in red and enhanced seeds in blue).

An algorithm to choose the two thresholds is devised as follows: First the number of necrotic voxels (N_{nec}^{OTSU}) and the number of enhanced voxels (N_{enh}^{OTSU}) are roughly calculated by using Otsu's method. Then the necrotic and enhanced thresholds are determined such that %25 of the necrotic volume is assigned as necrotic seed and %25 of the enhanced volume is assigned as enhanced seed (see Fig. 2.9).

$$\sum_{I=0}^{T_{nec}} H(I) = 0.25 \cdot N_{nec}^{OTSU} \text{ and } \sum_{I=T_{enh}}^{I_{max}} H(I) = 0.25 \cdot N_{enh}^{OTSU} \tag{2.17}$$

where H is the volume intensity histogram, N_{nec}^{OTSU} and N_{enh}^{OTSU} are rough volumes estimated with Otsu's method and T_{nec} and T_{enh} are the necrotic and enhanced thresholds.

2.3.7 Data and Evaluation Methods

Validation studies of the developed method is carried out over three different datasets of all contrast enhanced T1-MR images:

1. *Synthetic datasets of simulated tumors from Utah* [2]

   Five synthetic brain tumor datasets, available online from University of Utah

[2] are used in the first part of the validation studies. The utilized data simulates contrast-enhanced T1-weighted MR images with synthetically generated tumors. The tumor probability maps are also available with the dataset for validation purposes. This dataset is included in the performance evaluations since the ground truth segmentation is readily available.

2. *Harvard Brain Tumor Repository* [51]

   A tumor repository, which includes 10 tumors with multiple manual expert segmentations on 2D slices, from Harvard [51], was utilized in the second set of experiments, due to its availability online and providing a common framework to compare performances of different algorithms. The repository includes contrast enhanced T1-weighted MR images, acquired with SPGR sequence at 0.9375x0.9375x1.5 mm contiguous sagital slices. Recently, the data from this repository have been evaluated by a validation framework, known as STAPLE [19], which calculates sensitivity, specificity, and total correct fraction criteria for evaluation of the proposed method against multiple expert segmentations. With Harvard brain repository data, it is possible to compare intra- and inter-rater variation vs. the algorithm's robustness.

3. *Brain Tumor datasets obtained from our clinical Radiation Oncology site (ASM)*

   In radiosurgery planning of brain tumors, target tumor volume, which is desired to receive sufficiently high dose, is outlined on MR images by a radio-oncology specialist. A large dataset of brain tumor patients, who received CyberKnife radiosurgery treatment in Anadolu Medical Center (ASM), Kocaeli, Turkey was utilized in the third set of experiments. MR images of 19 tumors of 14 patients were obtained by 1.5T MRI scanner located at the same hospital as high resolution ($\approx$ 0.5x0.5x1.0 mm) contiguous axial T1 weighted 3D SPGR MRI volumes (TE/TR = 3.16s/8.17s, FA=25) acquired after IV injection of 10cc 0.5M Multihance Gd. Figure 2.10 demonstrates axial snapshots of a sample central slice for each tumor in the dataset. As the ground truth for segmentation, we used the tumor contours outlined manually by a radio-oncologist for radiosurgery planning.

---

[2] http://www.ucnia.org/softwaredata/5-tumordata/10-simtumordb.html

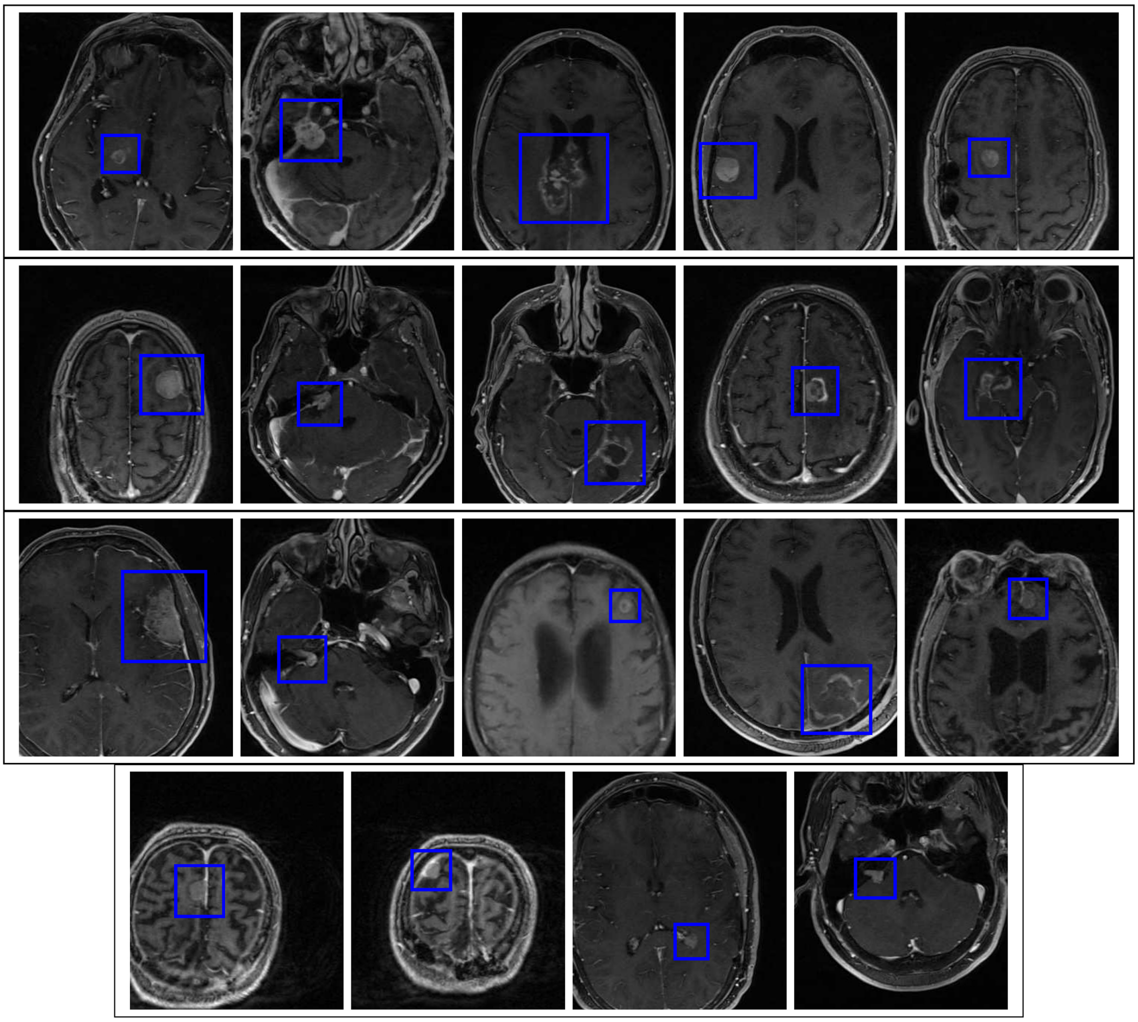

Figure 2.10: Clinical data set used for validation studies.

In assessment of the tumor segmentation performance, for each of the tumor cases, the following similarity criteria are utilized: Dice overlap is used to quantify the overlap between obtained segmentation maps and the "true" segmentations as given in Eq. A.0.1 of Appendix A. In addition, tumor volume error is calculated as: $(|Vol(Algorithm) - Vol(Manual)|/|Vol(Manual)|$, where $Vol(.)$ is the tumor volume calculated over either the algorithm segmentation map or the manual segmentation map accordingly. Mean, median, and maximum of the surface distances are calculated using the minimum distances from the sampled points on the algorithm segmentation surface to the manual segmentation surface.

Interactive segmentation method outputs do usually vary with respect to initializations, and this is an important performance criterion in assessment of the quality of a segmentation method. To measure the robustness of the proposed method, for each tumor case, results with 5 different initialization lines are calculated and mean and standard deviation for each criterion are reported in the tables. This is crucial in showing the true performance of any segmentation method that requires an initialization, and it should be reported rather than result of an arbitrary initialization, typically from a maximally performing case.

For Harvard tumor repository and our clinical dataset, measured physical tumor volumes are compared using Bland-Altman analysis, which looks at the variation of difference volume in mm^3 between the real and estimated tumors vs. the average of the two volume measurements. Typical evaluation with a Bland-Altman analysis, is to check whether the results are scattered around the zero difference value within ± 1.96 times standard deviation.

The result of the Tumor-cut algorithm is compared to that of the Graph-cut and Grow-cut algorithms, on the clinical dataset. Graph-cut is included in comparison for its popularity among graph based segmentation methods, and Grow-cut is chosen since it is the first algorithm that uses CA for image segmentation. For each of the tumor cases, Graph-cut, Grow-cut and Tumor-cut algorithms are run with identical seed initializations. Average Dice overlaps and standard deviations of 5 different initializations for three methods, are given as bar plots.

2.4 Results and Discussion

2.4.1 Validations on Synthetic Data

The performance measures, Dice overlap, mean, median, and maximum surface distances and the volume percent error between the ground truth segmentation and the result of the algorithm are reported in Table 2.1 for the synthetic dataset. The standard deviations show the extent of performance for different realizations of the initialization. The Dice overlap is on the average 83%. Due to the challenging case 5, the volume error increased, however, it was typically between 10 ± 6 percent. The mean ± standard deviations for the maximum surface distance is $6.8 \pm 3.6mm$, the mean surface distance is $1.7 \pm 2.1mm$, and the median surface distance is $1.5 \pm 2.3mm$. Although synthetically created, the Utah tumor dataset contains tumor scenarios with low contrast difference between the tumor region and its background: for instance, the synthetic tumor labeled as case 5 is shown in Figure 2.11. The active surface propagation over the constructed probability map aims at correction and improvement of the segmentation by smoothing out the tumor borders, and avoiding sharp protrusions, however, here due to the low intensity contrast between the tumor tissue and the gray matter, the Tumor-cut performed worse than expected. This low performance result obtained on the non-enhancing tumor case 5, reveals the limitation of the method and its application to the tumors that are enhanced with the contrast agent.

Table 2.1: Performance criteria ± std deviations over 5 different initial seed lines for each tumor for synthetic tumor data set from [2].

	Dice Overlap (%)	Volume Error (%)	Maximum Distance (mm)	Mean Distance (mm)	Median Distance (mm)
Synthetic Tumor 1	91.1 ± 1.8	7.3 ± 5.5	7.6 ± 1.6	1.3 ± 0.3	1.0 ± 0.0
Synthetic Tumor 2	84.5 ± 7.4	14.8 ± 7.2	8.0 ± 2.3	0.9 ± 0.2	1.0 ± 0.0
Synthetic Tumor 3	97.6 ± 0.2	4.0 ± 0.4	3.7 ± 0.0	0.4 ± 0.0	0.0 ± 0.0
Synthetic Tumor 4	86.9 ± 0.1	16.1 ± 0.2	2.9 ± 0.4	0.5 ± 0.0	0.0 ± 0.0
Synthetic Tumor 5	53.0 ± 6.7	181.8 ± 43.8	11.9 ± 1.0	5.3 ± 0.8	5.6 ± 1.4
Average	82.6 ± 17.3	44.8 ± 76.7	6.8 ± 3.6	1.7 ± 2.1	1.5 ± 2.3

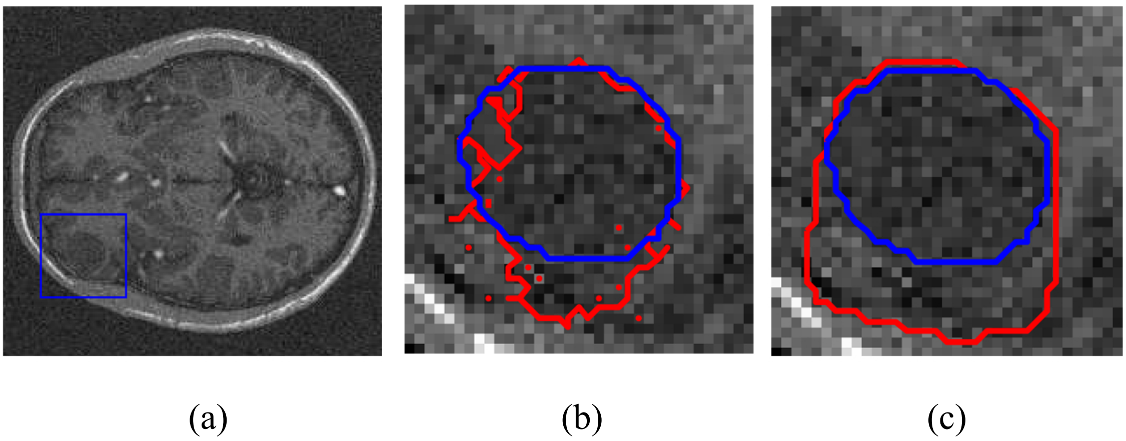

Figure 2.11: Synthetic tumor case 5 in Table 2.1. (a) An MRI slice is depicted; (b) Grow-cut result (red); (c) Tumor-cut method which includes a level set segmentation over the constructed probability map from tCA (red). Blue: Ground truth.

2.4.2 Validations on Harvard Brain Tumor Repository

Sensitivity, specificity and total correct fraction values evaluated by STAPLE are given in Figure 2.12 for Harvard tumor dataset. Sensitivity of the method is not statistically different from the expert results (within ±1.96 standard deviation), assuming an underlying Gaussian distribution of the variations around the mean. Specificity and total correct fraction values, on the other hand, are generally higher in the expert evaluations, however, the proposed method also performs at about 0.996 ± 0.005 in specificity and 0.995 ± 0.005 in total correct fraction. One can observe that tumor Case 8 performs especially poorly, which is depicted in Figure 2.13. Here, tumor tissue depicts intensity levels close to those of the surroundings, and high, continuous gradients of the complex background near the right boundary leads to a spread-out probability map as shown in the figure.

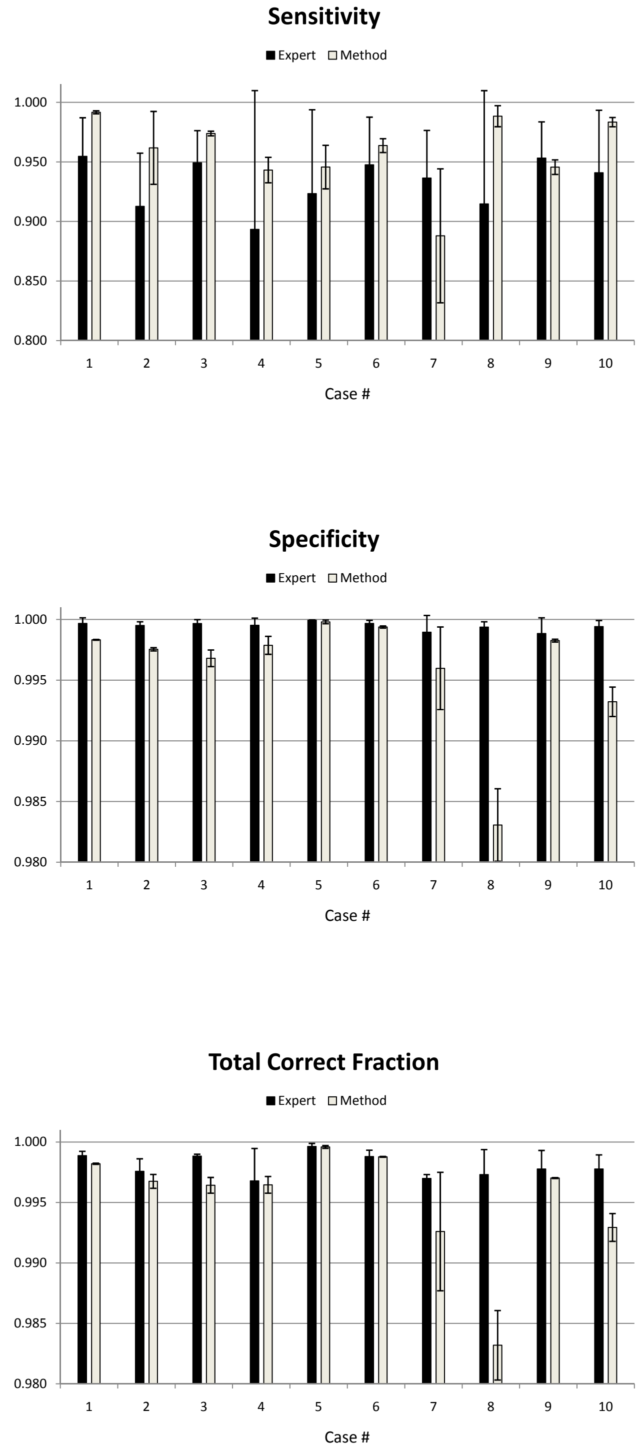

Figure 2.12: STAPLE evaluation results on Harvard Brain Tumor Repository.

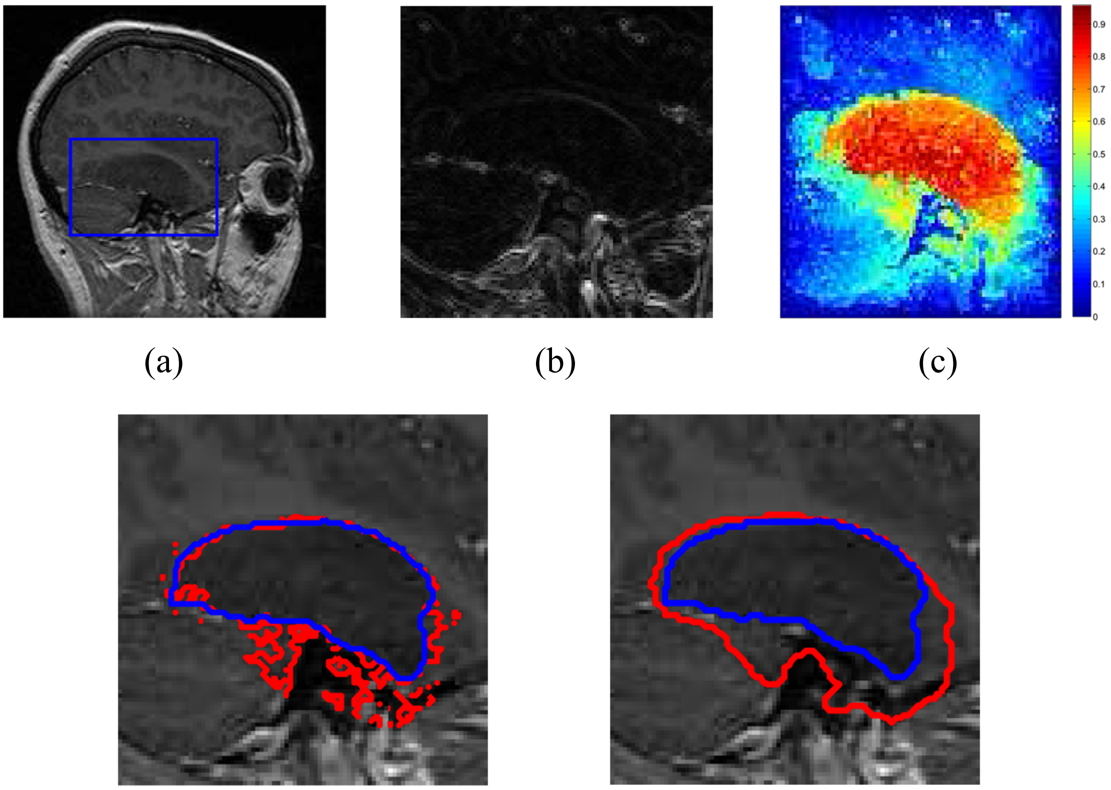

(a) (b) (c)

(d) (e)

Figure 2.13: Brain tumor repository data set case 8. (a) MR image slice; (b) gradient magnitudes; (c) the probability map constructed by Eq.(2.16); (d) Tumor-cut result without smoothing (in red), expert segmentation (in blue); (e) Tumor-cut-smoothed shows a spread out isosurface around value 0.5, possibly due to the tumor tissue depicting an intensity level close to its background and complex background with high gradients near the right boundary.

Table 2.2: Results on Harvard Brain Tumor Repository by the proposed method Tumor-cut.

		Dice Overlap (%)	Volume Error (%)	Maximum Distance (mm)	Mean Distance (mm)	Median Distance (mm)
Case 1	Meningioma	92.8 ± 0.1	15.6 ± 0.1	3.9 ± 0.0	1.2 ± 0.0	0.9 ± 0.0
Case 2	Meningioma	89.4 ± 1.5	17.5 ± 3.9	6.5 ± 0.3	1.5 ± 0.0	0.9 ± 0.0
Case 3	Meningioma	88.4 ± 1.8	24.8 ± 4.5	9.9 ± 1.9	2.1 ± 0.4	0.9 ± 0.0
Case 4	Low-grade glioma	91.5 ± 1.5	16.4 ± 3.7	6.1 ± 1.3	1.7 ± 0.3	0.9 ± 0.0
Case 5	Astrocytoma	95.1 ± 2.4	7.2 ± 5.5	1.6 ± 0.8	0.4 ± 0.2	0.4 ± 0.5
Case 6	Low-grade glioma	96.1 ± 0.3	6.0 ± 1.2	1.9 ± 0.0	0.7 ± 0.0	0.9 ± 0.0
Case 7	Astrocytoma	88.4 ± 7.5	8.4 ± 6.2	9.2 ± 4.9	2.6 ± 1.9	1.8 ± 2.0
Case 8	Astrocytoma	71.8 ± 3.4	78.6 ± 13.1	16.1 ± 2.5	6.5 ± 1.0	5.1 ± 1.5
Case 9	Astrocytoma	93.5 ± 0.1	8.3 ± 1.2	5.0 ± 0.4	1.1 ± 0.0	0.9 ± 0.0
Case 10	Low-grade glioma	86.2 ± 1.7	31.2 ± 4.7	12.5 ± 1.6	3.1 ± 0.4	1.8 ± 0.6
Average		89.3 ± 6.9	21.4 ± 21.7	7.3 ± 4.7	2.1 ± 1.8	1.5 ± 1.4

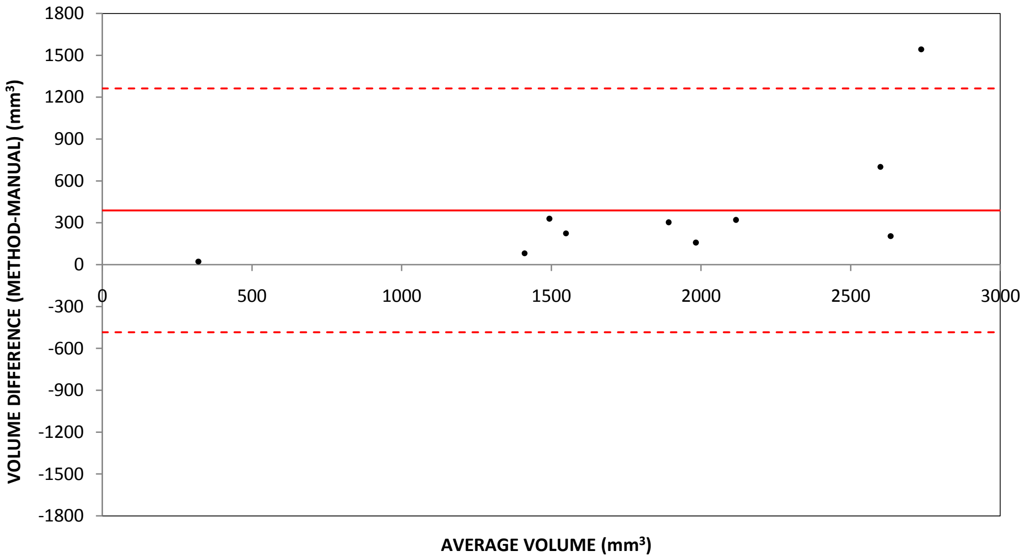

Figure 2.14: Bland-Altman plot of real and estimated physical tumor volumes (in mm^3) over Harvard Brain Tumor Repository. The dashed lines mark ±1.96 standard deviation values of the volume difference whereas the solid line marks its mean.

Table 2.2 shows the performance criteria statistics calculated for the Tumor-cut method over the Harvard brain tumor repository dataset. The Dice overlap over 10 tumor cases is 89.3% on the average, however, goes up to $89.3 + 6.9 = 96.2\%$ with better initialization scenarios. The volume percent error is 21.4 ± 21.7, which is degraded by the Tumor case 8, the worst performing one. We note that we included all the results including low performance ones rather than reporting that the algorithm failed for some tumors and excluding them as outliers from the statistics. Without such "outlier" cases, the overall statistics would as expected indicate higher success rates. The mean ± standard deviations for the maximum surface distance is $7.3 \pm 4.7mm$, the mean surface distance is $2.1 \pm 1.8mm$, and the median surface distance is $1.5 \pm 1.4mm$. Particularly, the median surface distance shows that the estimated tumor surfaces are fairly close to the expert outlined surfaces.

A Bland-Altmann analysis of the physical volume calculations, based on Tumor-cut segmentation method, is shown in Figure 2.14. Other than one failed case (case 8) as discussed above, the volume differences are inside the ±1.96 standard deviation interval as desired. However, we observed an overestimation in the measured volumes in the Harvard brain dataset. We found two possible reasons for this positive volume bias: (i) checking the tumor tissue image characteristics over the provided contrast enhanced T1-MRI, a smooth transition from the tumor contrast region to its surroundings could be seen (e.g. see Figures 2.13), which led to an oversmoothing in the constructed probability map, hence led to a slight over estimation; (ii) more likely reason is the clinical context and style of the manual segmentation maps. The experts who performed the tumor outlines preferred to draw the tumor border contours just inside the observed tumor edges. As our algorithm is motivated by the radiation therapy clinical application, the radiation oncology experts most likely draw the tumor border just outside the observed tumor edges rather than drawing them inside. The reason for this obvious preference is the fact that in the radiation therapy planning, a buffer zone is included around the tumor to ensure the inclusion of the enhancing tumor tissue on the rim of the tumor mass. This led us in our development of a tumor segmentation method for mainly radiation therapy planning, to design the level set smoothing stage over the tumor probability maps. We think this explains the volume over estimation by our method over the Harvard tumor dataset.

2.4.3 Validations on Tumors that undergo Radiation Therapy Planning

The clinical classification of tumors along with the different segmentation performance criteria of the Tumor-cut algorithm over the clinical radio-oncology dataset is tabulated in Table 2.3. The Dice overlap is 80.1 ± 6.9 on the average, volume percent error is 21.9 ± 12.1. In order to demonstrate the difficulty level of segmentation on the clinical radio-oncology dataset tumors, snapshots from a central axial slice over the VOI are given in Figure 2.10. The heterogeneous intensity character with both necrotic and enhancing tumor tissue content can be observed, and this heterogeneity leads to errors in existing segmentation methods. A comparison will be given in Figure 2.16 later. The mean ± standard deviations for the maximum surface distance is $5.5 \pm 2.7mm$, the mean surface distance is $1.2 \pm 0.6mm$, and the median surface distance is $1.0 \pm 0.4mm$. Another note here is the observation that the surface distance measures indicate an overall/major proximity of the expert-drawn and algorithm-computed surfaces, whereas the Dice overlap criterion is not as high as expected. In general, these two types of criteria (Dice overlap and surface distances) are not correlated. For instance, for small tumors (e.g. volume less than 1.5cc), we observed a low overlap score even though the surface distances between the manual delineations and the algorithm output surfaces were not relatively high.

Table 2.3: Performance criteria ± std deviations over 5 different initial seed lines for each tumor over the clinical radio-oncology dataset.

		Dice Overlap (%)	Volume Err.(%)	Maximum Dist.(mm)	Mean Dist.(mm)	Median Dist.(mm)
Tumor 1	Glioblastoma Multiforme	70.2 ± 7.3	24.3 ± 13.0	5.1 ± 1.0	1.0 ± 0.6	0.7 ± 0.4
Tumor 2	Acoustic Neuroma	76.2 ± 1.8	27.6 ± 8.4	10.2 ± 0.5	2.3 ± 0.2	1.2 ± 0.1
Tumor 3	Astrocytoma Grade 2-3	80.3 ± 5.7	27.1 ± 10.4	7.7 ± 1.2	1.8 ± 0.3	1.6 ± 0.2
Tumor 4	Brain Metastasis	80.9 ± 0.6	31.0 ± 2.4	3.4 ± 0.1	1.1 ± 0.0	1.1 ± 0.0
Tumor 5	Brain Metastasis	77.6 ± 0.5	34.6 ± 0.8	4.7 ± 0.1	1.1 ± 0.0	1.1 ± 0.0
Tumor 6	Brain Metastasis	83.3 ± 0.3	24.7 ± 1.0	4.6 ± 0.5	1.2 ± 0.0	1.1 ± 0.0
Tumor 7	Acoustic Neuroma	68.2 ± 1.2	46.4 ± 1.7	3.5 ± 0.4	1.0 ± 0.1	1.1 ± 0.0
Tumor 8	Glioblastoma Multiforme	88.2 ± 1.6	8.0 ± 6.6	7.2 ± 1.9	1.1 ± 0.2	0.8 ± 0.1
Tumor 9	Brain Metastasis	84.6 ± 0.6	16.9 ± 2.0	5.9 ± 0.5	0.9 ± 0.1	0.7 ± 0.0
Tumor 10	Astrocytoma Grade 2-3	90.3 ± 1.1	6.8 ± 4.4	5.4 ± 2.1	0.8 ± 0.2	0.6 ± 0.0
Tumor 11	Meningioma	82.4 ± 1.2	19.5 ± 2.7	12.1 ± 0.7	2.1 ± 0.1	1.2 ± 0.0
Tumor 12	Acoustic Neuroma	84.0 ± 0.4	16.1 ± 4.8	2.1 ± 0.2	0.5 ± 0.0	0.5 ± 0.0
Tumor 13	Brain Metastasis	65.9 ± 1.4	44.9 ± 3.3	5.0 ± 0.7	1.6 ± 0.1	1.5 ± 0.0
Tumor 14	Glioblastoma Multiforme	77.8 ± 4.7	16.6 ± 16.2	9.5 ± 3.1	2.5 ± 0.9	1.9 ± 0.6
Tumor 15	Meningioma	87.7 ± 1.6	10.1 ± 4.0	3.3 ± 0.2	0.6 ± 0.1	0.5 ± 0.0
Tumor 16	Meningioma	86.8 ± 0.7	4.6 ± 2.6	3.4 ± 0.6	0.8 ± 0.0	0.5 ± 0.0
Tumor 17	Meningioma	72.4 ± 1.1	26.8 ± 18.3	4.9 ± 0.1	1.2 ± 0.1	1.0 ± 0.1
Tumor 18	Brain Metastasis	81.3 ± 2.4	7.1 ± 6.8	4.8 ± 1.3	1.1 ± 0.2	0.7 ± 0.1
Tumor 19	Brain Metastasis	83.1 ± 0.7	22.1 ± 2.3	2.3 ± 1.5	0.5 ± 0.1	0.5 ± 0.0
Average		80.1 ± 6.9	21.9 ± 12.1	5.5 ± 2.7	1.2 ± 0.6	1.0 ± 0.4

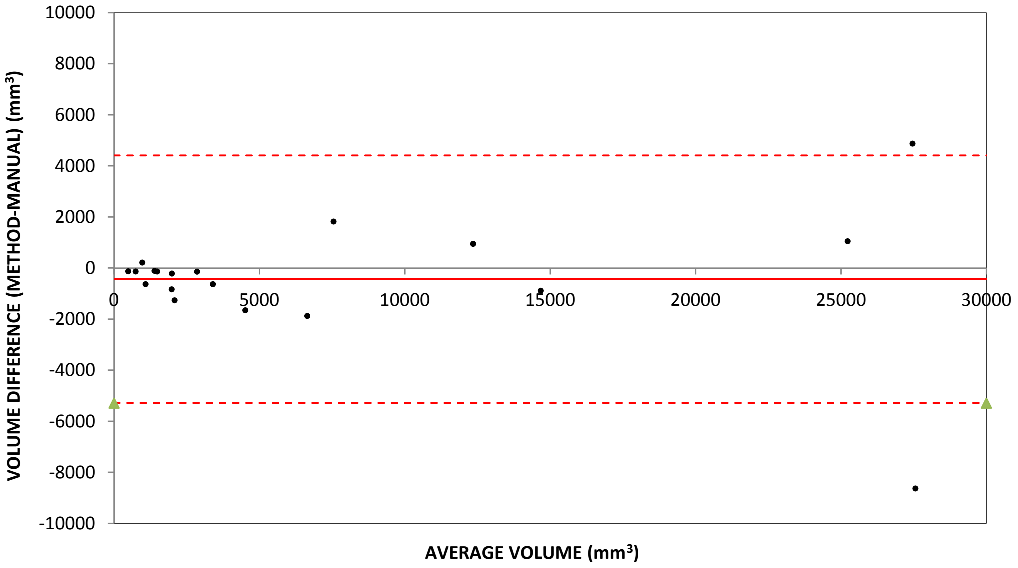

Figure 2.15: Bland-Altman plot of real and estimated tumor volumes on Clinical Data Set. The dashed lines mark ±1.96 standard deviation values of the volume difference whereas the solid line marks its mean.

A Bland-Altman analysis for physical tumor volume measurements is presented in Figure 2.15 which shows that the 90% of the volume differences lie within ±1.96 standard deviations around the mean difference, which is slightly below zero. As we noted before, slight under estimation or over estimation can be possibly due to the expert manual segmentations having a positive or negative bias.

Figure 2.16 presents Dice overlap comparison results among the Graph-cuts, Grow-cut, and the proposed Tumor-cut method. The results we observed with the Graph-cuts approach exhibits similar problems reported before in [30] such as shrinking bias due to minimum cut optimization. The shortest path algorithms, e.g. CA-based methods, showed lack of the shrinking bias problem. The proposed Tumor-cut algorithm exhibits a lower coefficient of variation (std/mean) on the average compared to the other methods used in validation, where the coefficient of variation was 0.5373 (Graph-cuts); 0.0393 (Grow-cut); 0.0238 (Tumor-cut). Paired

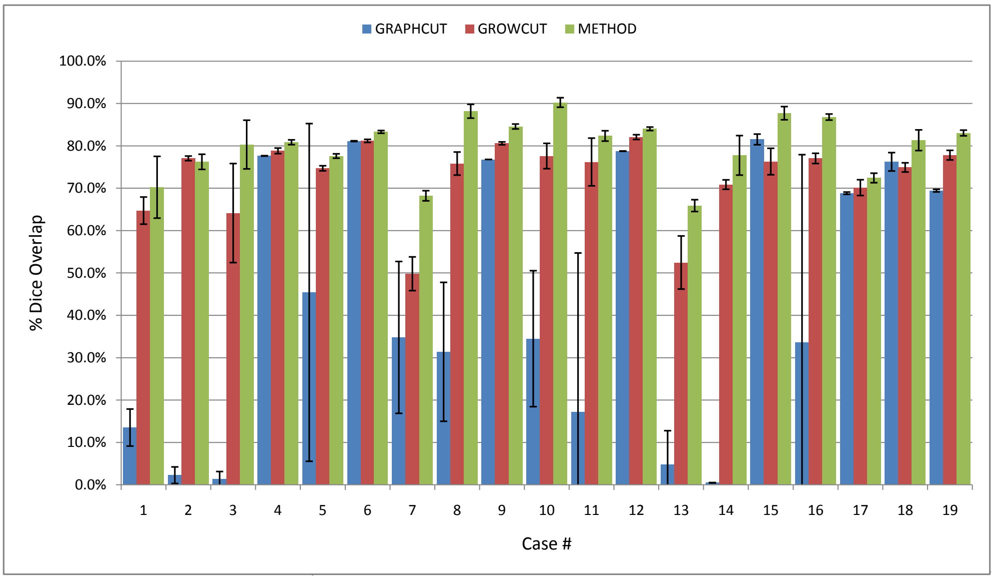

Figure 2.16: Comparison of Dice overlap for Graph-cut, Grow-cut and the proposed method on clinical radio-oncology data set, demonstrates improved overlap with the proposed method over this relatively more challenging tumor data. Black vertical bar indicates ± standard deviation over 5 different initializations.

t-test comparison of Grow-cut and Tumor-cut demonstrates a statistically significant improvement in Dice overlaps ($p = 9.91 \times 10^{-21}$), mean surface distances ($p = 5.37 \times 10^{-11}$) and volume errors ($p = 1.60 \times 10^{-11}$) with the Tumor-cut method.

Qualitative Results

We present 3D qualitative segmentation results from the clinical dataset on sample 2D slices in Figure 2.17. The mixed necrotic and enhancing tumor tissue content, as well as cluttering neighboring structures such as vessels can be observed. These challenging scenarios exemplify the difficulty level in the segmentation problem, for whose solution interactive algorithms are regarded by the physicians as more feasible than fully-automated ones. The level of interaction in the proposed tumor

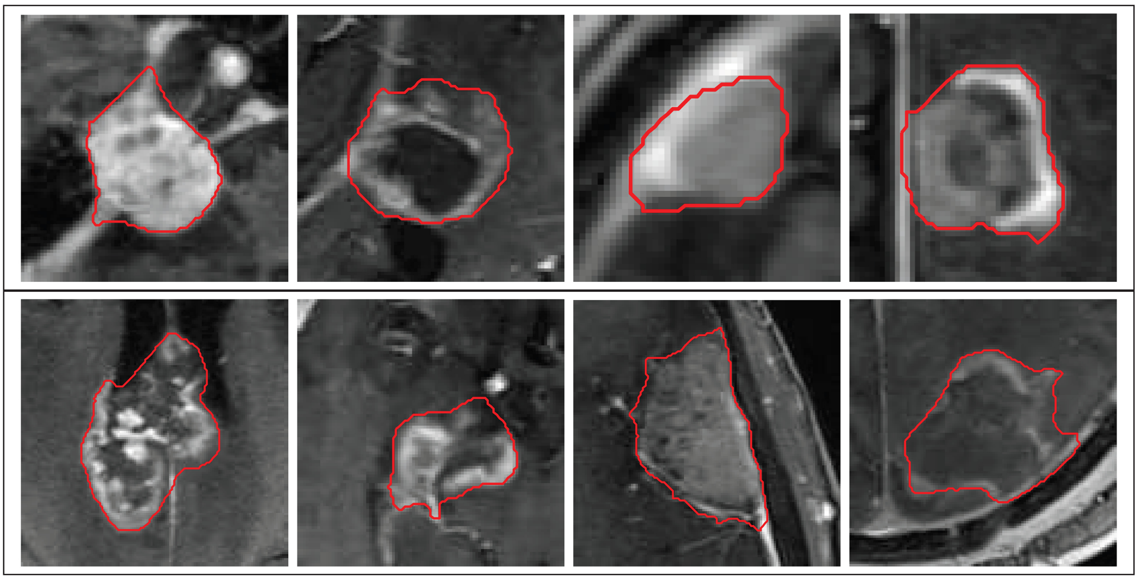

Figure 2.17: Sample slices of segmentation results obtained by the proposed method on challenging cases of the clinical data set.

segmentation algorithm is minimal given by a single line along a 2D axial major diameter of the given tumor. A simple initialization that lasts only 1-2 seconds for the Tumor-cut algorithm, lead to reasonably well tumor delineations, which are of important value in quantification of the volume change, as well as necrotic and enhancing tumor tissue content change between a baseline and follow-up study in the clinics for assessment of radiotherapy response. We present the results of the necrotic tissue segmentation in the next subsection.

2.4.4 Enhancing/Necrotic Core Segmentation Results

In Section 2.3.6, we presented a CA-based method for labeling of necrotic and enhancing tumor tissue content after whole tumor boundary segmentation. We compared the proposed method against EM and Otsu thresholding methods, both of which were based on finding a single “optimal” threshold over the intensity distribution within the tumor volume. In the proposed method, two thresholds are first selected in order to set seeds for the necrotic and enhancing tumor tissue, and afterwards, cellular automata algorithm is run and the results are validated against several 2D slices, over which the necrotic pixels were labeled by the expert radiologist in our team. In order to measure the improvement by imposing connectedness with the proposed CA algorithm, the maximum overlaps obtained using single and double threshold methods are also reported by evaluating the algorithms using every possible threshold values. Even though it is important for the clinicians to have the capacity to quantify the change in the necrotic content of the tumor after radiation therapy, this differentiation within tumor content is not typically carried out in the clinical routine. Table 2.4 presents Dice overlap results of necrotic tissue segmentation for the tumors for which manual labels were available. Although this is a too small dataset to arrive at conclusions, the proposed method performs reasonably well for this problem. Qualitative results are given in Figure 2.18. Typical patterns of dark necrotic core in the center and bright enhancing rim can be observed in rows 2-5, and to an extent in row 1. The result in row 6 gave the lowest performance because small islands of necrotic regions with ambiguous low contrast were missed by all three algorithms.

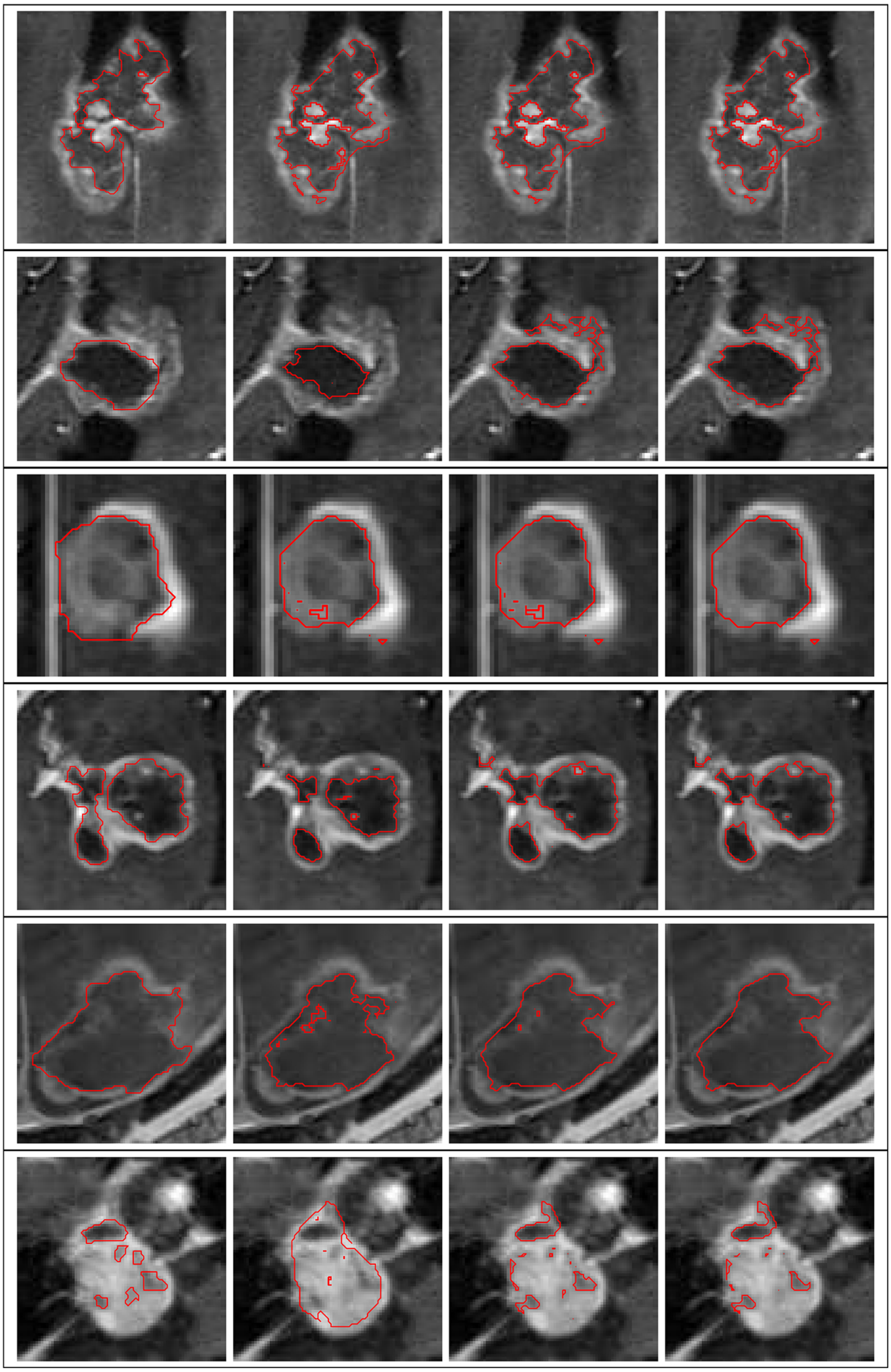

Figure 2.18: Necrotic segmentation results for 6 different tumors on each row. Left-To-Right: Manual Expert Delineation; EM Segmentation; Otsu Thresholding; CA Tumor Segmentation.

Table 2.4: Dice overlap percentages of three necrotic segmentation algorithms with respect to manual expert necrotic labelings.

Tumor ID	Expectation Maximization (%)	Otsu's Method (%)	Max. with Single Threshold (%)	Proposed CA Method (%)	Max. with CA (%)
Tumor 3	83.0	83.4	83.5	83.5	83.7
Tumor 8	73.7	80.0	83.8	80.4	85.6
Tumor 9	84.9	84.5	87.9	87.1	88.1
Tumor 10	74.6	87.5	89.0	87.3	89.6
Tumor 14	85.3	89.7	91.5	90.5	91.6
Tumor 2	42.5	64.6	68.4	59.1	69.0
Median	78.8	83.9	85.8	85.3	86.8

2.5 Conclusion

We presented a segmentation algorithm for the problem of tumor delineation which exhibit varying tissue characteristics. As the change in necrotic and enhancing part of the tumor after radiation therapy becomes important, we also applied the Tumor-cut segmentation to partition the tumor tissue further into its necrotic and enhancing parts. We presented validation studies over a synthetic tumor database and two real tumor databases: one from Harvard tumor repository and another from a clinical database of tumors that underwent radiosurgery planning at Radiation Oncology Department of ASM. The performance over particularly datasets of highly heterogeneous tissue content demonstrated an overlap in the range 80% to 90%, however, with a desired low surface distance error, average median surface distances of $1.0mm$ to $1.5mm$, respectively. Furthermore, performance change over varying initial seeds were also reported as standard deviations, and shown to be important in assessing true robustness of the proposed algorithm in real application scenarios. The user interaction time is just a few seconds and typical computation times vary between 1 second to 16 minutes (on a 3.17GHz dual processor workstation) depending on the volume of the tumor which ranges between 0.5cc and 32cc. Due to inherent parallelity of the proposed algorithm, computation time can be significantly reduced. However, in the case of multiple metastases, user interaction time increases with the number of tumors, as the user should draw one line for each tumor, and for instance such a problem was addressed in RECIST guideline 1.1 [52] which limited the maximum number of tumor cases to be processed to 5.

Strengths of the proposed method include its simple interaction over a single slice and less sensitivity to the initialization (demonstrated by lower coefficient of variation values), its efficiency in terms of computation time, and robustness with respect to different and heterogeneous tumor types. Choosing the contrast enhanced T1 modality limits the application to the tumors that are enhanced with the contrast agent, excluding the edema/infiltration region around the tumor. For the targeted clinical application of radiosurgery planning, using a single modality is an advantage due to the computational efficiency and ease of use. However, in a multimodal scenario, it could be possible to design new transition functions adapted to a given modality and also optimize the parameters. Later, the probability maps constructed from each modality could be combined to obtain the final segmentation. Future work includes assessment of the tumor response to therapy, built on the given segmentation framework, which was encouraged by the clinical experts due to reasonable and acceptable success rates of the algorithm. Attempts presented in this paper to quantify change in necrotic and enhancing tumor tissue content is also welcomed to be of high clinical interest, particularly in radiation oncology practice.

Chapter 3

Multimodal Extension of the Tumor-cut Method and Evaluation on the BraTS Dataset[1]

3.1 Introduction

In Chapter 2, a novel method for segmentation of tumors from a single MRI sequence, the contrast enhanced T1-weighted MRI, is presented. However, incorporation of the multi-modal imaging data from different MR sequences, diffusion MRI, and/or even Positron Emission Tomography (PET), is an emerging approach for tumor segmentation. This would bring a wider spectrum of information with different intensity characteristics from various medical images of for instance different relaxation characteristics as in T1-weighted or T2-weighted MRI. Because of their unpredictable appearance and shape, segmenting brain tumors from multi-modal imaging data is one of the most challenging tasks in medical image analysis. Although many different segmentation strategies have been proposed in the literature, it is hard to compare existing methods because the validation datasets that are used differ widely in terms of input data (structural MR contrasts; perfusion or diffusion data; ...), the type of lesion (primary or secondary tumors; solid or infiltratively growing), and the state of the disease (pre- or post-treatment).

---

[1] The work presented in this chapter appeared in *Proceedings of MICCAI-BRATS 2012 October 1st, Nice, France* and is in preparation for joint paper submission.

In order to gauge the current state-of-the-art in automated brain tumor segmentation and compare between different methods, a multimodal Brain Tumor Segmentation (BraTS) challenge is organized that is held in conjunction with the 15th International Conference on Medical Image Computing and Computer Assisted Intervention (MICCAI 2012) on October 1st, 2012 in Nice, France. For this challenge, a large dataset of brain tumor MR scans including low- or highgrade glioma cases with manually labeled segmentation maps are made publicly available. Additionally, realistically generated synthetic brain tumor datasets are provided for which the ground truth segmentation is known. The details of the available MR images and the expert labeling protocol are given in section 3.3.

Tumor-cut method, which is originally developed for segmentation on contrast enhanced T1 weighted MR modality as described in detail in Chapter 2 and in [53], is extended to process multi modality MR images (see Section 3.2). The BraTS challenge served to evaluate the value of the multi modality Tumor-cut method within the current state-of-the-art techniques.

3.2 Methods

The semi-automatic tumor segmentation method, as described in detail in the "Tumor-cut" article [53] and in Chapter 2, specifically targets the gross tumor volume (GTV) and the necrotic regions of the brain tumors on contrast enhanced T1-weighted MR images, requiring an initialization by drawing a line through the maximum diameter of the tumor as in the "Response Evaluation Criteria In Solid Tumors" (RECIST) guidelines [52]. For the BraTS challenge, the method was extended to multi-modal MRI to include also the labels for edema and non-enhanced regions. Tumor-cut's approach to fuse different MR modalities is to apply the original method to each channel seperately and then combine the segmented volumes by basic set operations based on the type of the modality. For each channel, a segmentation is initialized by drawing the maximum observable diameter of the tumor and performed independently (see Figure 3.1). For FLAIR images, whole hyperintense region is segmented as FLAIR volume (V_{fl}) and for T2 images only the core abnormality is segmented as T2 volume (V_{t2}). Tumor core is segmented on contrast

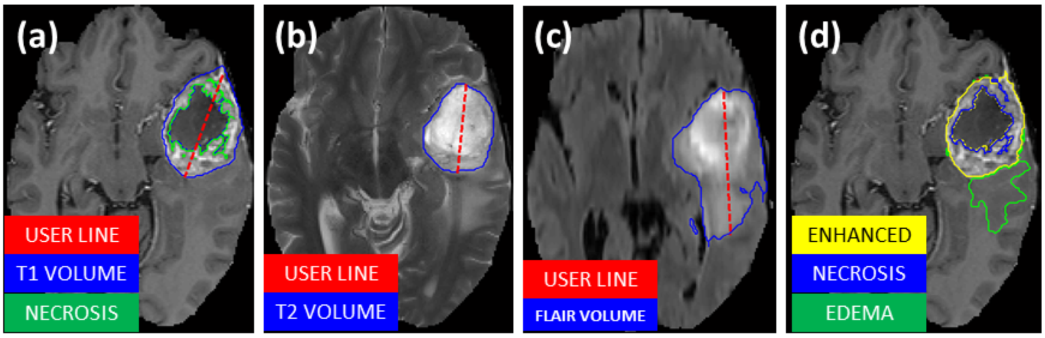

Figure 3.1: Maximum diameter line drawn by the user to initialize the algorithm for CE-T1 (a), T2 (b) and Flair (c) modalities and the corresponding outputs, for a sample high grade case. Manual labels overlayed on T1 for a sample slice (d).

enhanced T1 MRI (V_{t1c}) followed by the application of the necrotic segmentation method to segment the necrotic regions within the tumor core (V_{nec}). For the low grade cases, V_{t1c} and V_{nec} are set to empty, because the tumors were not enhanced by the application of the contrast agent. Non-contrast enhanced T1 MR images were used neither for high nor low grade cases. For FLAIR segmentation, only the weight of the regularizer in the energy term for the level-set evolution is tuned to allow resulting tumor surfaces to have higher curvatures. Label for each class is determined by the following operations:

$$\begin{aligned} Necrotic &= V_{nec} \\ Enhanced &= V_{t1c} \setminus V_{nec} \\ Non-enhanced &= V_{t2} \setminus V_{t1c} \\ Edema &= V_{fl} \setminus (V_{t2} \cup V_{t1c}) \end{aligned} \tag{3.1}$$

For each case, user interaction takes about 1-2 minutes and typical run time is around 10-30 minutes, depending on the size of the tumor, using a CPU (3.16 GHz). However, the parallel nature of the algorithm allows GPU implementation, which would reduce the processing time significantly.

3.3 BraTS Dataset[2]

The first version of the dataset, which was used in the BraTS challenge in MICCAI, consists of two label manual segmentation including edema and tumor core. After a few months, the performances of the algorithms were evaluated on an improved dataset consisting of 4-labels as described in detail in the following sections.

3.3.1 Image Types Used for Segmentation

The MR images used for tumor segmentation are given in the following list:

- **T1-Weighted.** T1-weighted, native image, sagittal or axial acquisitions, variable slice thickness from 1 to 5 mm.
- **Contrast Enhanced T1-Weighted:** T1-weighted, post Gd image. Axial 3D acquisition, 1 mm isotropic voxel size.
- **T2-Weighted.** T2-weighted image, axial 2D acquisition, 2-4 mm slice thickness.
- **T2-Weighted Fluid Attenuated Inversion Recovery (FLAIR).** T2-weighted FLAIR image, axial or coronal or sagittal 2D acquisitions.

The images were taken from multiple centers and multiple scanners, therefore image quality and acquisition parameters differ. Although the original acquisition parameters are heterogeneous, all images are co-registered to the post-contrast T1 image and re-sampled to 1 mm.

3.3.2 Label Definitions

Although the general problem of defining tumor borders in infiltrative tumors still exists, particular radiological criteria can be set to define such sub-domains. These

---

[2] Brain tumor image data used in this work were obtained from the MICCAI 2012 Challenge on Multimodal Brain Tumor Segmentation (http://www.imm.dtu.dk/projects/BRATS2012) organized by B. Menze, A. Jakab, S. Bauer, M. Reyes, M. Prastawa, and K. Van Leemput. The challenge database contains fully anonymized images from the following institutions: ETH Zurich, University of Bern, University of Debrecen, and University of Utah.

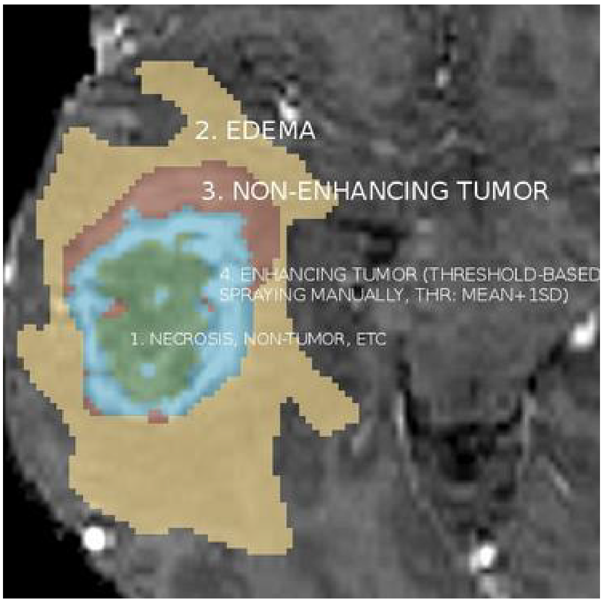

Figure 3.2: Tumor labels overlayed on a sample slice of a typical high grade glioma case. Green: Non-brain, non-tumor, necrosis, cyst, hemorrhage (1). Yellow: Surrounding edema (2). Brown: Non-enhancing tumor part (3). Blue: Enhancing tumor core (4).

domains do not reflect strict biological correspondence and homogeneity but are rather place-holders for similarly-looking regions. For instance, the definition of the active tumor could simply be the high signal intensity regions on T1 Gd images. However, in high grade tumors, there are non-necrotic, non-cystic regions that do not enhance but they can be clearly separable from the surrounding edema. Another problem is the definition of tumor center in low grades. In such cases, a certain delimitation of the T2 hyperintense surrounding edema and the growing tumor is sometimes possible, but they do not enhance. Therefore as shown in Figure 3.2, the following set of labels is used to define intra tumoral sub-domains:

- **Label 1.** Non-brain, non-tumor, necrosis, cyst, hemorrhage
- **Label 2.** Surrounding edema
- **Label 3.** Non-enhancing tumor part
- **Label 4.** Enhancing tumor core

The definitions for labels 1,2 and 4, which are necrosis, edema and enhancing tumor respectively are relatively common and easy to identify, whereas the label 3

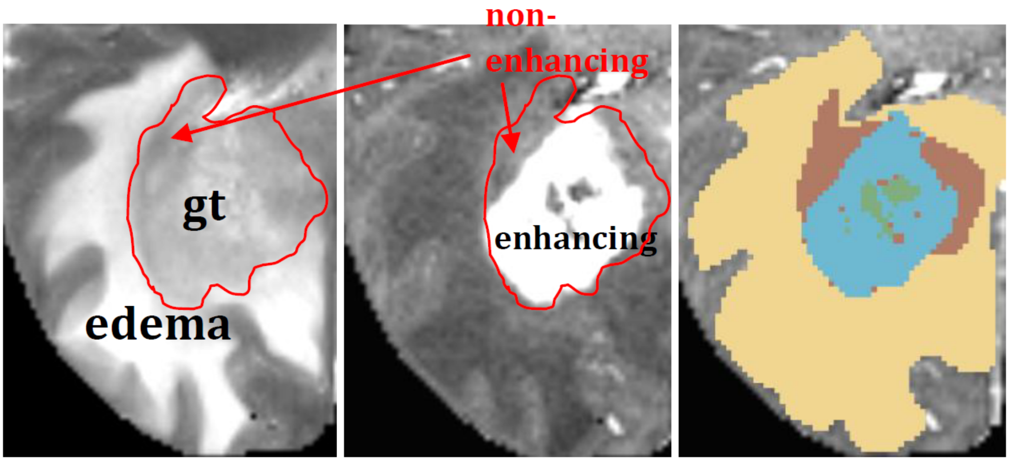

Figure 3.3: Definition of the label 3 for high grade glioma cases. Left: Gross tumor and edema regions are distinguishable on T2 images with different intensity and texture characteristics. Center: Enhancing tumor volume, which appears hyper-intense on contrast enhanced T1 weighted MR images, do not completely overlap with gross tumor volume on T2-weighted images. Right: Corresponding labeling where the region that is not enhanced with the contrast agent but appears as a part of the gross tumor in T2 is labeled as non-enhancing in brown color (label 3).

might be confusing. The non-enhancing tumor core is the only category used for delineating tumor centers in low grade gliomas, for there occurs no enhancement in contrast enhanced T1 images. However, in high grade glioma cases, identification of those non-enhancing regions of the tumor core requires parallel viewing of T1 and T2 images as shown in Figure 3.3. The region that is not enhanced with the contrast agent but appears as a part of the gross tumor in T2 is categorized as non-enhancing tumor core and labeled with 3.

3.4 Results

The method is implemented on Matlab environment, running on a windows 7 workstation, using mex files for core algorithms. The dataset is downloaded from the "Virtual Skeleton Database" web site (http://www.virtualskeleton.ch/) and the online system provided is used for the evaluation.

Both of the 2-label and 4-label dataset, are divided into two parts as "Training Dataset" and "Testing Dataset". The manual labels of the training data were provided offline to participants of the BraTS challenge as a ground truth to train and tune the algorithms. The segmentation maps obtained on the MR images of the test dataset are uploaded to the “Virtual Skeleton” server and the segmentation performance measures are calculated by comparing with the ground truth, which is hidden to the participants.

The results for each case of the “2-Label Training Dataset” are provided in Section 3.4.1. The overall results, for the 2-label (Section 3.4.1) and 4-label (Section 3.4.2) test/training datasets are given, compared to the performance of the other techniques participated in BraTS Challenge.

3.4.1 Results on 2-Label Dataset

For each subset of the BraTS 2-Label Training Dataset, including high grade and low grade, simulated and patient data, the Dice overlap scores obtained are given as bar charts in Figs 3.4-3.7. For the 2-Label ”Testing Dataset”, which consists of 4 low grade and 11 high grade glioma cases, the results are given in Figs 3.8 and 3.9.

The overall Dice overlap, Jaccard scores, Sensitivity and Specificity results with the standard deviations are reported in Table 3.1. The comparison of the Dice scores obtained by tumor-cut method with the other techniques participated in the BraTS challenge is given in Table 3.2.

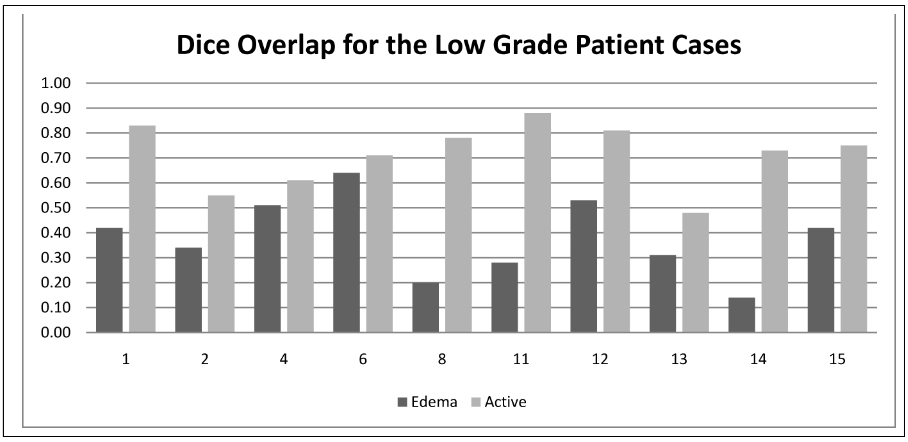

Figure 3.4: Dice overlap results obtained on each case of the low-grade patient subset of the 2-Label Training Dataset.

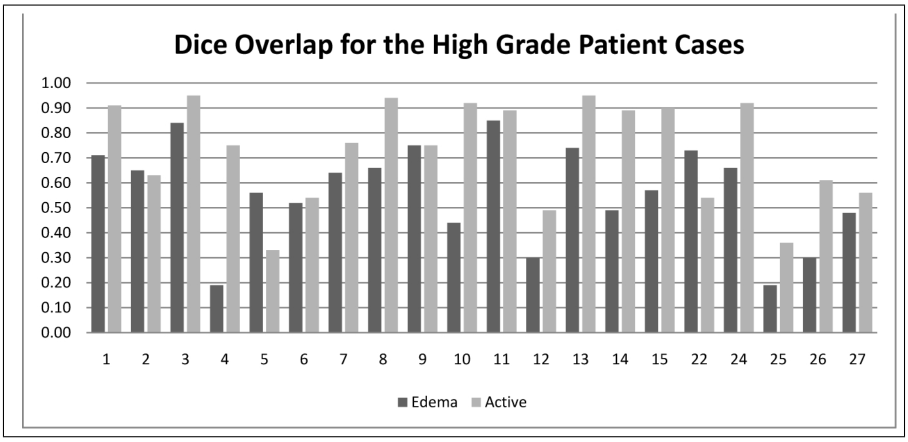

Figure 3.5: Dice overlap results obtained on each case of the high-grade patient subset of the 2-Label Training Dataset.

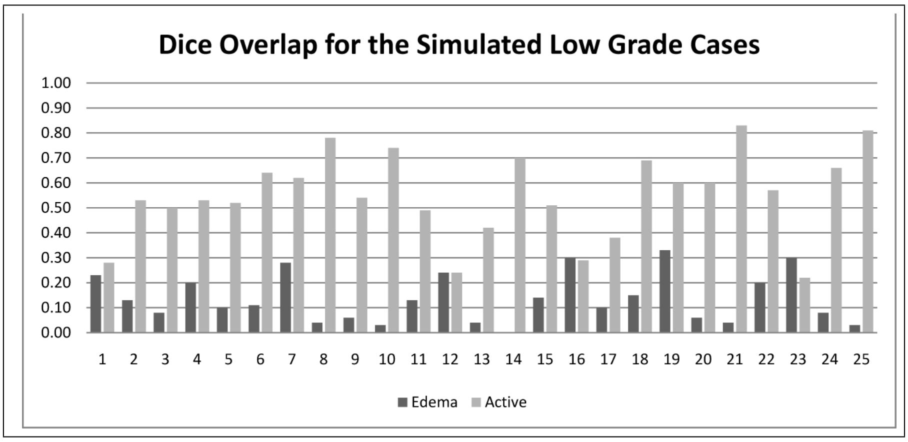

Figure 3.6: Dice overlap results obtained on each case of the simulated low-grade subset of the 2-Label Training Dataset.

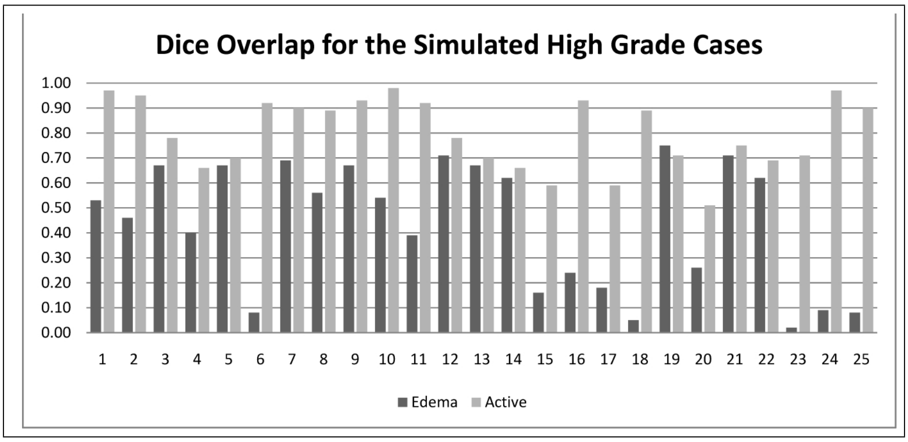

Figure 3.7: Dice overlap results obtained on each case of the simulated high-grade subset of the 2-Label Training Dataset.

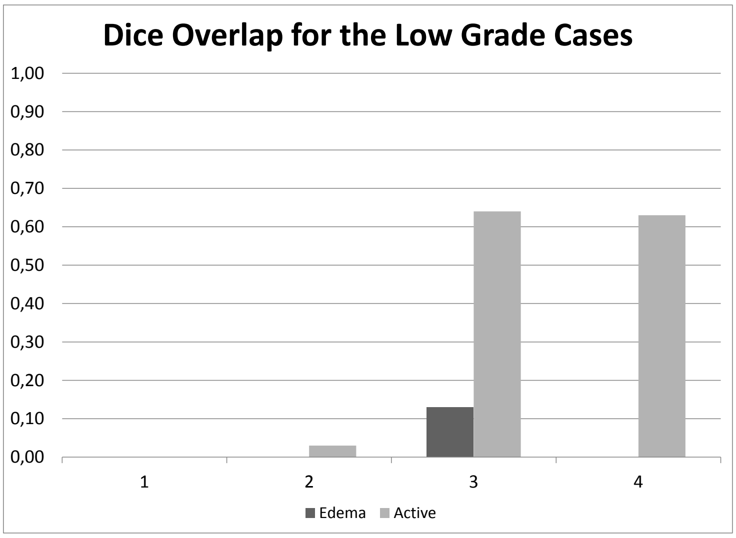

Figure 3.8: Dice overlap results obtained on each case of the low-grade patient subset of the 2-Label Testing Dataset.

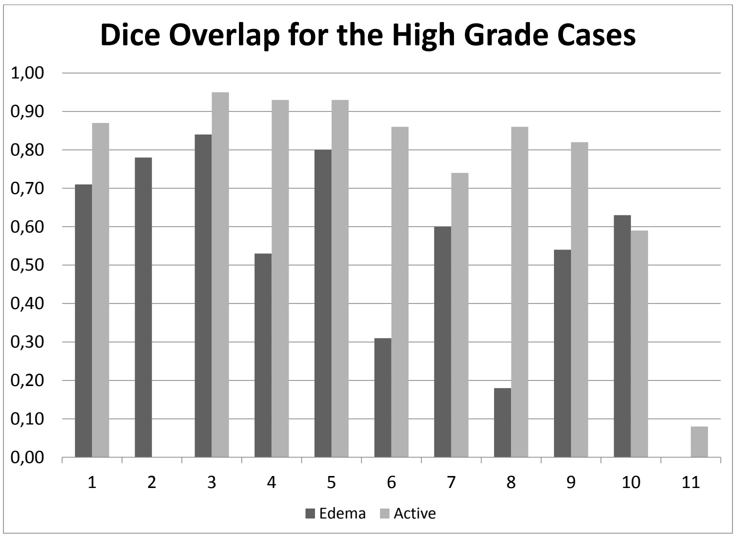

Figure 3.9: Dice overlap results obtained on each case of the high-grade patient subset of the 2-Label Testing Dataset.

Table 3.1: Average and standard deviation of the dice overlap, jaccard, specificity and sensitivity results obtained on the 2-label BraTS dataset.

	Dice Overlap Edema / Tumor	Jaccard Score Edema / Tumor	Specificity Edema / Tumor	Sensitivity Edema / Tumor
Training Data	$0.37 \pm 0.25/0.69 \pm 0.19$	$0.25 \pm 0.20/0.56 \pm 0.23$	$0.99 \pm 0.01/1.00 \pm 0.00$	$0.54 \pm 0.33/0.86 \pm 0.19$
Testing Data (Low Grade)	$0.03 \pm 0.00/0.32 \pm 0.10$	$0.02 \pm 0.00/0.24 \pm 0.05$	$1.00 \pm 0.00/0.99 \pm 0.00$	$0.02 \pm 0.00/0.42 \pm 0.14$
Testing Data (High Grade)	$0.54 \pm 0.07/0.69 \pm 0.11$	$0.41 \pm 0.05/0.61 \pm 0.09$	$0.99 \pm 0.00/1.00 \pm 0.00$	$0.75 \pm 0.07/0.69 \pm 0.11$

Table 3.2: Tumor core and edema dice overlap percentages on 2-label testing dataset for the participated groups of the BraTS Challenge.

Method	High Grade Cases (Tumor Core / Edema)	Low Grade Cases (Tumor Core / Edema)
Hamamci et al.	69.4 / 53.9	32.4 / 3.3
Shin et al.	14.4 / 3.8	23.2 / 6.1
Bauer et al.	51.2 / 53.6	33.2 / 17.9
Zikic et al.	47.6 / 59.8	33.9 / 32.4
Subbanna et al.	13.3 / 6.9	0.1 / 0.0
Xiao et al.	33.7 / 53.9	22.4 / 27.9
Zhao et al.	5.8 / 0.3	0.0 / 0.0

3.4.2 Results on 4-Label Dataset

The 4-label patient dataset is divided into two parts as "Training Dataset" and "Testing Dataset", that consist of 30 (10 low, 20 high grade) and 15 (4 low, 11 high grade) glioma cases respectively. The evaluation is done for 3 different tumor sub-compartments, which are a combination of the 4-labels defined in Section 3.3.2, as follows:

- **Region 1:** Complete Tumor (Edema + Enhancing + Non-enhancing + Necrosis)
- **Region 2:** Tumor Core (Enhancing + Non-enhancing + Necrosis)
- **Region 3:** Enhancing Tumor[3] (Enhancing)

The average dice overlap, jaccard scores, specificity and sensitivity results with the standard deviations for each subset of the 4-label dataset are reported in Table 3.3. The comparison of the dice scores, positive predictive values and sensitivity results obtained by tumor-cut method with the other techniques participated in the BraTS challenge for testing and training datasets are given in Tables 3.4 and 3.5 respectively.

---

[3] Enhancing tumor region is not evaluated for the low grade glioma cases.

Table 3.3: Average and standard deviation of the dice overlap, jaccard, specificity and sensitivity results obtained on the 4-label BraTS dataset.

	Dice Overlap			Jaccard Score			Specificity			Sensitivity		
	complete	core	enhancing	complete	core	enhancing	complete	core	enhancing	complete	core	enhancing
Testing - Low	0.55 ± 0.13	0.40 ± 0.13	-	0.46 ± 0.11	0.32 ± 0.10	-	0.49 ± 0.13	0.33 ± 0.10	-	0.71 ± 0.17	0.71 ± 0.17	-
Testing - High	0.78 ± 0.02	0.63 ± 0.03	0.59 ± 0.05	0.65 ± 0.02	0.48 ± 0.03	0.45 ± 0.05	0.72 ± 0.03	0.57 ± 0.04	0.63 ± 0.07	0.91 ± 0.02	0.85 ± 0.07	0.70 ± 0.05
Training - Low	0.86 ± 0.01	0.70 ± 0.02	-	0.77 ± 0.02	0.56 ± 0.03	-	0.84 ± 0.01	0.70 ± 0.03	-	0.89 ± 0.01	0.77 ± 0.05	-
Training - High	0.79 ± 0.02	0.68 ± 0.03	0.66 ± 0.05	0.68 ± 0.04	0.54 ± 0.03	0.52 ± 0.04	0.75 ± 0.03	0.60 ± 0.04	0.72 ± 0.07	0.89 ± 0.02	0.88 ± 0.02	0.64 ± 0.05

Table 3.4: Dice overlap, positive predictive value and sensitivity scores for complete tumor, tumor core and enhancing regions on the 4-label testing dataset for the participated groups of the BraTS Challenge.

	Dice			Positive Predictive Value			Sensitivity		
	complete	core	enhancing	complete	core	enhancing	complete	core	enhancing
Nagesh Subbanna	0.75 (4)	0.70 (1)	0.43 (2)	0.69 (6)	0.75 (1)	0.41 (5)	0.90 (1)	0.69 (3)	0.57 (2)
Liang Zhao	0.82 (1)	0.66 (2)	0.36 (7)	0.86 (1)	0.72 (3)	0.29 (8)	0.80 (6)	0.73 (2)	0.60 (1)
Darko Zikic	0.75 (3)	0.47 (6)	0.41 (4)	0.79 (3)	0.72 (2)	0.46 (2)	0.79 (8)	0.44 (7)	0.44 (7)
Andac Hamamci	0.72 (5)	0.57 (3)	0.43 (1)	0.66 (7)	0.51 (8)	0.46 (1)	0.86 (2)	0.81 (1)	0.51 (3)
Stefan Bauer	0.66 (7)	0.49 (5)	0.42 (3)	0.63 (8)	0.63 (4)	0.41 (4)	0.80 (7)	0.49 (6)	0.45 (6)
Bjoern Menze	0.69 (6)	0.33 (7)	0.39 (6)	0.78 (4)	0.57 (6)	0.42 (3)	0.67 (9)	0.29 (8)	0.46 (5)
Raphael Meier	0.65 (8)	0.51 (4)	0.39 (5)	0.62 (9)	0.56 (7)	0.37 (6)	0.81 (5)	0.59 (5)	0.47 (4)
Ezequiel Geremia	0.62 (9)	0.32 (8)	0.31 (8)	0.80 (2)	0.60 (5)	0.36 (7)	0.56 (10)	0.28 (10)	0.32 (8)
Ines Njeh	0.77 (2)	0.21 (9)	0.00 (10)	0.77 (5)	0.22 (9)	0.00 (10)	0.84 (3)	0.29 (9)	0.00 (10)
Hoo-Chang Shin	0.30 (10)	0.17 (10)	0.04 (9)	0.23 (10)	0.12 (10)	0.04 (9)	0.83 (4)	0.66 (4)	0.06 (9)

Table 3.5: Dice overlap, positive predictive value and sensitivity scores for complete tumor, tumor core and enhancing regions on the 4-label training dataset for the participated groups of the BraTS Challenge.

	Dice			Positive Predictive Value			Sensitivity		
	complete	core	enhancing	complete	core	enhancing	complete	core	enhancing
Syed Reza	0.92 (1)	0.91 (2)	0.68 (1)	0.97 (1)	0.95 (1)	0.70 (1)	0.89 (5)	0.88 (2)	0.66 (1)
Darko Zikic	0.92 (2)	0.93 (1)	0.63 (2)	0.86 (4)	0.92 (2)	0.63 (4)	0.98 (1)	0.94 (1)	0.64 (2)
Nick Tustison	0.88 (3)	0.76 (3)	0.55 (3)	0.88 (2)	0.80 (6)	0.65 (3)	0.89 (4)	0.79 (4)	0.53 (3)
Liang Zhao	0.86 (4)	0.75 (4)	0.55 (4)	0.88 (3)	0.86 (4)	0.65 (2)	0.86 (7)	0.72 (5)	0.50 (6)
Raphael Meier	0.80 (6)	0.66 (6)	0.53 (5)	0.77 (8)	0.71 (8)	0.56 (7)	0.85 (8)	0.68 (7)	0.52 (4)
Andac Hamamci	0.81 (5)	0.69 (5)	0.49 (8)	0.78 (7)	0.63 (9)	0.54 (8)	0.89 (3)	0.85 (3)	0.46 (8)
Nagesh Subbanna	0.78 (8)	0.66 (7)	0.46 (9)	0.66 (9)	0.87 (3)	0.62 (5)	0.97 (2)	0.56 (9)	0.40 (9)
Stefan Bauer	0.79 (7)	0.64 (8)	0.49 (7)	0.79 (5)	0.74 (7)	0.54 (9)	0.82 (9)	0.61 (8)	0.49 (7)
Thomas Taylor	0.68 (9)	0.62 (9)	0.52 (6)	0.78 (6)	0.83 (5)	0.60 (6)	0.62 (10)	0.53 (10)	0.50 (5)
Hoo-Chang Shin	0.46 (10)	0.36 (10)	0.35 (10)	0.35 (10)	0.27 (10)	0.35 (10)	0.86 (6)	0.69 (6)	0.39 (10)

3.5 Discussion and Conclusions

Originally we limited the scope of the “Tumor-cut” algorithm to the contrast enhanced gross tumor volumes, which corresponds to the tumor core of the high grade tumors in Table 3.2. The comparison of the performance with the other participating algorithms shows that the “Tumor-cut” performs superior to others for the segmentation of the tumor core of high grade glioma cases, whereas perform similar for other categories, except edema segmentation of the low grade tumors, which is usually not of interest in low grade gliomas.

For the 4-label challenge results given in 3.4, “Tumor-cut” algorithm performed comparable to the state-of-the-art techniques participated in the challenge. Because, the “Tumor-cut” method is not based on learning on the training dataset, the results obtained for both training and testing datasets are similar as expected. However, the low ranking in Table 3.5 is possibly due to the learning-based biased performance evaluation of the other algorithms.

Disadvantages of the interactive segmentation algorithms in general can be noted as: increased processing time and the possibility to miss some in case of multiple tumors, difficulty in batch processing of patient databases and intra/inter operator variability.

We observed that in one case only, we segmented an abnormal structure, which was not labeled as tumor by the experts. Although, this resulted a zero overlap score for the particular case, in fact, to allow user to choose what to segment is an advantage of the semi-automatic approach. In general, the T2 results did not provide useful information, as only a small portion of the tumors consist of the non-enhancing region and the segmentation results were not accurate due to the low contrast between tumor core and edema. The approach of “Tumor-cut” method was to apply the original algorithm independently to each modality. A combined algorithm that considers the multidimensional information from all available modalities have the potential to improve the results obtained.

Chapter 4

Potential Tumor Response Criteria based on the Invariants of the Finite Strain Tensor[1]

4.1 Tumor Follow-up

The work on developing a common language, in order to evaluate the therapy responses of the tumors in an objective and consistent manner, was accelerated after mid 1970's. For this purpose, the World Health Organization (WHO) criteria titled "Reporting results of cancer treatment" which is published by World Health Organization (WHO) in 1979 [54] and by Miller et.al. in 1981 [55] were widely used as a standard in the studies. WHO criteria proposes to calculate the total tumor load to determine the treatment response by multiplying the maximum diameter in any of the three orthogonal planes (axial, sagittal or coronal) and the maximum diameter in the perpendicular plane for each tumor and summing up over measurable lesions (2 dimensional). The measurement of the tumor load should be done at the beginning of the treatment and with equal time interval follow-ups by the same method. Whenever the accurate measurement in 2 dimensions is not possible, only the the single longest diameter of the tumor would be reported. Treatment responses for the measurable diseases are classified under 4 categories:

---

[1] The work presented in this chapter appeared in the *European Society of Magnetic Resonance in Medicine and Biology (ESMRMB) Conference, 2012.*

- Complete Response (CR): The disappearance of all known disease.
- Partial Response (PR): No new lesion, no progression of any lesion and at least 50% decrease in total tumor load.
- Progressive Disease (PD): A 25% or more increase in the size of any measurable lesions or the appearance of new lesions.
- No change (NC): No response or progression.

Complete and partial responses should be verified by a second measurement following the observation. [47].

In 1990, after the publication of the application of WHO criteria on brain tumors by Macdonald et.al., MacDonald criteria became a standart used on brain tumor studies [10, 11].

However, summing up the multiplication of bidimensional measurements, needs excessive workload and the results are error-prone and causes some problems about the usage of the WHO criteria [56, 57, 58]:

1. The usage of the tumor size changes in response evaluation varies between research groups.
2. The number of lesions and the minimum lesion sizes noted shows variations.
3. "Progessive Disease (PD)" is defined on a single lesion by some groups, while calculated on total tumor load by some other groups.
4. The technological development of the measurement devices (Computed Tomography and Magnetic Resonance Imaging), causes confusions on how to use 3-dimensional measurements on tumor response studies.

Addressing those problems, in the mid 1990's, a study is initiated to develop a new set of criteria by "The European Organization for Research and Treatment of Cancer (EORTC)", "The National Cancer Institute (NCI) of the United States", and "The National Cancer Institute of Canada, Clinical Trials Group" and published in the year 2000, under the name Response Evaluation Criteria in Solid Tumors (RECIST) [59]. In this widely used RECIST tumor response criteria, the maximum diameter of the tumor measured in any plan is used for tumor follow-up. Comparison studies revealed that the overall results obtained by unidimensional measurements of a single maximum diameter (RECIST) are equivalent to the bidimensional WHO criteria [56, 59, 58, 60].

In this chapter, as well as the global criteria such as diameter and volume measurements, the potential of the local criteria on assessment of the tumor evolution is studied and explained in the following section.

4.2 Deformable Registration for Tumor Follow-up

The first step in assessment of the tumor evolution between consecutive MR images of the patient locally and accurately is the alignment of the MR volumes by a rigid registration. One of the state-of-the-art rigid alignment techniques such as a normalized cross correlation-based registration could be applied (e.g. using SPM toolbox Rigid Registration). However, for an intra-patient alignment problem, which involves registration of MR volumes of the same patient at different time points (e.g. before and after therapy) with varying degrees of tumor tissue of highly heterogeneous characteristics, an anatomic landmark-based rigid registration was developed by Demir et.al. [61], which could be utilized in our pre-alignment phase. In this study, “Block Matching” algorithm of the MedINRIA software is used for rigid registration of the reference and follow-up contrast enhanced T1 MR volumes of the tumor patient.

After the rigid alignment of the reference and follow-up volumes of the tumor patient, a deformable registration is proposed to be used, to create a mapping ($\boldsymbol{A}(\boldsymbol{x}) : \Omega \rightarrow \Omega$ where $\Omega \in \mathbf{R}^3$ is the domain of the image volume) between the binary tumor volumes on both images obtained by the Tumor-cut segmentation algorithm. Diffeomorphic Demons algorithm, which is one of the most accurate and robust registration algorithms in the literature is used to create a deformation map from the reference tumor to the follow-up tumor [1]. Diffeomorphic demons algorithm, which is based on Thirion’s Demons algorithm [62], can be interpreted as an optimization procedure in the space of displacement vectors. Deformable transformation, which is defined by the displacement vectors ($\boldsymbol{u} : \mathbf{R}^3 \rightarrow \mathbf{R}^3$) for each voxel on the image space ($\boldsymbol{A}(\boldsymbol{x}) = \boldsymbol{x} + \boldsymbol{u}$), is calculated by using the intensity based forces obtained from the image. Following the construction of the displacement vectors for each voxel, the resulting displacement field is regularized by using Gaussian smoothing. Demons iterations can be summarized by the following:

1. Displacement field is initialized to $\boldsymbol{s}$.
2. By using SSD (sum of square differences) the displacement field $\boldsymbol{u}$ between F (reference) and M (moving image) is optimized by minimizing the norm:

   $$E_{corr}(\boldsymbol{u}) = \| F - M(\boldsymbol{s} + \boldsymbol{u}) \|^2 + \| \boldsymbol{u} \|^2 \tag{4.1}$$

   where F denotes the referrence (static) volume and M is the moving volume.
3. Vector field is updated by: $\boldsymbol{c} \longleftarrow \boldsymbol{s} + \boldsymbol{u}$
4. Vector field $\boldsymbol{c}$ is regularized by Gaussian smoothing: $\boldsymbol{s} \longleftarrow G(\boldsymbol{c})$

The iterations 1-4 above is finalized when the update of the estimated vector field lowers below a treshold. Although the Demons algorithm works efficiently, it has some limitations in terms of similarity measures and transformation constraints. One of the improvements in the literature, addressing those problems, is the "Diffeomorphic Demons" algorithm [1]. In diffeomorphic registration, not only the intensity differences but also the transformation properties are considered, to obtain a topology preserving transformation.

Mathematically, a diffeomorphism; is an invertable function which maps a differentiable manifold to another. Both the function and its inverse are smooth functions, which preserves the topology of the anatomical regions. Meanwhile, a one-to-one and invertable mapping is obtained without foldings of the function. In order to assure the diffeomorphism, the vector field is calculated in Lie space in Diffeomorphic Demons algorithm [1]. When the transformations are summed basically, as in the summation (+) operation given in the 3rd step above, the result is not guaranteed to belong to the same space, for they do not form a vector space. Instead of using a basic summation, if a composition (o) is done by using Lie group structure, the transformation estimated by the 3rd step given below would be preserved in the vector space.

The iterations of the Diffeomorphic Demons algorithm can be summarized as following:

1. Displacement field is initialized to $\boldsymbol{s}$.

2. By using SSD (sum of square differences) the displacement field $\boldsymbol{u}$ between F (reference) and M (moving image) is optimized by minimizing the norm:

$$E_{corr}(\boldsymbol{u}) = || F - M(\boldsymbol{s} \circ \exp(\boldsymbol{u})) ||^2 + || \boldsymbol{u} ||^2 \tag{4.2}$$

   where F denotes the referrence (static) volume and M is the moving volume.

3. Vector field is updated by: $\boldsymbol{c} \longleftarrow \boldsymbol{s} \circ \exp(\boldsymbol{u})$

4. Vector field $\boldsymbol{c}$ is regularized by Gaussian smoothing: $\boldsymbol{s} \longleftarrow G(\boldsymbol{c})$

An example comparing the classical Demons algorithm and the Diffeomorphic Demons algorithm is given in Figure 4.1. Here, F denotes the referrence (static) volume and M is the moving volume. It can be seen that the topology of the reference volume is preserved better by the Diffeomorphic Demons algorithm.

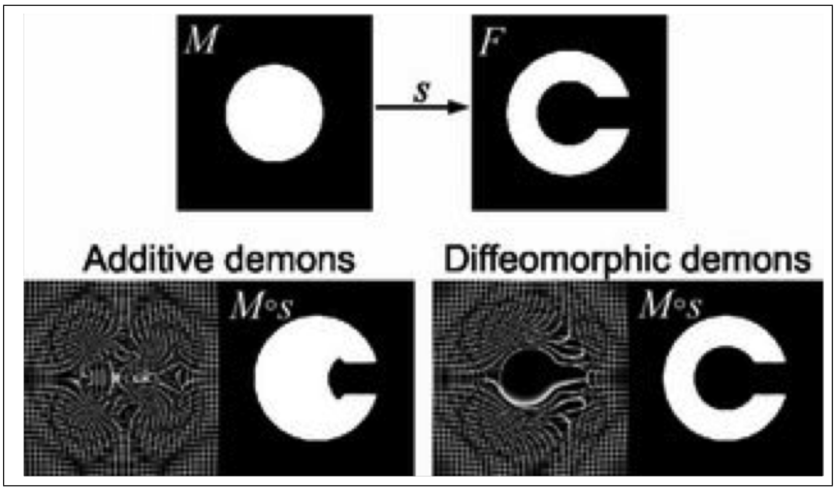

Figure 4.1: Comparison of the classical Demons and the Diffeomorphic Demons algorithms.

In Figure 4.2, the same sample slice of the reference and follow-up contrast enhanced T1 images of a tumor patient are shown. Here, it can be seen that the volume and diameter of the tumor is decreased after the treatment. First, Diffeomorphic Demons deformable registration algorithm is applied to register the reference and follow-up contrast enhanced T1 weighted MR images of the brain tumor patients. However, the results were not successful. Briefly, the displacement vector field obtained by using the voxel intensity values of the reference and follow-up volumes was not able to map the tumor volume before the therapy to the tumor volume after the therapy. One of the possible reasons for this failure is thought to be the effect of the deformation caused by the background and surrounding structures on the deformation of the tumor region.

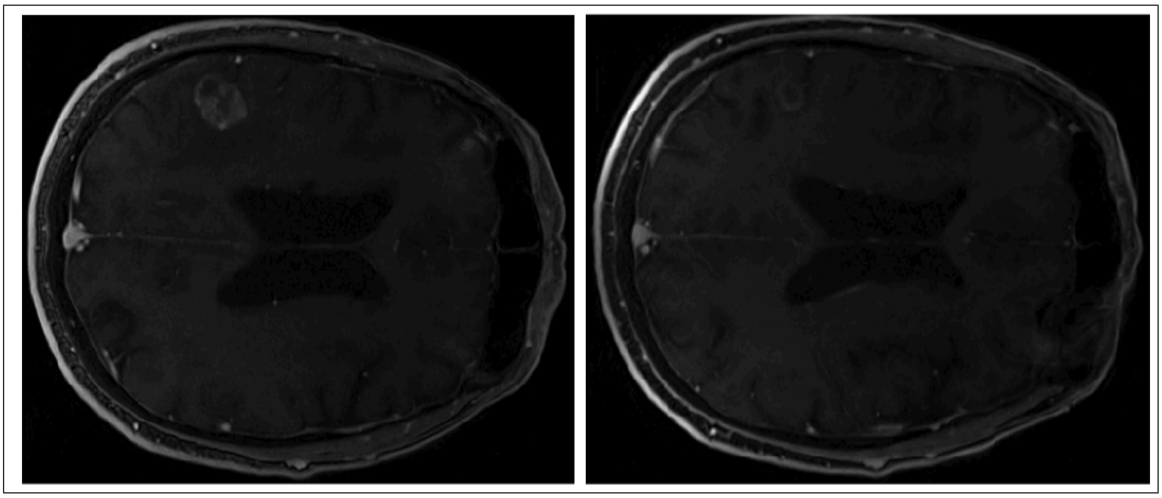

Figure 4.2: Left: Tumor of a patient on the reference scan before the therapy; Right: The same tumor on the follow-up slice.

In order to solve the encountered problem of intensity based registration, the tumors on both reference and follow-up volumes are segmented and then the Diffeomorphic Demons algorithm is applied to determine the deformation field between the tumor surfaces. To segment the tumors on both volumes, Tumor-cut algorithm described in detail in Chapter 2 and in [43] is applied. Contours of the tumor on both reference and follow-up images are overlayed on a sample slice of the reference MRI in Figure 4.3.

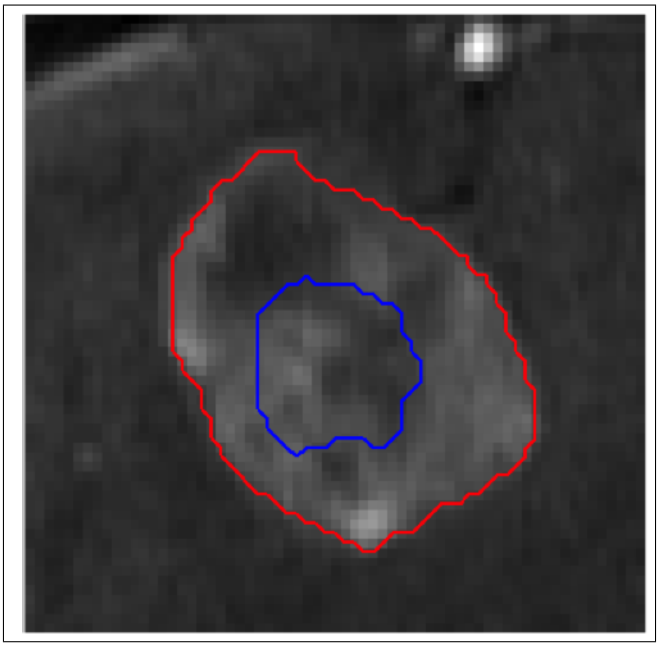

Figure 4.3: Red: Contour of the tumor in reference scan. Blue: Contour of the tumor in follow-up scan, overlayed on the reference MRI.

4.3 Deformation Gradient, Lagrange Strain Tensor, and its Invariants

After obtaining the segmented binary tumor maps on both MR volumes, "Diffeomorphic Demons" deformable registration algorithm is applied to estimate a smooth deformation field between the reference and follow-up binary tumor volumes [1]. The displacement field is defined as on each voxel of the moving (follow-up) volume mapping to the static (reference) volume: $\boldsymbol{X} = \boldsymbol{A}(\boldsymbol{x})$, $\boldsymbol{x}$: denote the coordinates in moving frame where, $\boldsymbol{X}$ are the coordinates in the constant volume. Deformation field $\boldsymbol{A}(\boldsymbol{x})$, can be written in terms of displacement field $\boldsymbol{u}(\boldsymbol{x})$ as:

$$\boldsymbol{A}(\boldsymbol{x}) = \boldsymbol{x} + \boldsymbol{u}(\boldsymbol{x}) \tag{4.3}$$

To calculate the total deformation of the tumor, which is related to the amount of shape change, tensors used in the field of continuum mechanics are used (e.g. see [63]). The differential relation between the static and moving coordinate frames are given as:

$$d\boldsymbol{X} = \boldsymbol{F}\, d\boldsymbol{x} \tag{4.4}$$

where $\boldsymbol{F}$ is known as Jacobian, or the deformation gradient:

$$\boldsymbol{F} = \frac{\partial \boldsymbol{A}}{\partial \boldsymbol{x}} \tag{4.5}$$

$\boldsymbol{F}$ can be calculated by using the estimated displacement field:

$$\boldsymbol{F} = \boldsymbol{I} + \nabla_x \boldsymbol{u} \tag{4.6}$$

In equation 4.6, $\boldsymbol{I}$ is the identity tensor, $\nabla_x \boldsymbol{u}$ is the gradient of the displacement field.

The binary tumor volumes obtained by the Tumor-cut segmentation algorithm are deformably registered, and a sample 2D slice of the resultant 3D displacement field $\boldsymbol{u}$ is visualized on a reference MR slice in Figure 4.4. Inward direction of the vector field on the reference MR image indicates the shrinkage of the tumor.

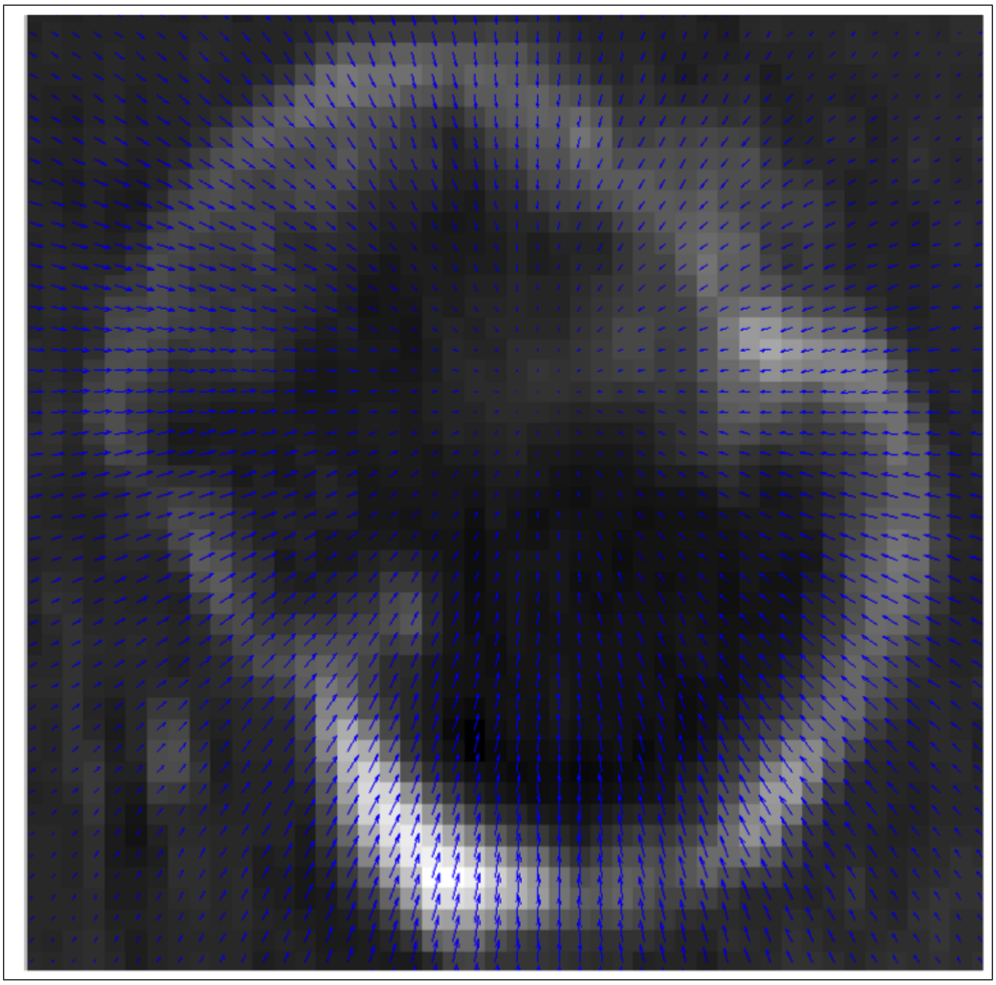

Figure 4.4: Vector field overlayed on a sample reference MR slice.

After obtaining a deformation field between the tumors on the reference and follow-up scans, the estimated 3D vector field can be further interpreted to calculate a local response criteria. As an example, the determinant of the jacobian of the displacement vector field, $det(\nabla_{\boldsymbol{x}} \boldsymbol{u})$, is calculated and visualized as a color map in Figure 4.5.

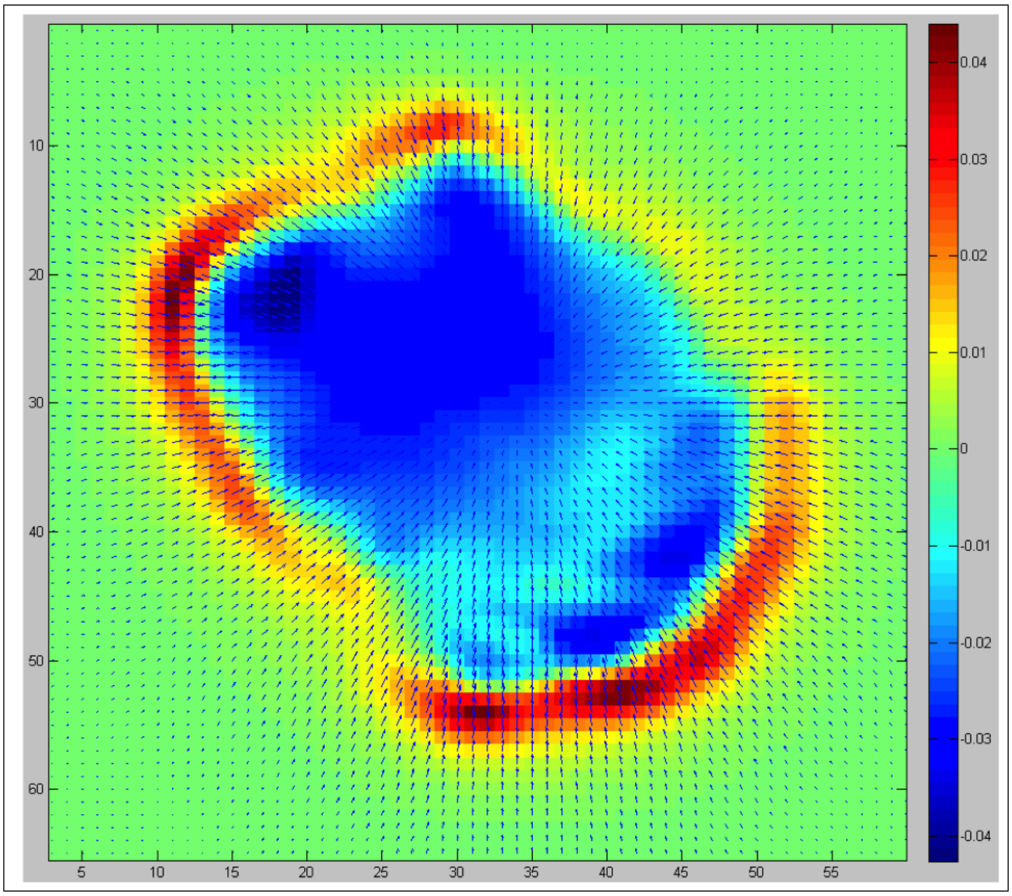

Figure 4.5: Determinant of the jacobian of the 3D vector field visualized as a color map on a sample slice.

By using $\boldsymbol{F}$, the Left Green Deformation Tensor:

$$\boldsymbol{C} = \boldsymbol{F}^T \boldsymbol{F} \tag{4.7}$$

and Lagrange Strain Tensor:

$$\boldsymbol{T} = \frac{1}{2}[\boldsymbol{C} - \boldsymbol{I}] \tag{4.8}$$

can be defined [63]. To calculate a scalar map over a 2nd order tensor, the eigenvalue and eigenvector equation can be used:

$$\boldsymbol{T}\boldsymbol{v} = \lambda\boldsymbol{v} \tag{4.9}$$

where $\boldsymbol{v}$ represents the eigenvector, and λ is the eigenvalue. Three eigenvalues can be determined by solving the characteristic equation:

$$\det(\boldsymbol{T} - \lambda\boldsymbol{I}) = -\lambda^3 + \lambda^2 I_1 - \lambda I_2 + I_3 = 0 \tag{4.10}$$

In the equation above, I_1, I_2, I_3 are defined as the invariants of the tensor $\boldsymbol{T}$ and can be calculated as:

$$\begin{aligned} I_1(\boldsymbol{T}) &= \boldsymbol{T}\cdot\boldsymbol{I} = tr(\boldsymbol{T}) = \boldsymbol{T}_{mm} && (4.11)\\ I_2(\boldsymbol{T}) &= \frac{1}{2}[(\boldsymbol{T}\cdot\boldsymbol{I})^2 - (\boldsymbol{T}\cdot\boldsymbol{T}^T)] = \frac{1}{2}[(\boldsymbol{T}_{mm})^2 - \boldsymbol{T}_{mn}\boldsymbol{T}_{nm}] && (4.12)\\ I_3(\boldsymbol{T}) &= det(\boldsymbol{T}) && (4.13) \end{aligned}$$

where *det* is the determinant of the tensor, *tr* is the trace of the tensor, and the "·" represents the inner product of two tensors.

The first invariant I_1 is a measure of local volume change (< 0 shrinkage and > 0 expansion), the second invariant I_2 is a measure of the strain magnitude, and the third invariant I_3 can be interpreted as again a sort of measure for the local volume change.

In order to quantify the amount of deformation between the tumors on the reference and follow-up scans, the Lagrange Strain tensor $\boldsymbol{T}$ is calculated using equation (4.8), and the tensor invariants I_1, I_2, I_3 are determined by using equations (4.11),(4.12),(4.13).

The evaluation studies of the proposed tensor invariants on synthetic and real MR volumes is described in the next section.

4.4 Evaluation of the Tumor Response Criteria

4.4.1 Evaluation of the Tensor Invariants on the Synthetic Volumes

For further interpretation of the tensor invariants, phantom studies are performed. 3 dimensional deformation fields are estimated, as described in Section 4.2, on spherical and ellipsoidal volumes generated synthetically. Followed by the calculation of the Lagrange Strain tensor, tensor invariant I_1, I_2, I_3 maps are calculated based on this estimated 3D displacement field. The results are given below for various phantoms:

(1) Expansion in a single dimension In order to investigate the effect of the expansion in a single dimension, a spherical volume is mapped to an ellipsoid which is expanded in only one dimension. A sample 2D slice is shown in Figure 4.6, where blue ellipsoid represents the moving volume and white sphere is the static volume. Mathematically, the generated phantoms are as following:

Static volume: $\{(x, y, z) : (x - 350)^2 + (y - 350)^2 + (z - 100)^2 < 50^2\}$

Moving volume: $\{(x, y, z) : 0.5(x - 350)^2 + (y - 350)^2 + (z - 100)^2 < 50^2\}$

Sample 2D slices of each tensor invariant maps are shown in Figure 4.7.

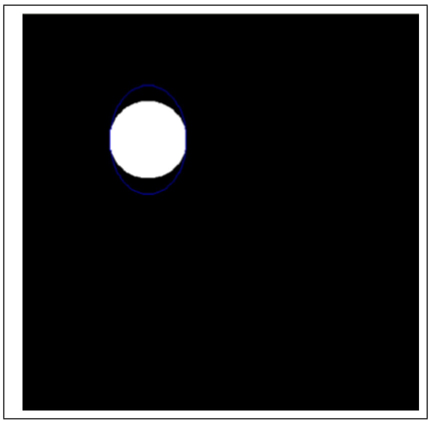

Figure 4.6: Blue contour: Ellipsoidal moving volume. White: Spherical static volume. Displacement vectors are from ellipsoid to sphere.

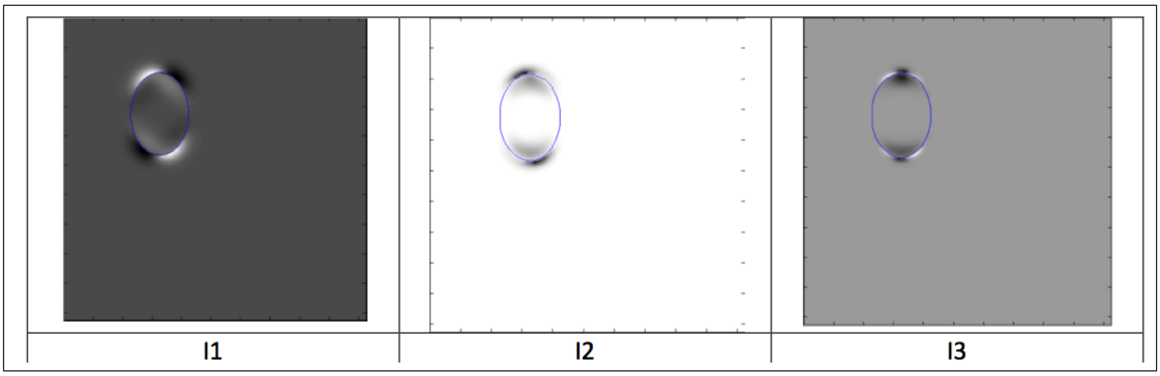

Figure 4.7: A sample slice of the tensor invariant I_1,I_2,I_3 maps between the two volumes in Figure 4.6.

(2) Spherical expansion To investigate the effect of the spherical expansion, two co-centric spheres with different radius are used. A sample 2D slice is shown in Figure 4.8, where the blue sphere is deformed to the white one. Mathematically, the spheres are generated by:

Static volume: $\{(x, y, z) : (x - 350)^2 + (y - 350)^2 + (z - 100)^2 < 80^2\}$

Moving volume: $\{(x, y, z) : (x - 350)^2 + (y - 350)^2 + (z - 100)^2 < 50^2\}$

Sample 2D slices of each tensor invariant maps are shown in Figure 4.9.

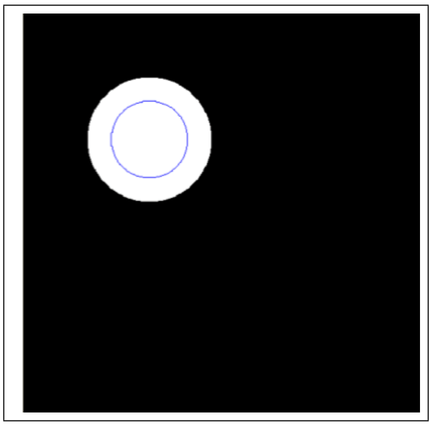

Figure 4.8: Blue contour: Small spherical moving volume. White: Larger spherical static volume. Displacement vectors are from larger to the small sphere.

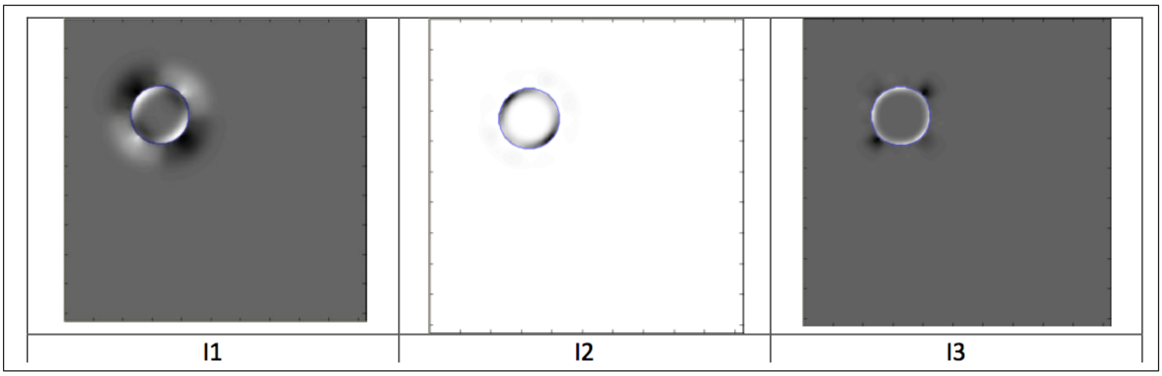

Figure 4.9: A sample slice of the tensor invariant I_1,I_2,I_3 maps between the two volumes in Figure 4.8.

(3) Translation in a single direction To investigate the effect of the translation in a single direction, two spheres at the same size but with translated center points are used. A sample 2D slice is shown in Figure 4.10, where the blue sphere is obtained by translating the white one.

Mathematically, the generated phantoms are as following:

Static volume: $\{(x, y, z) : (x - 350)^2 + (y - 350)^2 + (z - 100)^2 < 50^2\}$

Moving volume: $\{(x,y,z) : (x-320)^2 + (y-350)^2 + (z-100)^2 < 50^2\}$

Sample 2D slices of each tensor invariant maps are shown in Figure 4.11.

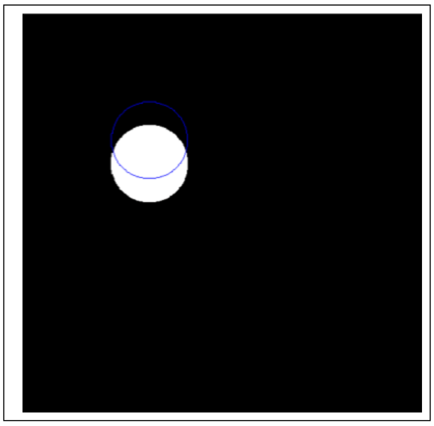

Figure 4.10: Blue contour: Original spherical static volume. White: Moving volume generated by translating the original sphere. Displacement vectors are from white sphere to the blue one.

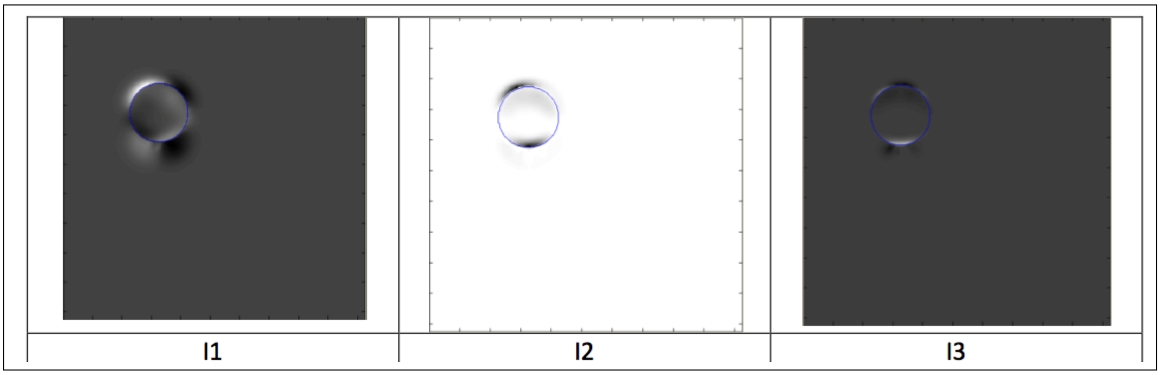

Figure 4.11: A sample slice of the tensor invariant I_1,I_2,I_3 maps between the two volumes in Figure 4.10.

To evaluate the usage of the tensor invariants I_1,I_2,I_3 on quantifying the shape changes, shrinkage in a single direction and translation in a single direction are applied with different amounts and the results are mapped seperately. Using those tensor invariant maps, scalar measures are obtained and listed in Table 4.1. In this table, the first three rows are the volumes of the moving and static phantoms, and the percentage of the volume change. The integrals over the whole displacement domain for the invariants are given in the next three rows, where the last three rows are the coefficient of variations for each invariant given as the ratio of the standart deviation to the average over the domain. Considering the expansion of the sphere to three different ellipsoids, given in the first 3 columns of the table, the integrals and variation of coefficients of the tensor invariants are correlated with the volume changes. At the last 2 columns, instead of changing the volume, translation is applied by different amounts. The coefficient of variations (especially CV I3) shows high variation, which is not observed in volume changes. Evaluation studies done on synthetic phantoms reveal the potential usage of the tensor invariants for assessment of the tumor changes.

Table 4.1: Volumes, integrals of the I_1,I_2,I_3 tensor invariants and coefficient of variations of the I_1,I_2,I_3 tensor invariants calculated for various synthetic phantoms. (Coefficient of variation)[CV = standard deviation/mean].

	From sphere to the highly expanded ellipsoid	From sphere to the medium expanded ellipsoid	From sphere to the lower expanded ellipsoid	From the small sphere to the larger sphere	From the sphere to the 30 voxel translated sphere	From the sphere to the 15 voxel translated sphere
Volume of the moving phantom	9.56×10^5	7.40×10^5	5.85×10^5	2.14×10^6	7.40×10^5	7.40×10^5
Volume of the static phantom	5.23×10^5	5.23×10^5	5.23×10^5	5.23×10^5	7.40×10^5	7.40×10^5
Volume change percentage	82.71%	41.44%	11.76%	309.75%	0.00%	0.00%
Integral I_1	1.62×10^6	3.38×10^5	2.64×10^4	5.90×10^6	9.12×10^5	2.10×10^5
Integral I_2	-2.57×10^6	-2.83×10^5	-2.15×10^4	-5.96×10^6	-8.55×10^5	-1.73×10^5
Integral I_3	-4.78×10^5	-6.19×10^4	-1.36×10^3	-1.77×10^6	-1.88×10^5	-8.05×10^3
CV I_1 (std/mean)	7.39	2.52	1.65	3.94	4.73	2.02
CV I_2 (std/mean)	38.60	0.80	0.05	7.78	23.90	0.31
CV I_3 (std/mean)	4.56	0.49	0.01	1.35	282.00	0.82

4.4.2 Evaluation of the Tensor Invariants on Clinical Cases

Evaluation studies of the tensor invariant measures, which are tested on synthetic phantoms, are performed on radiotherapy patients. The contrast enhanced T1 weighted MR volumes of 16 patients (Glioblastoma Multiforme or Acoustic Neuroma patients) acquired before and after the therapy performed in Anadolu Health Center (ASM) are included. Firstly the MRI volumes acquired after the therapy are aligned with the volumes before the therapy using a rigid transformation (6 degrees of freedom). For both volumes, tumor core and the necrotic regions within the tumor are segmented using the Tumor-cut method described in detail in Chapter 2 and in [43]. The dense displacement field between the two tumor maps is estimated by using the Diffeomorphic Demons algorithm [1]. Corresponding Lagrange Strain tensors and the 3D map of the tensor invariants I_1,I_2,I_3 are calculated for the estimated displacement field. For each patient, calculated change measures are given in Table 4.2. Furthermore, tensor invariants computed on the sample data in Figure 4.12 are given in Figure 4.13 and 4.14.

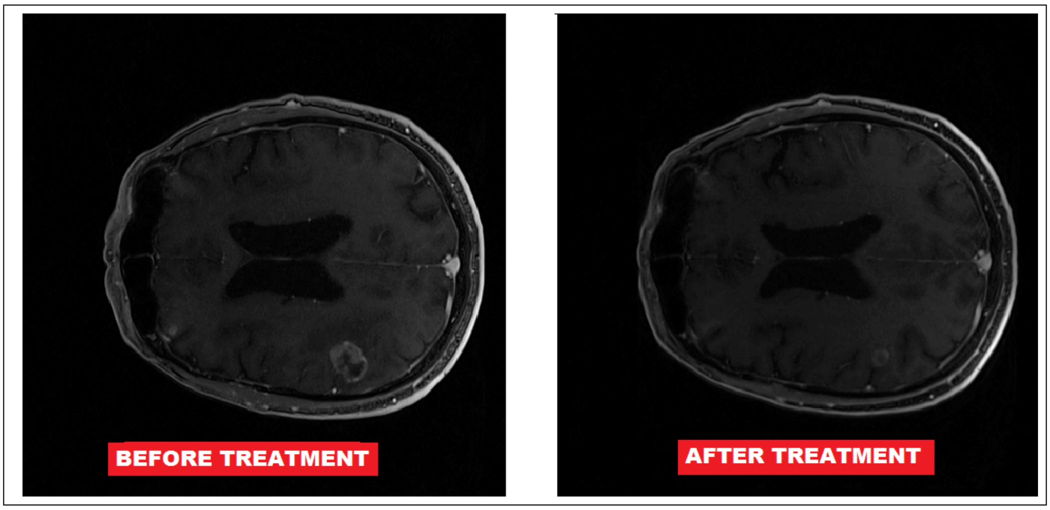

Figure 4.12: Sample MR slices of a patient before (left) and after (right) the treatment.

Table 4.2: Integral of the calculated tensor invariants I_1,I_2,I_3 over the whole domain, coefficient of variations, change of the volumes, displacements of the center of mass and change of the maximum diameters for each clinical case.

ID	Type	Clinical Outcome	Radiological Assessment	Integral I1	Integral I2	Integral I3	Coef.of Var. I1	Coef.of Var. I2	Coef.of Var. I3	Volume Change (%)	Necrotic Volume Change (%)	Displacement (mm)	Maximum Diameter Change (%)
1	Acoustic Neuroma	0	0	260.5	-168.5	4.9	251.3	-58.9	244.1	10.41	0.36	0.37	13.13
2	Acoustic Neuroma	-1	0	280.2	-196.4	6.5	213.9	-85.0	473.3	1.86	-14.31	0.82	-1.88
3	Acoustic Neuroma	0	+1	1026.3	-741.1	28.6	143.9	-26.8	77.4	25.12	245.43	1.00	6.38
4	GBM	-1	+1	195.6	-124.0	-4.5	307.9	-75.8	-559.4	0.01	4.43	0.83	-2.84
5	Acoustic Neuroma	-1	0	9.8	-6.2	0.0	1191.8	-118.1	1352.0	0.91	-22.15	0.14	1.05
6	Acoustic Neuroma	0	0	4330.6	-2730.4	175.4	63.2	-33.8	196.3	111.35	226.26	1.57	28.31
7	GBM	+1	+1	2525.4	-1642.7	42.5	81.7	-27.1	142.0	34.13	7.89	1.29	13.76
8	Acoustic Neuroma	0	0	95.2	-56.5	-1.3	469.1	-91.2	-360.8	-8.73	-19.01	0.42	-1.57
9	Acoustic Neuroma	-1	0	271.7	-157.1	-7.0	290.3	-126.6	-904.4	-8.55	44.22	1.04	-0.42
10	Acoustic Neuroma	-1	0	863.8	-567.3	9.9	138.5	-69.5	1251.2	34.35	52.69	1.27	32.33
11	GBM	+1	+1	3459.8	-2433.8	125.2	73.2	-28.0	150.2	41.11	33.08	2.36	4.41
12	GBM	0	-1	2502.0	-1666.4	-38.3	78.9	-29.0	-261.1	-8.45	-30.11	1.40	10.10
13	Acoustic Neuroma	0	-1	44.3	-22.5	0.5	669.2	-78.4	361.0	27.37	73.43	0.28	7.60
14	Acoustic Neuroma	-1	0	4719.5	-3035.3	-37.7	68.0	-60.2	-1553.9	65.46	341.31	3.84	22.03
15	Acoustic Neuroma	-1	-1	5695.2	-3713.7	-62.6	64.9	-48.2	-1005.7	-8.66	209.68	1.19	-8.12
16	Acoustic Neuroma	-1	-1	210.6	-121.9	1.1	293.1	-60.7	969.1	5.25	-2.56	0.36	0.72

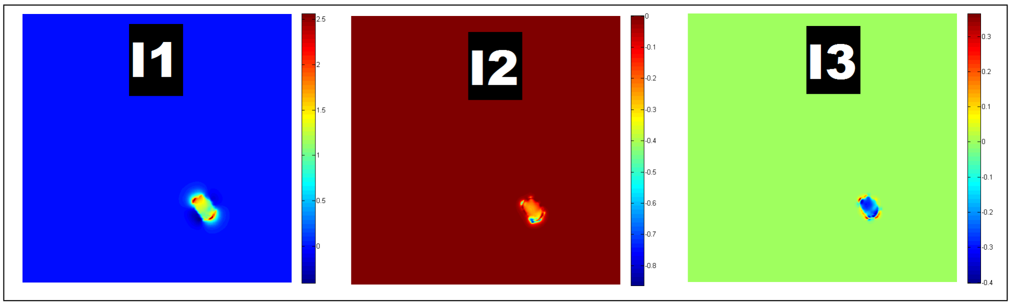

Figure 4.13: Tensor invariants calculated for the patient in Figure 4.12.

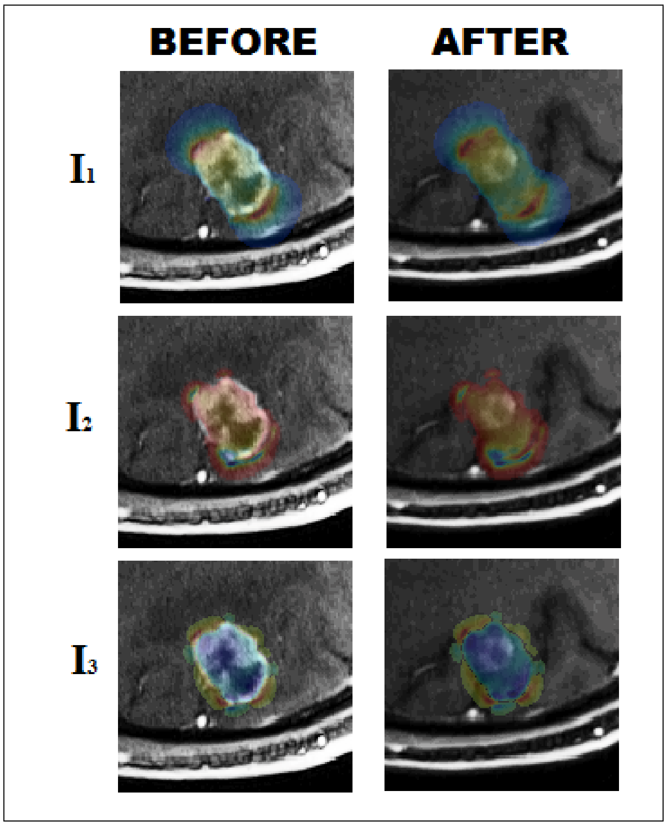

Figure 4.14: Visualization of the calculated tensor invariants on the MR images acquired before (left column) and after (right column) the therapy.

4.5 Clinical Usability Experiments

Contrast enhanced T1 weighted spoiled gradient echo volumes acquired before and after the radiosurgery treatment of 16 patients; 4 with Glioblastoma Multiforme (GBM) and 12 with Acoustic Neuroma were included in the study, retrospectively. In order to evaluate the potential clinical usage of the proposed method, for the cases given in Table 4.2 clinical and radiological assessments reported before and after the treatment are scored by the convention defined in Table 4.3 and tabulated in Table 4.4.

Table 4.3: Scoring convention used to quantify clinical and radiological outcomes.

Convention For Scoring Clinical Outcome	Convention For Scoring Radiological Assesment
-1 : Reduced Symptoms	-1 : Reduction in size
0 : Stability	0 : Unchanged
+1 : Increased Symptoms	+1 : Increased in size

The discriminative value of each of the measures: volume change, maximum diameter change, integrals and coefficient of variations of tensor invariants I_1,I_2,I_3 is determined by Kruskal-Wallis test and the p values are given in Table 4.5. The variance analysis graphs for the most discriminative parameters coefficient of variation of I_2 and integral of I_3 are given in Figure 4.15 and 4.16.

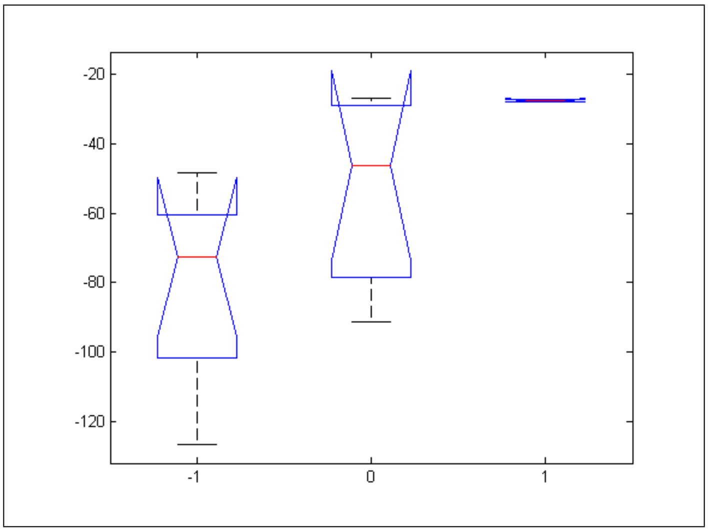

Figure 4.15: Distribution of the coefficient of variation of I_2 for three clinical outcomes (p = 0.05).

Clinical outcomes are visualized on coefficient of variation of I_2 v.s. integral of I_3 plot in Figure 4.17. As seen on the graph, coefficient of variation of I_2 performs better in identifying clinical improvement whereas integral of I_3 is more discriminative in disease progression. Also a possible linear classification is proposed by the red

Table 4.4: Clinical and radiological assessments reported before and after the treatment for the cases given in Table 4.2.

Patient Id	Diagnose	Clinical Outcome	Radiology Volume Change	Radiology Necrotic Volume Change
1	Acoustic neuroma	0	0	+1
2	Acoustic neuroma	-1	0	+1
3	Acoustic neuroma	0	+1	+1
4	GBM	-1	+1	0
5	Acoustic neuroma	-1	0	0
6	Acoustic neuroma	0	0	+1
7	GBM	+1	+1	0
8	Acoustic neuroma	0	0	+1
9	Acoustic neuroma	-1	0	+1
10	Acoustic neuroma	-1	0	+1
11	GBM	+1	+1	0
12	GBM	0	-1	0
13	Acoustic neuroma	0	-1	+1
14	Acoustic neuroma	-1	0	+1
15	Acoustic neuroma	-1	-1	+1
16	Acoustic neuroma	-1	-1	+1

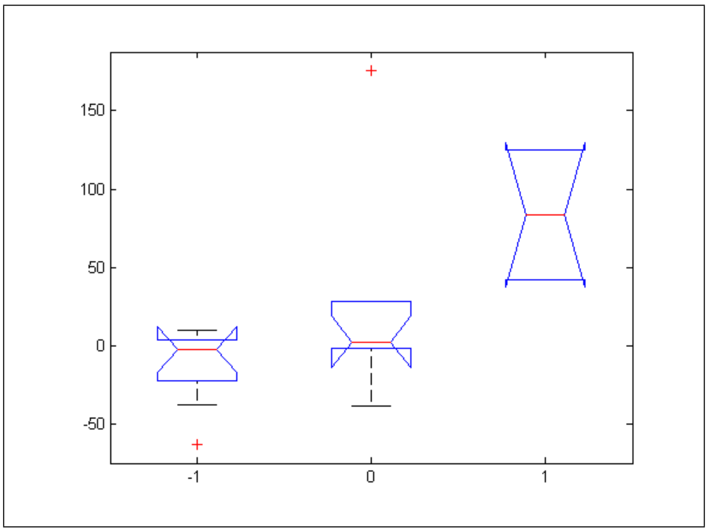

Figure 4.16: Distribution of the integral of I_3 for three clinical outcomes (p = 0.10).

Table 4.5: P values obtained by comparing the clinical outcomes to the calculated measures and radiological assessments by Kruskal-Wallis test.

	Radiological Assessment	Maximum Diameter	Volume	C.V. I_1	C.V. I_2	C.V. I_3	Integral I_1	Integral I_2	Integral I_3
p	0.12	0.34	0.33	0.54	0.05	1.00	0.44	0.54	0.10

and blue lines on the same plot, which provides the results of the proposed method referred in Table 4.18 .

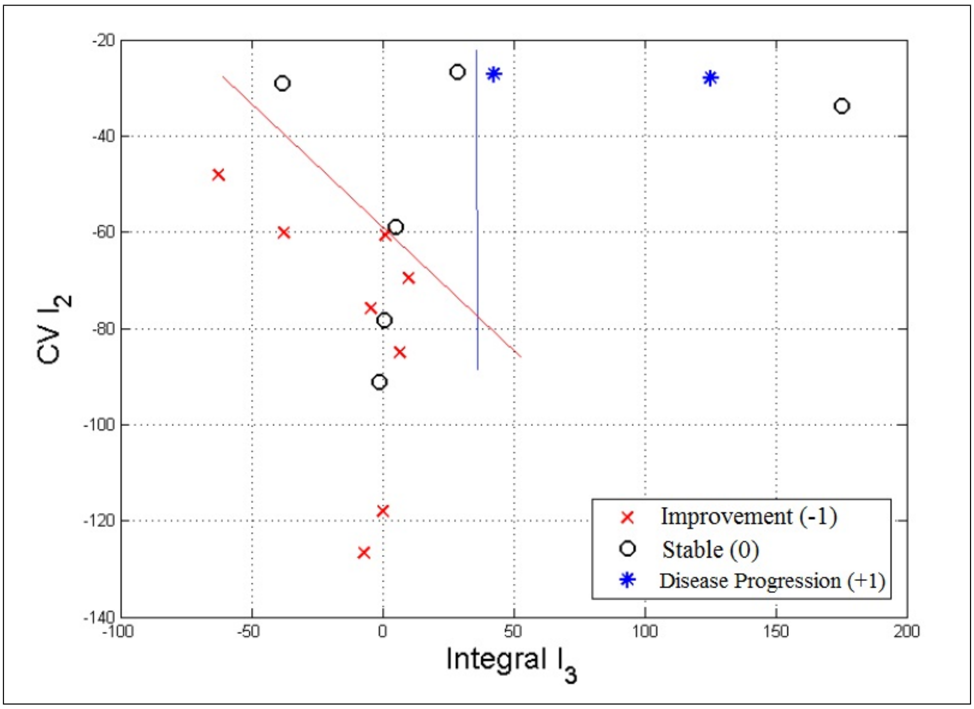

Figure 4.17: Clinical outcomes plotted on coefficient of variation of I_2 v.s. integral of I_3 graph.

Clinical outcomes are compared to the results obtained by the proposed method and the radiological assessment in Table 4.18. In disease progression and stability cases, both the method and the radiological assessment provides similar results, whereas it can be seen that the proposed method performs better in clinical improvement.

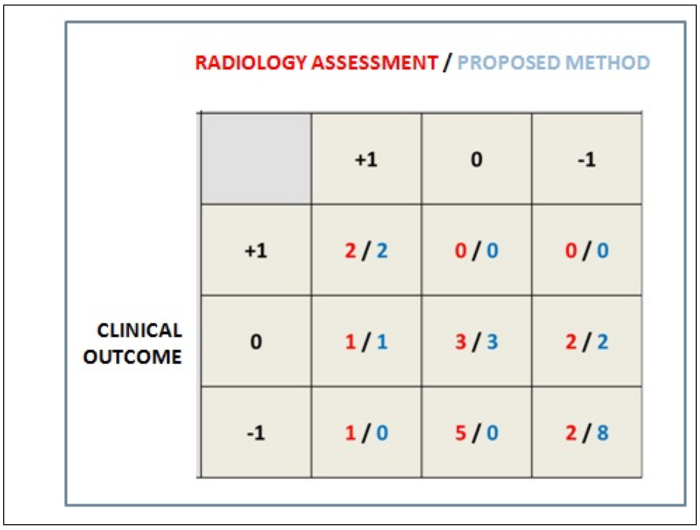

RADIOLOGY ASSESSMENT / PROPOSED METHOD

CLINICAL OUTCOME

	+1	0	-1
+1	2 / 2	0 / 0	0 / 0
0	1 / 1	3 / 3	2 / 2
-1	1 / 0	5 / 0	2 / 8

Figure 4.18: Comparison of the clinical outcomes with the calculated measures and radiological assessments.

4.6 Conclusions

For clinically unchanged and worsened cases, both radiological assessment and the proposed method resulted in the same prediction performance, whereas considering the best linear classifier applicable, the method outperformed the basic global measurements used in the radiological assessment for those cases with clinical improvement.

The volume change, show less importance in explaining the clinical outcome, whereas the variation of the second invariant which is a measure of the strain magnitude and the integral of the third invariant which quantifies the local volume change of the deformation plays a more important role.

The results presented show that the analysis of the deformation fields of tumor changes using methods of solid mechanics might provide results that are more correlated to the clinical outcomes of the therapy than considering only the volume or largest diameter measurements.

The results need further validation on larger datasets and the effect of the regularization while obtaining the deformation field on the results should be considered.

Chapter 5

Registration of Brain Tumor Images using Hyper-elastic Regularization[1]

5.1 Introduction

Registration of pre-therapy and post-therapy brain volumes with tumors is an important task to be able to track the changes between two instances in order to assess the progression of the tumor and the treatment response. The first step is a rigid/affine registration between the two volumes. Although this is a challenging problem due to the changes caused by the tumor, various approaches on the problem reported successful results in the literature [61, 64, 65]. The total deformation caused by the tumor growth can be taught as the combination of infiltration to the healthy tissue and mass effect components. Our aim in this work is to separate the mass effect and infiltration components, so that, malignancy and the reversibility of the destruction can be determined. The healthy brain tissue in one of the images can be warped onto the other ignoring the tumor tissue regions, as the latter may contain uncertainty due to highly complex tumor growth and therapy processes. Hence, the idea proposed in this thesis of matching only the healthy tissues in baseline and follow-up tumor images will provide an estimation of the intracranial pressure caused by the

---

[1] Preliminary part of this work presented in this chapter appeared in the *Computational Biomechanics for Medicine, pp. 101-114, Springer, 2013* and the current version is in preparation for submission as a journal article.

tumor growth plus the mass effect (see Figure 5.1).

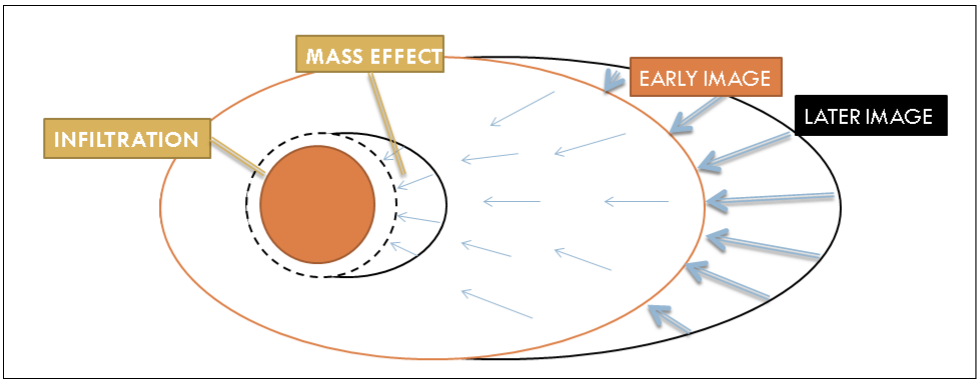

Figure 5.1: Schematic explanation of the idea proposed in the thesis to separate the tumor growth and the mass effect.

A similar problem arises in deformable registration of the brain with tumors to a healthy population atlas. The main difference to the intra-subject registration problem is that the deformation also includes inter-subject variations. Hence, a general strategy to solve this problem is to iterate the forward model by simulating the tumor growth on the atlas and refining the parameters of the simulation model by comparing it to the tumor image [66]. This requires strong models, which rely on realistic models of tumor growth and deformations due to the mass effect [66, 67, 68, 69]. The main problem with those approaches is that the growth of the tumor is mostly affected by the uncontrolled parameters such as treatment and requires sophisticated tumor growth models even without treatment. In "Geometric Metamorphosis" paper, Niethammer et.al, proposed an interesting approach to the problem using a weak model by separating the foreground, hence the tumor growth, and the background changes [70].

For the problem of intra-subject registration, our approach is based on the assumption that the deformations except around the tumor volume are caused by the mass effect of the tumor, hence obey the bio-mechanical rules. This is different from the atlas matching problem, which includes also inter-subject variations between the images. Sample baseline and follow-up MRI slices are shown in Figs. 5.2 and 5.3. Deformation of the ventricles and sulci due to the mass effect of the growing tumor can be clearly observed on the right hemisphere of the subject (denoted by "R" in the figures). Although, a mapping of the tumor tissue between the baseline and

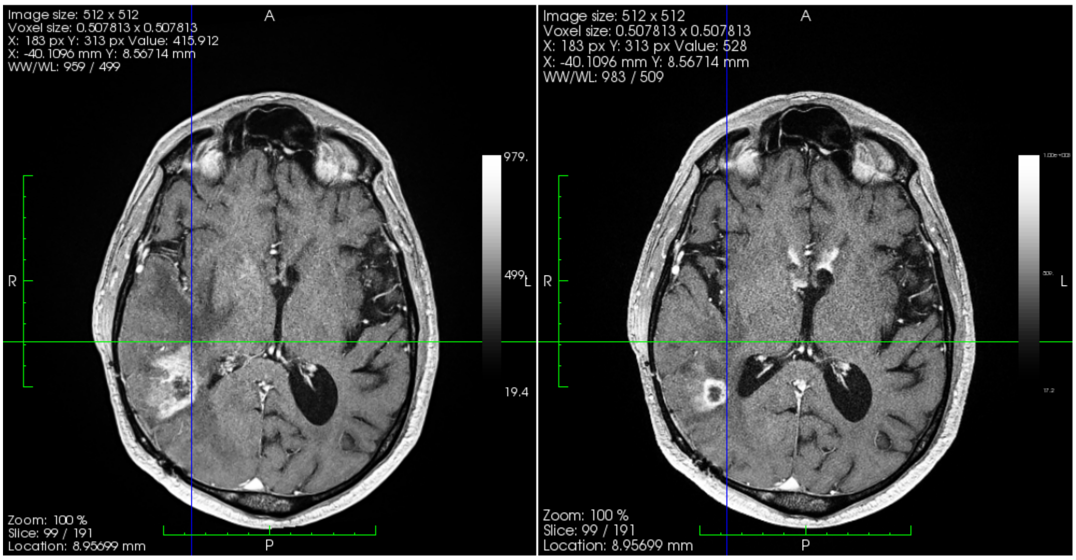

Figure 5.2: A sample axial slice from baseline (on the right) and follow-up (on the left) MRI.

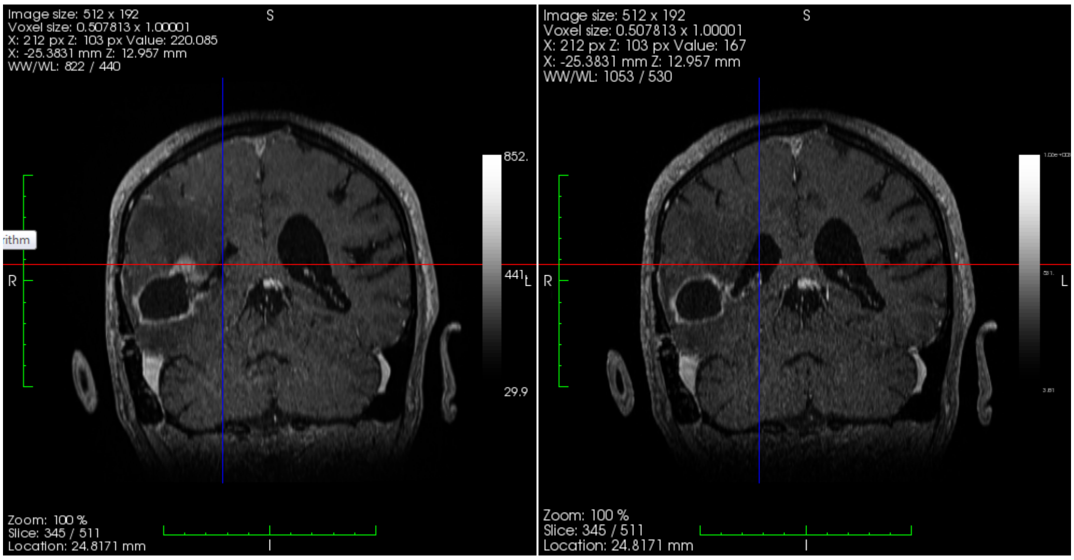

Figure 5.3: A sample sagittal slice from baseline (on the right) and follow-up (on the left) MRI.

the follow-up is not well defined due to the uncertain growth pattern and therapy effects, a mapping between the healthy tissues can be estimated. Therefore, our aim is to find a mapping between the healthy tissues of the brains, which obeys the nonlinear elastic finite deformation models.

The results of the experimental studies on animals suggest to model the brain with a homogeneous hyper-viscoelastic non-isotropic material [71]. In the image analysis literature, simplified hyper-elastic models are used: Neo-Hookean [72], Ogden type [73, 74], Saint-Venant Kirchhoff model [75], linear viscoelastic type [68]. In their work, comparing viscoelastic, hyper-elastic and linear elastic models on brain simulations, Wittek et. al. reports no significant difference on the results obtained [76]. In "Nonlinear Elastic Registration with Unbiased Regularization in Three Dimensions", Saint-Venant Kirchhoff model was used as a regularizer in the registration of serial magnetic resonance images [75].

Our novel contributions in this chapter of the thesis are: (i) Matching healthy tissue to healthy tissue of the brain using a dedicated image data term; (ii) Using the hyper-elastic Neo-Hookean strain energy density as a regularizer in deformable registration framework; (iii) Derivation of displacement field update equations based on the Neo-Hookean model using Euler-Lagrange framework.

5.2 Background

Linear theories of solid mechanics are highly developed and are in a satisfactory state of completion. In the theory of linear elasticity, the stress and strain are related linearly by the Hooke's Law:

$$\sigma = c : \varepsilon \tag{5.1}$$

where σ is the Cauchy stress tensor, ε is the small strain tensor and c is the fourth-order elasticity tensor that contains the material properties. However, this linear model is only valid for infinitesimal or small strains. One of the simplest nonlinear theory to model huge, reversible, shape changes is Hyper-elasticity, which is used to model rubber and foams.

The mechanical properties of a hyper-elastic material are characterized completely by a scalar strain-energy density function W. Specifying the strain energy density W as a function of the deformation gradient $\boldsymbol{F} : W = W(\boldsymbol{F})$ ensures that the material is perfectly elastic. The general form of the strain energy density, W, is guided by experiment [63].

Let us define the displacement field from the un-deformed to deformed configuration as $\boldsymbol{u} : \Omega \longrightarrow \mathbb{R}^3$ where $\Omega \in \mathbb{R}^3$. In addition to the strain energy density

$W = W(\boldsymbol{x}\,, \nabla \boldsymbol{u}\,)$, let $f = f(\boldsymbol{x}\,, \boldsymbol{u}\,(\boldsymbol{x}\,))$ denote the external energy, then the equilibrium configurations can be determined as the minima of the total energy functional:

$$E(\boldsymbol{u}\,) = \int_\Omega W(\boldsymbol{x}\,, \nabla \boldsymbol{u}\,)d\boldsymbol{x} - \int_\Omega f(\boldsymbol{x}\,, \boldsymbol{u}\,)d\boldsymbol{x} \tag{5.2}$$

The Euler-Lagrange system associated with the functional E, which is a necessary condition for a minimizer of the total energy given in Eqn. 5.2, is precisely the equilibrium equation:

$$div(\frac{\partial W}{\partial \boldsymbol{F}}(\boldsymbol{x}\,, \nabla \boldsymbol{u}\,(\boldsymbol{x}\,))) + \frac{\partial f}{\partial \boldsymbol{u}}(\boldsymbol{x}\,, \boldsymbol{u}\,(\boldsymbol{x}\,)) = 0 \tag{5.3}$$

where $F_{ij} = \sigma_{ij} + \frac{\partial u_i}{\partial x_j}$ is the deformation gradient and $\frac{\partial W}{\partial \boldsymbol{F}}^T$ is called the First Piola-Kirchhoff tensor in the mechanics literature [77].

Commonly, constitutive hyper-elastic strain energy density models are based on principal strains λ_i, or invariants of the stretch tensor I_i, defined as:

$$\begin{aligned} I_1 &= \lambda_1^2 + \lambda_2^2 + \lambda_3^2 \\ I_2 &= \lambda_1^2\lambda_2^2 + \lambda_2^2\lambda_3^2 + \lambda_1^2\lambda_3^2 \\ I_3 &= \lambda_1^2\lambda_2^2\lambda_3^2 \end{aligned} \tag{5.4}$$

With the incompressibility assumption for the material, I_3 is taken to be constant and equal to 1.0 and does not contribute to the strain energy. One of the most simple models is the Neo-Hookean model, which is given as:

$$W_{NH} = C(I_1 - 3) \tag{5.5}$$

Another model that has been extensively utilized in studies of elastomer deformation is the Mooney-Rivlin model, given as:

$$W_{MR} = C_1(I_1 - 3) + C_2(I_2 - 3) \tag{5.6}$$

A more general form in terms of principal stretches is the Ogden model, given as:

$$W_O = \sum_n \frac{\mu_n}{\alpha_n}(\lambda_1^{\alpha_n} + \lambda_2^{\alpha_n} + \lambda_3^{\alpha_n} - 3) \tag{5.7}$$

where n is the degree of the model and μ_n and α_n are the model parameters.

Note that the Neo-Hookean model results from Eqn. 5.7 by setting $n = 1$ and $\alpha_1 = 2$, whereas Mooney-Rivlin model can be obtained by setting $n = 2$, $\alpha_1 = 2$, $\alpha_2 = -2$.

Although rubber elastic materials are generally considered to be incompressible, including compressibility increases accuracy, improves models where the bulk response is important and helps to avoid numerical problems inherent in incompressibility assumption. Compressible forms of the strain energy function W are developed in one of two ways. Both begin by removing the incompressibility restriction that $J = 1$ where $J = \sqrt{I_3}$. Decoupling approach assumes the strain energy is a separable function of a deviatoric strain (distortional) energy and a hydrostatic strain (volumetric) energy dealing with the volume change, as follows:

$$W = W_D(\bar{I}_1, \bar{I}_2) + W_H(J) \tag{5.8}$$

where $\bar{I}_1$ and $\bar{I}_2$ are invariants of the deviatoric stretch tensor, $\bar{I}_1 = J^{-2/3}I_1$, $\bar{I}_2 = J^{-4/3}I_2$. Corresponding decoupled representations for hyper-elastic models can be reformulated by replacing λ_i and I_i by the modified quantities $\bar{\lambda}_i$ and $\bar{I}_i$, and adding a suitable volumetric response function. For example, the decoupled strain-energy function for the Mooney-Rivlin model has the form:

$$W_{MR}(\bar{I}_1, \bar{I}_2, J) = C_1(\bar{I}_1 - 3) + C_2(\bar{I}_2 - 3) + W_{VOL}(J) \tag{5.9}$$

where W_{VOL} can be selected as a penalty of the deviation of J from unity. Other compressible formulations append a bulk strain energy term to an existing strain energy form, as follows:

$$W = W_a(I_1, I_2, J) + W_b(J) \tag{5.10}$$

Here, both W_a and W_b terms contain contributions due to the volume change. As an example, the coupled form of the compressible Mooney-Rivlin model may be given as:

$$W_{MR}(I_1, I_2, J) = C_1(I_1 - 3) + C_2(I_2 - 3) - dlnJ + c(J - 1)^2 \tag{5.11}$$

where c is a material constant and d defines a parameter with certain restrictions. Another example is the coupled form of the compressible neo-Hookean model given by:

$$W_{NH}(I_1, J) = \frac{c_1}{\beta}(J^{-2\beta} - 1) + c_1(I_1 - 3) \tag{5.12}$$

with the constants $c_1 = \mu/2$ and $\beta = \nu/(1-2\nu)$. The material parameters μ and ν denote the shear modulus and Poisson's ratio, respectively [78, 79].

5.3 Methods

In deformable registration, the problem is to find the displacement field $\boldsymbol{u}$ from the volume R to T, which minimizes the given functional:

$$\boldsymbol{u}^* = \arg\min_{u} \int_{\Omega} f(R(\boldsymbol{x}), T(\boldsymbol{x} + \boldsymbol{u}(\boldsymbol{x}))) + \alpha W(\boldsymbol{x}, \nabla \boldsymbol{u}) d\boldsymbol{x} \tag{5.13}$$

where f is the external energy density term calculated as a similarity measure between the reference (R) and target (T) volumes and α is the weighting parameter of the regularizer term W. Let $R(\boldsymbol{x})$ and $T(\boldsymbol{x})$ denote the brain tissue maps (White Matter + Gray Matter + Tumor) of reference (undeformed) and target (deformed) volumes, respectively. The mechanical properties of white matter and gray matter are assumed to be similar.

In this section, first, the energy forms for both image and regularizer terms that are used in this study are introduced and corresponding Euler-Lagrange conditions are derived. Then, details of the implementation of deformable registration is given.

5.3.1 Image Term for Matching the Boundaries of the Bodies

A solution that matches the outside surfaces of the two bodies requires all the displacements from the surface of the reference body (fixed body) to point the surface of the target body (moving body). Therefore, an energy term, which penalizes the distance from the surface of the reference body to the surface of the target can be used for this purpose. Note that, displacement vectors can still move on the target surface freely. This is ensured by the following energy term:

$$f_B(\boldsymbol{x}, \boldsymbol{u}(\boldsymbol{x})) = \chi_{\partial R}(\boldsymbol{x}) D_{\partial T}(\boldsymbol{x} + \boldsymbol{u}(\boldsymbol{x})) \tag{5.14}$$

where $\chi_{\partial R}$ is the indicator function of the boundary of the reference body, having the value of 1 for the points on the boundary and 0 elsewhere. $D_{\partial T}$ is the distance to the boundary of the target body. By defining the distance function from a point $\boldsymbol{x}$ to a set $S \in \Omega$ as:

$$d(\boldsymbol{x}, S) = \inf\{\|\boldsymbol{x} - \boldsymbol{y}\|_2 : \boldsymbol{y} \in S\} \tag{5.15}$$

and the signed distance function as:

$$\phi_S(\boldsymbol{x}) = \begin{cases} d(\boldsymbol{x}, S) & \text{if } \boldsymbol{x} \in S^C \\ -d(\boldsymbol{x}, S^C) & \text{if } \boldsymbol{x} \in S \end{cases} \tag{5.16}$$

The integrand of the total external energy functional can be written as:

$$f_B(\boldsymbol{x}, \boldsymbol{u}(\boldsymbol{x})) = \delta_0(\phi_R(\boldsymbol{x})) \cdot \phi_T(\boldsymbol{x} + \boldsymbol{u}(\boldsymbol{x}))^2 \tag{5.17}$$

Here, squared distance is used to assure the continuity of the derivative at the boundary while equally penalizing negative and positive distances. To derive the Euler-Lagrange condition for this energy term, the derivative of the functional in Eq. 5.17 is written as:

$$\frac{\partial}{\partial u} f_B(\boldsymbol{x}, \boldsymbol{u}(\boldsymbol{x})) = \delta_0(\phi_R(\boldsymbol{x})) \cdot 2\phi_T(\boldsymbol{x} + \boldsymbol{u}(\boldsymbol{x}))\nabla_{x+u(x)}\phi_T(\boldsymbol{x} + \boldsymbol{u}(\boldsymbol{x})). \tag{5.18}$$

5.3.2 Hyper-elastic Regularizer

For simplicity, assuming a nonlinear hyper-elastic model in a decoupled Ogden form as in [74]:

$$W = \frac{2\mu}{\alpha^2}(\bar{\lambda_1}^{\alpha} + \bar{\lambda_2}^{\alpha} + \bar{\lambda_3}^{\alpha} - 3) + \frac{1}{D_1}(J-1)^2 \tag{5.19}$$

where principal strains $\bar{\lambda_i} = \lambda_i / J^{1/3}$, $\lambda_i = e_i^{1/2}$, e_i's are eigenvalues of $\boldsymbol{B} = \boldsymbol{F}\boldsymbol{F}^T$, J is the determinant of the deformation $J = det(\boldsymbol{F})$ and deformation gradient tensor $F_{ij} = \frac{\partial u_i}{\partial x_j} + \delta_{ij}$. In [71], α parameter of the model for the brain tissue is determined as $\alpha = -4.7$. For simplicity, in this work $\alpha = 2$ is used, which is known as the Neo-Hookean model. By replacing $Tr(B) = \lambda_1^2 + \lambda_2^2 + \lambda_3^2$, the strain energy density function becomes:

$$W = \frac{\mu}{2}(\frac{Tr(B)}{J^{2/3}} - 3) + \frac{1}{D_1}(J-1)^2 \tag{5.20}$$

The Euler-Lagrange condition on the displacement field $\boldsymbol{u}$ for minimizing the given strain energy functional in terms of the trace and determinant is given by:

$$\frac{\partial W}{\partial u_i} - \sum_j \frac{\partial}{\partial x_j}\frac{\partial W}{\partial(\partial u_i/\partial x_j)} = 0 \tag{5.21}$$

The first term drops, as the energy density functional W is not dependent on the $\boldsymbol{u}$ but its derivatives. The derivative with respect to $\partial u_i/\partial x_j$ is identical to the derivative with respect to F_{ij}, therefore, rewriting Eq. 5.21 results in:

$$\sum_j \frac{\partial}{\partial x_j}\frac{\partial W}{\partial F_{ij}} = 0 \tag{5.22}$$

The derivative $\frac{\partial W}{\partial F_{ij}}$, which is also known as the 1st Piola-Kirchhoff tensor in mechanics literature, is obtained after a set of manipulations as follows (see Appendix B):

$$\begin{aligned} -\frac{\mu}{J^{2/3}}\sum_j(\frac{\partial \boldsymbol{F}}{\partial x_j})_{ij} + \frac{2\mu}{3J^{2/3}}\sum_j F_{ij}Tr(\boldsymbol{F}^{-1}\frac{\partial \boldsymbol{F}}{\partial x_j}) \\ -(\frac{\mu Tr(\boldsymbol{B})}{3J^{2/3}} - \frac{2J(J-1)}{D1})\sum_j(\boldsymbol{F}^{-1}\frac{\partial \boldsymbol{F}}{\partial x_j}\boldsymbol{F}^{-1})_{ji} \\ -(\frac{2\mu Tr(\boldsymbol{B})}{9J^{2/3}} + \frac{2J(2J-1)}{D1})\sum_j(\boldsymbol{F}^{-1})_{ji}Tr(\boldsymbol{F}^{-1}\frac{\partial \boldsymbol{F}}{\partial x_j}) \\ +\frac{2\mu}{3J^{2/3}}\sum_j(\boldsymbol{F}^{-1})_{ji}Tr(\frac{\partial \boldsymbol{F}}{\partial x_j}\boldsymbol{F}^T) = 0 \end{aligned} \tag{5.23}$$

In some cases, for the volumetric part of the strain energy, instead of $(J-1)^2$ above, the following form is used:

$$W_{vol} = \frac{K}{2}(lnJ)^2 \tag{5.24}$$

Similarly, the derivatives $\frac{\partial W}{\partial F_{ij}}$, for this term can be derived (see Appendix C):

$$\begin{aligned} -\sum_j \frac{\partial}{\partial x_j}\frac{\partial W}{\partial F_{ij}} = -K\sum_j(\boldsymbol{F}^{-1})_{ji}Tr[\boldsymbol{F}^{-1}\frac{\partial \boldsymbol{F}}{\partial x_j}] \\ -KlnJ\sum_j(\boldsymbol{F}^{-1}\frac{\partial \boldsymbol{F}}{\partial x_j}\boldsymbol{F}^{-1})_{ji} \end{aligned} \tag{5.25}$$

5.3.3 Log-Barrier Method

At each iteration, inverse of the deformation $\boldsymbol{F}$ is computed, which requires the determinant of the deformation to be non-zero. Furthermore, to avoid foldings at the final result, the determinant of the deformation is needed to be positive at each point. To assure both, an inequality constraint $J > 0$ can be imposed by using the log-barrier method, which contributes to the energy functional as:

$$W = -\lambda lnJ \tag{5.26}$$

where J is the determinant of the deformation $\boldsymbol{F}$. For J is a function of $\boldsymbol{F}$, similar to the incompressibility term of the hyperelastic regularizer, the corresponding term of the Euler-Lagrange condition can be calculated as (see Appendix D):

$$-\sum_j \frac{\partial}{\partial x_j}\frac{\partial W}{\partial F_{ij}} = \lambda \sum_j (\boldsymbol{F}^{-1}\frac{\partial \boldsymbol{F}}{\partial x_j}\boldsymbol{F}^{-1})_{ji}$$

5.3.4 Implementation Details

In the implementation, the $\delta(\cdot)$ function is approximated as the derivative of a regularized Heaviside function as in [26] as:

$$\begin{aligned} H(z) &= \frac{1}{2}(1 + \frac{2}{\pi}arctan(\frac{z}{\varepsilon})) \\ \delta_0(z) &= \frac{\partial}{\partial z}H(z) = \frac{1}{\pi\varepsilon}\frac{1}{1+(\frac{z}{\varepsilon})^2} \end{aligned} \tag{5.27}$$

Although the squared distance given in Equation 5.17 is useful to avoid oscillations around the boundary due to the zero value near the boundary, at large distances, the derivative is increasing with the distance, which causes uncontrolled update steps and instabilities. To overcome those problems, the Huber function is employed in the image term, which is given in [80] as:

$$\rho_k(z) = \begin{cases} \frac{z^2}{2} & \text{if } |z| <= k \\ k|z| - \frac{k^2}{2} & otherwise \end{cases} \tag{5.28}$$

That is this function incorporates the absolute value for farther distances, determined by a threshold “k”. A multi-resolution approach is implemented to increase the convergence speed. Volumes are down-sampled using trilinear interpolation and the obtained displacement field is interpolated to the higher resolution at the end of each stage.

The update equation for the displacement field $\boldsymbol{u}$ is obtained by the steepest descent method as:

$$\frac{\partial \boldsymbol{u}}{\partial t} = -(Eq.5.18 + Eq.5.23) \tag{5.29}$$

If the maximum change due to the regularizer is greater than 1, the update of the displacement $\nabla_u W$, is normalized by dividing to the maximum update over the image grid:

$$\nabla_u W = \begin{cases} \frac{\nabla_u W}{max(\nabla_u W)} & \text{if } \nabla_u W > 1 \\ \nabla_u W & otherwise \end{cases} \tag{5.30}$$

Scaling of the strain energy density function of the regularizer term is arbitrary. Therefore, instead of having two independent parameters μ and D_1 for the energy functional in Eq. 5.20, the algorithm is affected mainly by the ratio $\frac{\mu}{1/D_1} = \mu D_1$.

The effect of a μD_1 at a higher limit is shown on the sub-figure at the center of Fig. 5.5, which corresponds to the first term in Eq. 5.20, whereas, the effect of a zero μD_1 is shown on the right sub-figure of Fig. 5.5, which corresponds to the second term. In this work, our aim is to estimate the cause (tumor deformation) by observing the result (displacement at the boundaries). Therefore, we assure the reversibility by enforcing a highly incompressible behavior to prevent the energy to be stored in the material, which we can not observe by MRI. This is achieved by penalizing the local volume changes more by setting a low μD_1. We also assume that the total volume increase of the brain parenchyma is mostly caused by the increase of the tumor volume. Therefore, by setting the tumor region as a hole for the regularizer, which does not contribute to the external energy, and using an incompressible strain energy density, the observed local volume changes at the boundaries of the parenchyma are carried to the tumor area. We also note that, by decreasing the μ, the dependence of the strain energy density to the model parameter α in Eq. 5.19 is decreased, which strengthen our simplification approach of using Neo-Hookean model ($\alpha = 2$) instead of Ogden form with $\alpha = -4.7$.

Starting with an initial time step δt for the regularizer, the value is halved if the strain energy is not decreased by updating the displacement field.

The first derivatives are calculated by using central difference finite differencing scheme as:

$$V_x(x, y, z) = \frac{V(x+h, y, z) - V(x-h, y, z)}{2h} \tag{5.31}$$

The derivative $\frac{\partial \boldsymbol{F}}{\partial x_j}$ is given by the following matrix:

$$\frac{\partial \boldsymbol{F}}{\partial x_j} = \begin{pmatrix} \frac{\partial^2 u_1}{\partial x_1 \partial x_j} & \frac{\partial^2 u_1}{\partial x_2 \partial x_j} & \frac{\partial^2 u_1}{\partial x_3 \partial x_j} \\ \frac{\partial^2 u_2}{\partial x_1 \partial x_j} & \frac{\partial^2 u_2}{\partial x_2 \partial x_j} & \frac{\partial^2 u_2}{\partial x_3 \partial x_j} \\ \frac{\partial^2 u_3}{\partial x_1 \partial x_j} & \frac{\partial^2 u_3}{\partial x_2 \partial x_j} & \frac{\partial^2 u_3}{\partial x_3 \partial x_j} \end{pmatrix}$$

Its components are calculated by second order finite difference discretization as:

$$\begin{aligned} V_{xx}(x,y,z) &= \frac{V(x-h,y,z) - 2V(x,y,z) + V(x+h,y,z)}{h^2} \\ V_{xy}(x,y,z) &= \frac{V(x+h,y+h,z) - V(x+h,y-h,z) - V(x-h,y+h,z) + V(x-h,y-h,z)}{4h^2} \end{aligned} \tag{5.32}$$

Other derivative components are calculated similarly.

At the boundaries Neumann boundary conditions, which sets a zero normal derivative at the boundary, are used. To impose Neumann condition, the first derivative is set to zero if any of the $V(x+h,y,z)$ or $V(x-h,y,z)$ in Eqn. 5.31 is missing (out of the volume). Note that, this also satisfies the normality to the boundary. Let's assume the value at the positive x direction is out of the volume. By setting:

$$V_x(x,y,z) = \frac{V(x+h,y,z) - V(x-h,y,z)}{2h} = 0 \tag{5.33}$$

The missing value that satisfies zero normal boundary can be estimated by replicating the value inside to the outside as:

$$V(x+h,y,z) = V(x-h,y,z) \tag{5.34}$$

By this substitution, the second derivative at the boundary can be written as below:

$$V_{xx}(x,y,z) = 2\frac{V(x-h,y,z) - V(x,y,z)}{h^2} \tag{5.35}$$

Using a similar approach of substituting the missing terms is applied for calculating the derivatives in other directions (i.e. $V_y(x,y,z)$, $V_z(x,y,z)$) and the cross terms of the second derivatives (i.e.$V_{xy}(x,y,z)$), at the boundaries.

5.4 Experiments and Results

5.4.1 Regularizer Test

To test the regularizer initially, the algorithm is run on 10x10x10 mask on a 20x20x20 lattice with a single constant displacement vector (0.0001,0.0001,0.0) and zero boundary conditions. The central xy-plane of the input and the result obtained with $\mu = 0.8$ and $D_1 = 1.0$ is given in Fig. 5.4 with a closer look at Fig. 5.5. The effect of setting the parameters of the model at the lower and higher limits is shown on the middle and the right sub-figures of Fig. 5.5. Although, incompressibility is a necessity for our problem as discussed in the method, setting a non-zero value to μ helps to increase the stability of the solution.

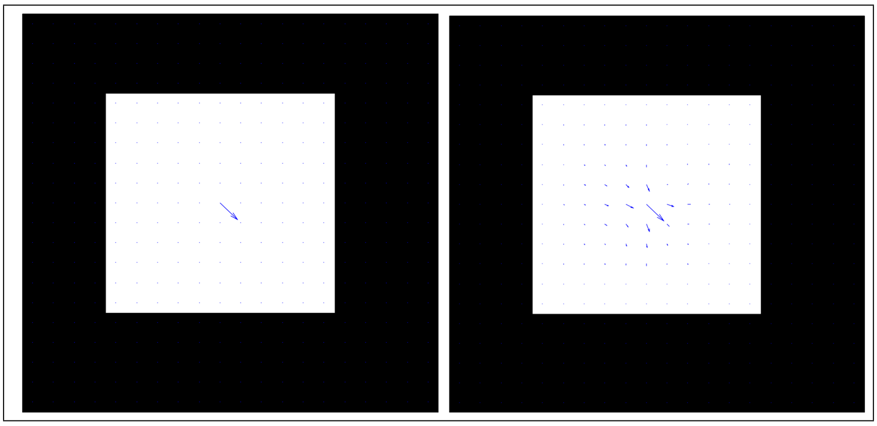

Figure 5.4: Left: Input phantom for the regularizer test. Right: Output of the regularizer test.

5.4.2 Experiments on FEBIO Simulations

In order to validate the proposed methodology of estimating the displacement field inside the object, given the initial and final contours, simulation studies are performed. FEBIO software, which is a nonlinear implicit finite element (FE) software, is used for simulation studies [81]. A constant force is applied to a cubic solid object. We used Mooney-Rivlin model, given below, with $c_2 = 0$ to obtain an uncoupled Neo-Hookean model.

$$W(\lambda_1, \lambda_2, \lambda_3, J) = c_1(\bar{I}_1 - 3) + c_2(\bar{I}_2 - 3) + \frac{K}{2}(lnJ)^2 \tag{5.36}$$

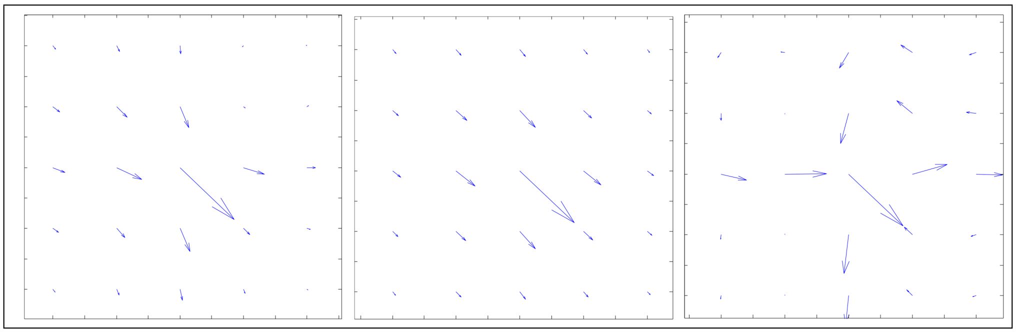

Figure 5.5: Left: A closer view of the output of the regularizer test on phantom in Figure 5.4. Middle: The result obtained on phantom by increasing μ in the strain energy density model in Eq. 5.20. Right: The result obtained on phantom by setting the μ as zero in the strain energy density model in Eq. 5.20.

Other material parameters are assigned as; $c_1 = 0.1$ and $K = 1.0$. The same model is implemented and the displacement field is estimated by the method proposed in this chapter using the known initial and final states of the object. Simulated and estimated displacement fields are shown in Figure 5.6.

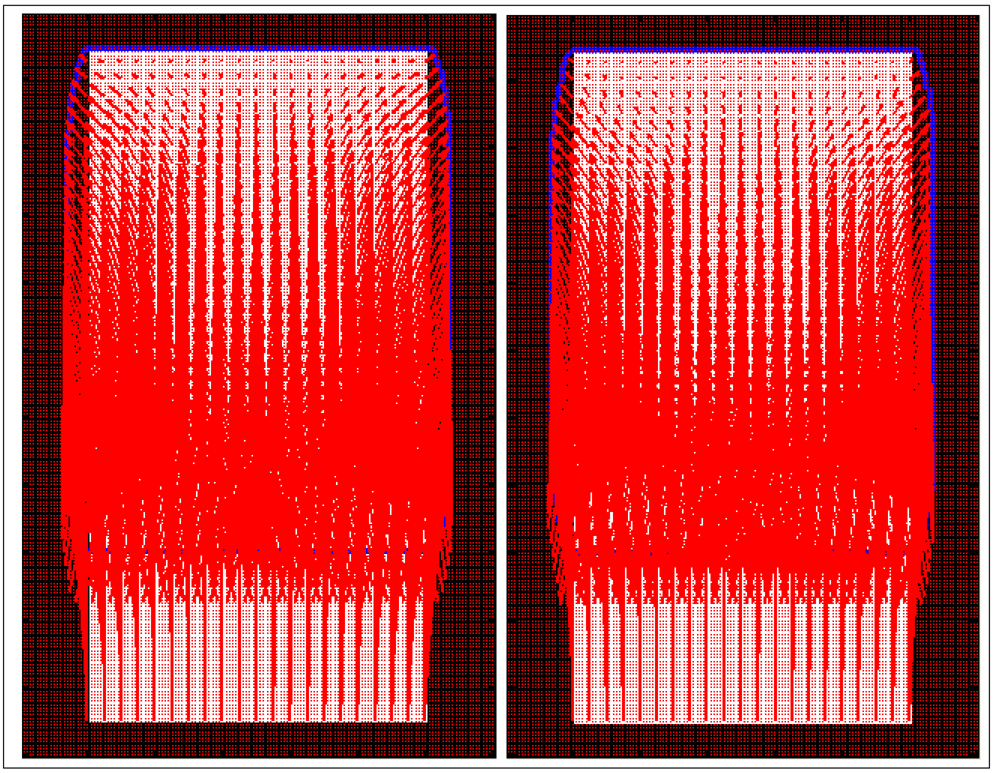

Figure 5.6: The finite element simulation result obtained for the neo-hookean box, on the left. Estimated displacement field for the same scenario by our method, on the right.

5.4.3 Experiments on MRI Brain Tumor Followup Volumes

The Data

MR images of a brain tumor patient (Glioblastoma Multiforme), obtained by 1.5T MRI scanner at high resolution ($\approx$ 0.5x0.5x1.0 mm) contiguous axial T1 weighted 3D SPGR (TE/TR = 3.16s/8.17s, FA=25deg) sequence acquired after IV injection of 10cc 0.5M Multihance Gd, is used for validation study. The sample slices of the baseline and the follow-up volume, obtained 35 days after, are given in Fig. 5.2 and 5.3.

Preprocessing MRI Volumes

Statistical Parametric Mapping (SPM8) software [2], distributed by Wellcome Trust Centre for Neuroimaging, London, which gives accurate results in brain volumes with tumors, is used for standard operations such as: rigid registration, brain tissue segmentation and smoothing. Specifically, the following preprocessing operations are applied to the data before the execution of the deformable registration:

- Follow-up volume is rigidly registered to the baseline volume using "co-register" function of SPM8.
- White matter (WM) and gray matter (GM) segmentations ($P > 0.5$) are obtained for both volumes using SPM8.
- Tumors in both volumes are segmented using the Tumor-cut algorithm [53].
- For each of the volumes, Tumor, WM and GM segmentations are combined using: $\Omega_{Tumor} \cup \Omega_{WM} \cup \Omega_{GM}$.
- Each combined binary volume is smoothed by the "smooth" function of the SPM8 with a Gaussian kernel having 8x8x8mm full width at half maximum.
- Finally, binary maps are converted to isotropic voxels ($1 \times 1 \times 1mm$).

---

[2] http://www.fil.ion.ucl.ac.uk/spm/

Results

After executing the proposed deformable registration algorithm proposed in this thesis on the MRI data of the patient, sample slices showing the resulting displacement field, obtained on tumor patient data, are shown in Fig. 5.7. Intense displacement on the hemisphere with tumor, due to the mass effect, can be observed. At the bottom of the sub-figure on the right, displacement of the sulci due to the increased cerebrospinal fluid (CSF) pressure can be seen. Also, the increase in the CSF pressure results in slight displacements at the ventricles of the healthy hemisphere, on the top. Displacement field, overlayed on a sample axial slice of the reference MRI in high resolution, is given in Fig. 5.8. The mass effect around the tumor is clearly observed. A closer look to the ventricle at the hemisphere without tumor depicts the displacement due to the expansion of the ventricle. When we focus on the displacement around the tumor as in Fig. 5.9, the displacement caused by the mass-effect (at the top) and the tumor growth (on the right) can be observed. The vectors at the the bottom-left of the tumor explains the local shrinkage of the tumor as a tissue displacement.

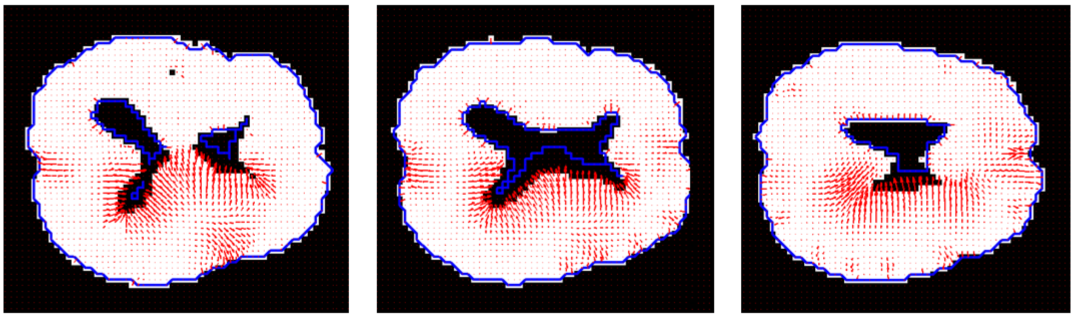

Figure 5.7: Sample slices of the result obtained on tumor patient data in 3x3x3mm voxel size. Binarized brain tissue of the reference volume is labeled in white color, the blue contour indicates the boundary of the target volume, and the displacement field is indicated with arrows in red.

5.5 Discussion and Conclusions

A method to register the brain tissues in baseline and follow-up MRI volumes using hyper-elastic deformation models is presented. Implementations on synthetic and

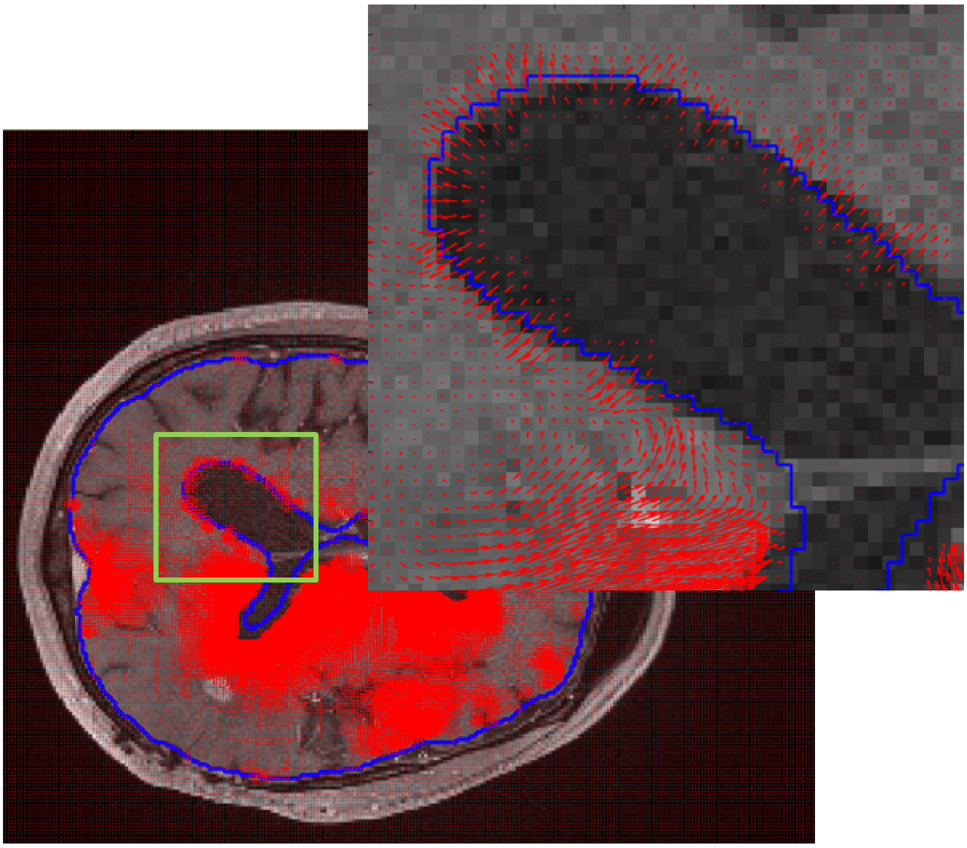

Figure 5.8: Displacement field (in red) overlayed on a sample MRI slice of the reference volume, with the boundary of the target volume indicated with the blue contour. A closer look to the ventricle of the hemisphere without tumor.

patient data, with only minimal user interaction, provide promising results, which might have relevant use in clinical problems. Publicly available state-of-the-art algorithms for the rigid registration and tissue/tumor segmentation are able to provide highly accurate outputs, which are necessary initializations in order to obtain an accurate displacement field. Accuracy of the method could be increased by improving the data term, such as by adding vessel correspondences or manual landmarks. Furthermore, although in this thesis, we utilized a measure based on distances between pre- and post- tumor surfaces as the data (image) term, a direct utilization of image intensity-based measures such as SSD, would be a straightforward extension on the data term part of our method.

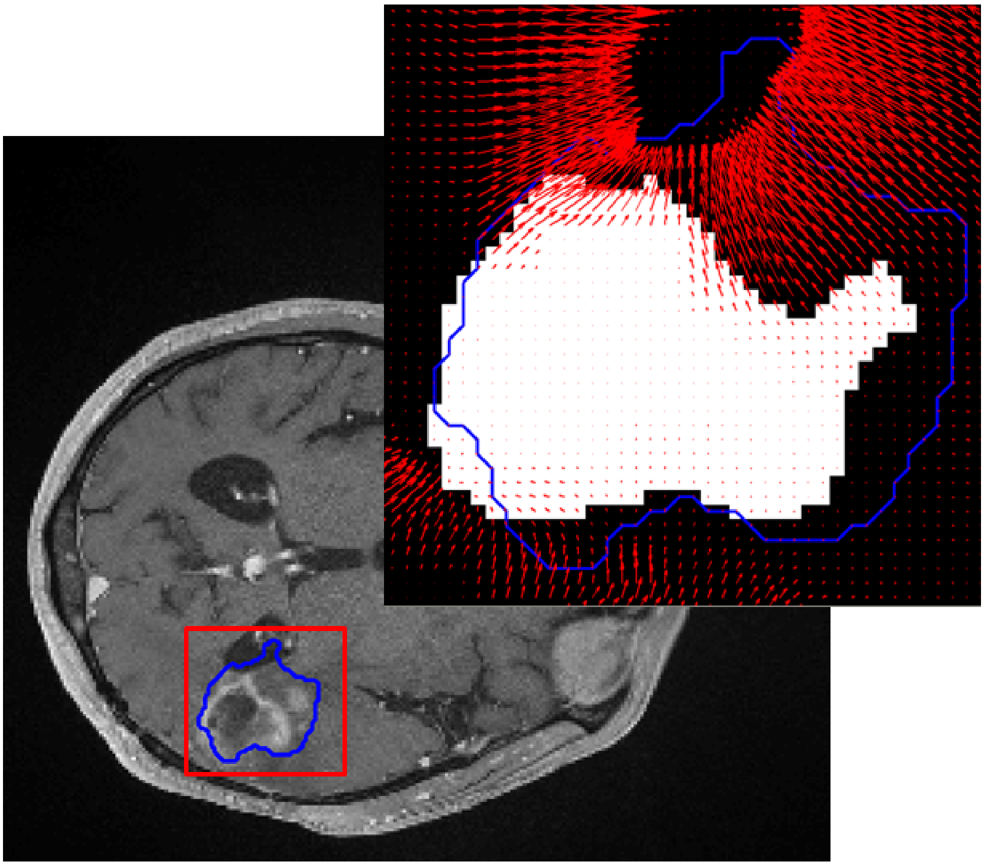

Figure 5.9: A closer look to the tumor where the baseline tumor volume is labeled with white color, the follow-up tumor boundary is indicated with blue contour and the displacement field is overlayed with red arrows.

Chapter 6

Summary and Discussion

Advanced image analysis techniques are involved in different stages of both the radiotherapy treatment and follow-up of the brain tumors. Computational methods used in radiation therapy usually involve intra/inter patient registration, segmentation and tumor growth modeling, whereas, tumor follow-up involves intra/inter patient and longitudinal registration, segmentation and change quantification steps.

In this thesis, image analysis techniques are developed for planning the image guided radiotherapy and follow-up of the treatment responses. Three main parts of the thesis are: Segmentation of brain tumors on MRI, deformable registration of brain MRI volumes with tumors, and change quantification in temporal MRI series of brain tumors.

The "Tumor-cut" method, developed for segmentation of brain tumors on MR images, performed superior for some subsets of the multimodal tumor database and comparable to the state-of-the-art techniques for the remainders. Local response criteria, proposed by using the invariants of the Lagrange strain tensor, resulted in measures more consistent with the clinical outcome than volumetric measurements. The deformable registration method based on a novel approach, including regularization using hyper-elastic mechanical models and tumor exclusion, resulted in displacement fields consistent with the finite element simulations. Application on real tumor case reveals the potential of our method to quantify healthy tissue deformations due to the tumor mass effect.

Although, the results on solid tumors obtained by fully or semi-automatic methods are greatly improved recently with region based and machine learning approaches, improvement of the accuracy and robustness of multi-modal brain tumor segmentation methods, especially in the presence of the surgical cavity, remains as a challenge for the field. A multi-modal "Tumor-cut" idea, where the transition rules are devised using information from different MR intensities, could be developed for a multi-label tumor segmentation. Segmentation of organs at risk (OAR) is still a developing field, not only by more precise definition of the current OAR but also by addition of new structure definitions using advanced imaging modalities (i.e. subcortical regions by functional magnetic resonance imaging, fiber tracks by diffusion MR imaging) and image analysis techniques (i.e. hippocampus segmentation using shape priors [82]).

Improvement of the irradiation dose planning, to better cure the pathology and protect the healthy tissue, is a major research area including advanced functional imaging and mathematical modeling of the tumor evolution. Ongoing studies on techniques, such as tumor growth modeling/simulation [67] or advanced imaging modalities (i.e. Positron Emission Tomography, spectroscopy, diffusion MR imaging, perfusion MR imaging) allow a better understanding of the tumor characteristics hence the improvement of the irradiation margins.

Both, registration of the intra-patient longitudinal images and spatial normalization in the presence of the tumor lesion are hot research topics due to both intensity differences in lesion area and deformation of the healthy tissue caused by the mass effect of the tumor. An open problem which might help to segment OAR automatically and more accurately is deformable registration of the brains to the population atlases in the presence of the tumor. This also allows better understanding and categorization of the tumors by creating tumor probability atlases. Furthermore, target tracking during therapy is another area in which methods including optical tracking and registration of intra-therapy x-ray images are involved depending on the radiotherapeutic hardware [83].

Better visualization and quantification of the local changes of the tumor evolution is an open problem, which requires both understanding the clinical needs and developing mathematical techniques to meet those requirements. Local tumor response measures based on deformation tensor invariants, proposed in this thesis, show promise for quantification of tumor response to therapy and relation to clinical outcome, which should be further explored over larger data sets.

Appendix A

Definitions and Conversions of Overlap Measures

Most commonly used measures to report segmentation overlap results in brain tumor segmentation literature are Dice Overlap (D), Jaccard Index (J), False Positive and Negative Volume Fraction (FPVF, FNVF) pairs. Dice Overlap (D) between two label sets A and B is defined as:

$$D(A,B) = 2 \times \frac{s(A \cap B)}{s(A) + s(B)} \tag{A.0.1}$$

where $s(A)$ denotes the cardinality of a set A. Jaccard Index (J) of two sets A and B is defined as:

$$J(A,B) = \frac{s(A \cap B)}{s(A \cup B)} \tag{A.0.2}$$

and could be converted to Dice Overlap score by:

$$D(A,B) = 2 \times \frac{J(A,B)}{1 + J(A,B)} \tag{A.0.3}$$

False Positive Volume Fractions (FPVF) and False Negative Volume Fractions (FNVF) of a segmentation (A) and a ground truth (M) are defined as:

$$FPVF(M,A) = \frac{s(A - M)}{s(M)} \quad FNVF(M,A) = \frac{s(M - A)}{s(M)} \tag{A.0.4}$$

and can be converted to Jaccard Index as:

$$J(M,A) = \frac{1 - FNVF(M,A)}{1 + FPVF(M,A)} \tag{A.0.5}$$

Similarly, Sensitivity and Specificity of a segmentation (A) and a ground truth (M) are defined as:

$$Sensitivity(M,A) = \frac{s(M \cap A)}{s(M)} \quad Specificity(M,A) = \frac{s(M^{\complement} \cap A^{\complement})}{s(M^{\complement})} \tag{A.0.6}$$

Appendix B

Euler-Lagrange Condition of the Neo-Hookean Energy Function

The decoupled form of the neo-Hookean strain energy model is given as:

$$W = \frac{\mu}{2}(\frac{Tr(B)}{J^{2/3}} - 3) + \frac{1}{D_1}(J-1)^2 \tag{B.0.1}$$

where the deformation gradient tensor is $F_{ij} = \frac{\partial u_i}{\partial x_j} + \delta_{ij}$, $B = FF^T$ and J is the determinant of the deformation $J = det(F)$.

The derivation of the corresponding Euler-Lagrange condition requires the following term to be evaluated:

$$-\sum_j \frac{\partial}{\partial x_j} \frac{\partial W}{\partial F_{ij}} \tag{B.0.2}$$

Starting with the chain rule:

$$\frac{\partial W}{\partial F_{ij}} = \frac{\partial W}{\partial Tr(B)} \frac{\partial Tr(B)}{\partial F_{ij}} + \frac{\partial W}{\partial J} \frac{\partial J}{\partial F_{ij}} \tag{B.0.3}$$

The trace of B can be written in terms of F as:

$$Tr(B) = \sum_i B_{ii} = \sum_i \sum_j F_{ij} F_{ij} = \sum_i \sum_j F_{ij}^2 \tag{B.0.4}$$

The derivative $\frac{\partial Tr(B)}{\partial F_{ij}}$'s can be calculated using Eq. B.0.4:

$$\frac{\partial Tr(B)}{\partial F_{ij}} = 2F_{ij} \tag{B.0.5}$$

The derivative $\frac{\partial J}{\partial F_{ij}}$'s can be calculated using :

$$\frac{\partial det(F)}{\partial F_{ij}} = det(F)(F^{-1})_{ji} \tag{B.0.6}$$

The Euler-Lagrange term becomes:

$$-\sum_j \frac{\partial}{\partial x_j} \frac{\partial W}{\partial F_{ij}} = -\sum_j \frac{\partial}{\partial x_j} (\frac{\mu}{J^{2/3}} F_{ij} - \frac{\mu}{3} \frac{Tr(B)}{J^{2/3}} (F^{-1})_{ji}$$
$$+ \frac{2J(J-1)}{D1} (F^{-1})_{ji}) \tag{B.0.7}$$

$$-\sum_j \frac{\partial}{\partial x_j}\frac{\partial W}{\partial F_{ij}} = -\mu \sum_j \frac{\partial}{\partial x_j} J^{-2/3} F_{ij} + \frac{\mu}{3}\sum_j \frac{\partial}{\partial x_j} Tr(B) J^{-2/3} (F^{-1})_{ji} \\ -\frac{2}{D1}\sum_j \frac{\partial}{\partial x_j} J(J-1)(F^{-1})_{ji} \quad \text{(B.0.8)}$$

$$-\sum_j \frac{\partial}{\partial x_j}\frac{\partial W}{\partial F_{ij}} = -\mu J^{-2/3}\sum_j \frac{\partial}{\partial x_j} F_{ij} - \mu \sum_j F_{ij}\frac{\partial}{\partial x_j} J^{-2/3} \\ +\frac{\mu}{3} Tr(B) J^{-2/3} \sum_j \frac{\partial}{\partial x_j}(F^{-1})_{ji} + \frac{\mu}{3} Tr(B) \sum_j (F^{-1})_{ji} \frac{\partial}{\partial x_j} J^{-2/3} \\ +\frac{\mu}{3} J^{-2/3} \sum_j (F^{-1})_{ji} \frac{\partial}{\partial x_j} Tr(B) \\ -\frac{2}{D1} J(J-1)\sum_j \frac{\partial}{\partial x_j}(F^{-1})_{ji} - \frac{2}{D1}\sum_j (F^{-1})_{ji}) \frac{\partial}{\partial x_j} J(J-1) \quad \text{(B.0.9)}$$

$$-\sum_j \frac{\partial}{\partial x_j}\frac{\partial W}{\partial F_{ij}} = -\mu J^{-2/3}\sum_j \frac{\partial F_{ij}}{\partial x_j} + \frac{2\mu}{3J^{5/3}} \sum_j F_{ij}\frac{\partial}{\partial x_j} J \\ +\frac{\mu}{3} Tr(B) J^{-2/3} \sum_j \frac{\partial}{\partial x_j}(F^{-1})_{ji} - \frac{2\mu}{9J^{5/3}} Tr(B) \sum_j (F^{-1})_{ji} \frac{\partial}{\partial x_j} J \\ +\frac{\mu}{3} J^{-2/3} \sum_j (F^{-1})_{ji} Tr(\frac{\partial}{\partial x_j} F F^T) \\ -\frac{2}{D1} J(J-1)\sum_j \frac{\partial}{\partial x_j}(F^{-1})_{ji} - \frac{2(2J-1)}{D1}\sum_j (F^{-1})_{ji} \frac{\partial}{\partial x_j} J \quad \text{(B.0.10)}$$

We utilize the following matrix derivatives:

$$\frac{\partial}{\partial x} det(F) = det(F) Tr[F^{-1}\frac{\partial F}{\partial x}] \quad \text{(B.0.11)}$$

$$\frac{\partial}{\partial x} F^{-1} = -F^{-1}\frac{\partial F}{\partial x} F^{-1} \quad \text{(B.0.12)}$$

Inserting Eq. B.0.11 into Eq. B.0.10, we get:

$$\begin{aligned}
-\sum_j \frac{\partial}{\partial x_j}\frac{\partial W}{\partial F_{ij}} = & -\frac{\mu}{J^{2/3}}\sum_j \frac{\partial F_{ij}}{\partial x_j} + \frac{2\mu}{3J^{2/3}}\sum_j F_{ij}Tr(F^{-1}\frac{\partial F}{\partial x_j}) \\
& +\frac{\mu Tr(B)}{3J^{2/3}}\sum_j \frac{\partial}{\partial x_j}(F^{-1})_{ji} - \frac{2\mu Tr(B)}{9J^{2/3}}\sum_j (F^{-1})_{ji}Tr(F^{-1}\frac{\partial F}{\partial x_j}) \\
& +\frac{2\mu}{3J^{2/3}}\sum_j (F^{-1})_{ji}Tr(\frac{\partial F}{\partial x_j}F^T) \\
& -\frac{2J(J-1)}{D1}\sum_j \frac{\partial}{\partial x_j}(F^{-1})_{ji} - \frac{2J(2J-1)}{D1}\sum_j (F^{-1})_{ji}Tr(F^{-1}\frac{\partial F}{\partial x_j}) \qquad \text{(B.0.13)}
\end{aligned}$$

Inserting Eq. B.0.12 into Eq. B.0.13, we obtain the resulting update equation in Eq. 5.23.

Appendix C

Euler-Lagrange Condition of the Volumetric Term

The volumetric part of the strain energy can be given as:

$$W_{vol} = \frac{K}{2}(lnJ)^2 \tag{C.0.1}$$

where J is the determinant of the deformation F.

The corresponding term in Euler-Lagrange condition is derived as:

$$\begin{aligned}
-\sum_j \frac{\partial}{\partial x_j}\frac{\partial W}{\partial F_{ij}} &= -\sum_j \frac{\partial}{\partial x_j}\frac{\partial}{\partial F_{ij}}\frac{K}{2}(lnJ)^2 \\
-\sum_j \frac{\partial}{\partial x_j}\frac{\partial W}{\partial F_{ij}} &= -\frac{K}{2}\sum_j \frac{\partial}{\partial x_j}\frac{2lnJ}{J}\frac{\partial J}{\partial F_{ij}} \\
-\sum_j \frac{\partial}{\partial x_j}\frac{\partial W}{\partial F_{ij}} &= -\frac{K}{2}\sum_j \frac{\partial}{\partial x_j}\frac{2lnJ}{J}J(F^{-1})_{ji} \\
-\sum_j \frac{\partial}{\partial x_j}\frac{\partial W}{\partial F_{ij}} &= -K\sum_j \frac{\partial}{\partial x_j}lnJ(F^{-1})_{ji} \\
-\sum_j \frac{\partial}{\partial x_j}\frac{\partial W}{\partial F_{ij}} &= -K\sum_j((F^{-1})_{ji}\frac{\partial lnJ}{\partial x_j} + lnJ\frac{\partial}{\partial x_j}(F^{-1})_{ji}) \\
-\sum_j \frac{\partial}{\partial x_j}\frac{\partial W}{\partial F_{ij}} &= -K\sum_j(F^{-1})_{ji}\frac{1}{J}\frac{\partial J}{\partial x_j} - KlnJ\sum_j \frac{\partial}{\partial x_j}(F^{-1})_{ji} \\
-\sum_j \frac{\partial}{\partial x_j}\frac{\partial W}{\partial F_{ij}} &= -K\sum_j(F^{-1})_{ji}\frac{1}{J}JTr[F^{-1}\frac{\partial F}{\partial x_j}] + KlnJ\sum_j(F^{-1}\frac{\partial F}{\partial x_j}F^{-1})_{ji} \\
-\sum_j \frac{\partial}{\partial x_j}\frac{\partial W}{\partial F_{ij}} &= -K\sum_j(F^{-1})_{ji}Tr[F^{-1}\frac{\partial F}{\partial x_j}] + KlnJ\sum_j(F^{-1}\frac{\partial F}{\partial x_j}F^{-1})_{ji}
\end{aligned} \tag{C.0.2}$$

Appendix D

Euler-Lagrange Condition of the Log Barrier

Log-barrier energy term is given as:

$$W = -\lambda lnJ \tag{D.0.1}$$

where J is the determinant of the deformation F.

The corresponding term in euler-lagrange condition is derived as:

$$\begin{aligned}
-\sum_j \frac{\partial}{\partial x_j}\frac{\partial W}{\partial F_{ij}} &= -\sum_j \frac{\partial}{\partial x_j}\frac{\partial}{\partial F_{ij}}(-\lambda lnJ) \\
-\sum_j \frac{\partial}{\partial x_j}\frac{\partial W}{\partial F_{ij}} &= \lambda \sum_j \frac{\partial}{\partial x_j} J^{-1}\frac{\partial J}{\partial F_{ij}} \\
-\sum_j \frac{\partial}{\partial x_j}\frac{\partial W}{\partial F_{ij}} &= \lambda \sum_j \frac{\partial}{\partial x_j} J^{-1} J (F^{-1})_{ji} \\
-\sum_j \frac{\partial}{\partial x_j}\frac{\partial W}{\partial F_{ij}} &= \lambda \sum_j \frac{\partial}{\partial x_j} (F^{-1})_{ji} \\
-\sum_j \frac{\partial}{\partial x_j}\frac{\partial W}{\partial F_{ij}} &= -\lambda \sum_j (F^{-1}\frac{\partial F}{\partial x_j}F^{-1})_{ji}
\end{aligned} \tag{D.0.2}$$

Bibliography

[1] T. Vercauteren, X. Pennec, A. Perchant, and N. Ayache, “Diffeomorphic demons: Efficient non-parametric image registration.” *Neuroimage*, 2008.

[2] M. Prastawa, E. Bullitt, and G. Gerig, “Synthetic ground truth for validation of brain tumor mri segmentation,” in *MICCAI, LNCS 3749*. Springer, 2005, pp. 26–33.

[3] L. M. DeAngelis, “Brain tumors,” *N Engl J Med*, vol. 344, no. 2, pp. 114–123, 2001.

[4] S. Bauer, R. Wiest, L.-P. Nolte, and M. Reyes, “A survey of mri-based medical image analysis for brain tumor studies,” *Physics in Medicine and Biology*, vol. 58, no. 13, p. R97, 2013.

[5] D. Louis, W. H. Organization, H. Ohgaki, and I. A. for Research on Cancer, *WHO Classification of Tumours of the Central Nervous System*. International Agency for Research on Cancer, 2007.

[6] T. Scarabino, *Imaging Gliomas After Treatment: A Case-based Atlas*. Springer, 2012.

[7] R. Rampling, A. James, and V. Papanastassiou, “The present and future management of malignant brain tumours: surgery, radiotherapy, chemotherapy,” *Journal of Neurology, Neurosurgery Psychiatry*, vol. 75, no. suppl 2, pp. ii24–ii30, 2004.

[8] D. Zikic, B. Glocker, E. Konukoglu, A. Criminisi, C. Demiralp, J. Shotton, O. Thomas, T. Das, R. Jena, and S. Price, “Decision forests for tissue-specific segmentation of high-grade gliomas in multi-channel mr,” in *Medical Image Computing and Computer-Assisted Intervention MICCAI 2012*, ser. Lecture

Notes in Computer Science. Springer Berlin Heidelberg, 2012, vol. 7512, pp. 369–376.

[9] E. D. Angelini, O. Clatz, E. Mandonnet, E. Konukoglu, L. Capelle, and H. Duffau, “Glioma dynamics and computational models: A review of segmentation, registration, and in silico growth algorithms and their clinical applications,” *Current Medical Imaging Reviews*, vol. 3, no. 4, pp. 262–276, 2007.

[10] G. Shah, S. Kesari, R. Xu, T. Batchelor, A. O’neill, F. Hochberg, B. Levy, J. Bradshaw, and P. Wen, “Comparison of linear and volumetric criteria in assessing tumor response in adult high-grade gliomas.” *Neuro-oncol*, vol. 8, no. 1, pp. 38–46, 2006.

[11] D. Macdonald, T. Cascino, S. Schold Jr, and J. Cairncross, “Response criteria for phase ii studies of supratentorial malignant glioma.” *J Clin Oncol*, vol. 8, no. 7, pp. 1277–80, 1990.

[12] P. Y. Wen, D. R. Macdonald, D. A. Reardon, T. F. Cloughesy, A. G. Sorensen, E. Galanis, J. DeGroot, W. Wick, M. R. Gilbert, A. B. Lassman, C. Tsien, T. Mikkelsen, E. T. Wong, M. C. Chamberlain, R. Stupp, K. R. Lamborn, M. A. Vogelbaum, M. J. van den Bent, and S. M. Chang, “Updated response assessment criteria for high-grade gliomas: Response assessment in neuro-oncology working group,” *Journal of Clinical Oncology*, vol. 28, no. 11, pp. 1963–1972, 2010.

[13] E. Konukoglu, W. Wells, S. Novellas, N. Ayache, R. Kikinis, P. Black, and K. Pohl, “Monitoring slowly evolving tumors,” in *In Proceedings of the IEEE Internation Symposium on Biomedical Imaging: From Nano to Macro (ISBI’08)*, Paris, France, May 2008.

[14] M. Cabezas, A. Oliver, X. Lladó, J. Freixenet, and M. Bach Cuadra, “A review of atlas-based segmentation for magnetic resonance brain images,” *Comput. Methods Prog. Biomed.*, vol. 104, no. 3, pp. e158–e177, 2011.

[15] E. Zacharaki, D. Shen, S. Lee, and C. Davatzikos, “Orbit: a multiresolution framework for deformable registration of brain tumor images,” *IEEE Trans Med Imaging*, vol. 27, no. 8, pp. 1003–17, 2008.

[16] C. Davatzikos, E. Zacharaki, A. Gooya, and V. Clark, "Multi-parametric analysis and registration of brain tumors: constructing statistical atlases and diagnostic tools of predictive value," *Conf Proc IEEE Eng Med Biol Soc*, vol. 2011, 2011.

[17] M. Brett, A. Leff, C. Rorden, and J. Ashburner, "Spatial normalization of brain images with focal lesions using cost function masking," *NeuroImage*, vol. 14, no. 2, pp. 486–500, 2001.

[18] A. Gooya, G. Biros, and C. Davatzikos, "Deformable registration of glioma images using em algorithm and diffusion reaction modeling," *Medical Imaging, IEEE Transactions on*, vol. 30, no. 2, pp. 375 –390, feb. 2011.

[19] S. Warfield, K. Zou, and W. Wells, "Simultaneous truth and performance level estimation (staple): An algorithm for the validation of image segmentation," *IEEE Trans. Med Imaging*, vol. 23, no. 7, pp. 903 – 921, 2004.

[20] M.-R. Nazem-Zadeh, E. Davoodi-Bojd, and H. Soltanian-Zadeh, "Atlas-based fiber bundle segmentation using principal diffusion directions and spherical harmonic coefficients," *NeuroImage*, vol. 54, Supplement 1, no. 0, pp. S146 – S164, 2011.

[21] K. H. Zou, S. K. Warfield, A. Bharatha, C. M. C. Tempany, M. R. Kaus, S. J. Haker, W. M. Wells, F. A. Jolesz, and R. Kikinis, "Statistical validation of image segmentation quality based on a spatial overlap index," *Academic Radiology*, vol. 11, no. 2, pp. 178 – 189, 2004.

[22] M. Prastawa, E. Bullitt, S. Ho, and G. Gerig, "A brain tumor segmentation framework based on outlier detection," *Medical Image Analysis*, vol. 8, no. 3, pp. 275–283, 2004.

[23] J. Liu, J. K. Udupa, D. Odhner, D. Hackney, and G. Moonis, "A system for brain tumor volume estimation via mr imaging and fuzzy connectedness," *Computerized Medical Imaging and Graphics*, vol. 29, no. 1, pp. 21 – 34, 2005.

[24] T. Biswas, P. Okunieff, M. C. Schell, T. Smudzin, W. H. Pilcher, R. S. Bakos, G. E. Vates, K. A. Walter, A. Wensel, D. N. Korones, and et al., "Stereotac-

tic radiosurgery for glioblastoma: retrospective analysis." *Radiation Oncology*, vol. 4, no. 11, p. 11, 2009.

[25] B. H. Menze, K. Van Leemput, D. Lashkari, M.-A. Weber, N. Ayache, and P. Golland, "A generative model for brain tumor segmentation in multi-modal images," in *Medical Image Computing and Computer-Assisted Intervention (MICCAI'10)*, ser. LNCS. Beijing, China: Springer, September 2010.

[26] T. F. Chan and L. Vese, "Active contours without edges," *"IEEE Transactions on Image Processing"*, vol. 10, no. 2, pp. 266–277, 2001.

[27] S.Ho, E.Bullitt, and G.Gerig, "Level-set evolution with region competition: Automatic 3-d segmentation of brain tumors," *ICPR*, vol. 1, p. 10532, 2002.

[28] Y. Boykov and M.-P. Jolly, "Interactive graph cuts for optimal boundary and region segmentation of objects in n-d images," in *ICCV*, 2001, pp. 105–112.

[29] L. Grady, "Random walks for image segmentation," *PAMI*, vol. 28, no. 11, pp. 1768 – 1783, 2006.

[30] C. Couprie, L. Grady, L. Najman, and H. Talbot, "Power watersheds: A new image segmentation framework extending graph cuts, random walker and optimal spanning forest," in *ICCV*, 2009.

[31] A. Sinop and L. Grady, "A seeded image segmentation framework unifying graph cuts and random walker which yields a new algorithm," in *ICCV*, 2007.

[32] A. Criminisi, T. Sharp, and A. Blake, "GeoS: Geodesic Image Segmentation," in *Computer Vision ECCV 2008*, vol. 5302, 2008, pp. 99–112.

[33] X. Bai and G. Sapiro, "Geodesic matting: A framework for fast interactive image and video segmentation and matting," *International Journal of Computer Vision*, vol. 82, pp. 113–132, 2009.

[34] R. Szeliski, R. Zabih, D. Scharstein, O. Veksler, V. Kolmogorov, A. Agarwala, M. Tappen, and C. Rother, "A comparative study of energy minimization methods for markov random fields with smoothness-based priors," *IEEE Trans. Pattern Anal. Mach. Intell.*, vol. 30, pp. 1068–1080, 2008.

[35] V.Vezhnevets and V.Konouchine, “Growcut - interactive multi-label n-d image segmentation by cellular automata,” in *Graphicon*, Novosibirsk Akademgorodok, Russia, 2005.

[36] A. Popovici and D. Popovici, “Cellular automata in image processing,” in *15th International Symposium on the Mathematical Theory of Networks and Systems*, Indiana, USA, 2002.

[37] J. V. Neumann, *Theory of Self-Reproducing Automata*, A. W. Burks, Ed. Champaign, IL, USA: University of Illinois Press, 1966.

[38] N. Ganguly, B. K. Sikdar, A. Deutsch, G. Canright, and P. P. Chaudhuri, “A survey on cellular automata,” Centre for High Performance Computing, Dresden University of Technology, Dresden, Germany, Tech. Rep., 2003.

[39] J. Kari, “Theory of cellular automata: A survey,” *Theoretical Computer Science*, vol. 334, no. 1-3, pp. 3 – 33, 2005.

[40] K. Kaneko, “Overview of coupled map lattices,” *Chaos*, vol. 2, no. 3, pp. 279–282, 1992.

[41] D. N. Ostrov and R. Rucker, “Continuous-valued cellular automata for nonlinear wave equations,” *Complex Systems*, vol. 10, pp. 91 – 119, 1996.

[42] S. Wolfram, *A New Kind of Science.* Wolfram Media, 2002, ch4-p155.

[43] A. Hamamci, G. Unal, N. Kucuk, and K. Engin, “Cellular automata segmentation of brain tumors on post contrast mr images,” in *MICCAI, LNCS 6363.* Beijing, China: Springer, 2010, pp. 137–146.

[44] C. Kauffmann and N. Pich, “Seeded nd medical image segmentation by cellular automaton on gpu,” *International Journal of Computer Assisted Radiology and Surgery*, vol. 5, pp. 251–262, 2010.

[45] G. Hernandez and H. J. Herrmann, “Cellular automata for elementary image enhancement,” *Graphical Models And Image Processing*, vol. 58, no. 1, pp. 82–89, 1996.

[46] C. Alvino, G. Unal, G. Slabaugh, B. Peny, and T. Fang, “Efficient segmentation based on eikonal and diffusion equations,” *Int. J. Comput. Math.*, vol. 84, pp. 1309–1324, September 2007.

[47] P. Therasse, “Evaluation of response: new and standard criteria,” *Annals of Oncology*, vol. 13, pp. 127 – 129, 2002.

[48] L. S. Chin, L. Ma, and S. DiBiase, “Radiation necrosis following gamma knife surgery: a case-controlled comparison of treatment parameters and long-term clinical follow up,” *Journal of Neurosurgery*, vol. 94, no. 6, pp. 899–904, 2001.

[49] A. P. Dempster, N. M. Laird, and D. B. Rubin, “Maximum likelihood from incomplete data via the em algorithm,” *Journal of the Royal Statistical Society, Series B*, vol. 39, no. 1, pp. 1–38, 1977.

[50] N. Otsu, “A threshold selection method from gray level histograms,” *IEEE Trans. Systems, Man and Cybernetics*, vol. 9, pp. 62–66, Mar. 1979.

[51] N. Archip, F. Jolesz, and S. Warfield, “A validation framework for brain tumor segmentation,” *Acad Radiol.*, vol. 14, no. 10, pp. 1242 – 1251, 2007.

[52] E. Eisenhauer, P. Therasse, J. Bogaerts, L. Schwartz, D. Sargent, R. Ford, J. Dancey, S. Arbuck, S. Gwyther, M. Mooney, L. Rubinstein, L. Shankar, L. Dodd, R. Kaplan, D. Lacombe, and J. Verweij, “New response evaluation criteria in solid tumours: Revised recist guideline (version 1.1),” *European journal of cancer*, vol. 45, issue 2, pp. 228–247, 2009.

[53] A. Hamamci, N. Kucuk, K. Karaman, K. Engin, and G. Unal, “Tumor-cut: Segmentation of brain tumors on contrast enhanced mr images for radiosurgery applications,” *Medical Imaging, IEEE Transactions on*, vol. 31, no. 3, pp. 790 –804, march 2012.

[54] W. H. Organization, *Handbook for Reporting Results of Cancer Treatment.* Geneva: Offset Publication, 1979.

[55] A. Miller, “Reporting results of cancer treatment,” *Cancer*, vol. 47, pp. 207–14, 1981.

[56] J. Park, S. Lee, S. Song, K. Kim, W. Kim, C. Jung, Y. Park, Y. Im, W. Kang, M. Lee, K. Lee, and K. Park, “Measuring response in solid tumors: Comparison of recist and who response criteria.” *Jpn J Clin Oncol*, vol. 33, no. 10, pp. 533–7, 2003.

[57] Y. Tsuchida and P. Therasse, “Response evaluation criteria in solid tumors (recist): new guidelines.” *Med Pediatr Oncol*, vol. 37, no. 1, pp. 1–3, 2001.

[58] K. James, E. Eisenhauer, M. Christian, M. Terenziani, D. Vena, A. Muldal, and P. Therasse, “Measuring response in solid tumors: unidimensional versus bidimensional measurement.” *J Natl Cancer Inst*, vol. 91, no. 6, pp. 523–8, 1999.

[59] P. Therasse, S. Arbuck, E. Eisenhauer, J. Wanders, R. Kaplan, L. Rubinstein, J. Verweij, M. Van Glabbeke, A. van Oosterom, M. Christian, and S. Gwyther, “New guidelines to evaluate the response to treatment in solid tumors. european organization for research and treatment of cancer, national cancer institute of the united states, national cancer institute of canada.” *J Natl Cancer Inst*, vol. 92, no. 3, pp. 205–16, 2000.

[60] W. Shi, D. Wildrick, and R. Sawaya, “Volumetric measurement of brain tumors from mr imaging.” *J Neurooncol*, vol. 37, no. 1, pp. 87–93, 1998.

[61] A. Demir, G. Unal, and K. Karaman, “Anatomical landmark based registration of contrast enhanced t1-weighted mr images,” in *Proceedings of the 4th international conference on Biomedical image registration*, ser. WBIR’10. Berlin, Heidelberg: Springer-Verlag, 2010, pp. 91–103.

[62] J.-P. Thirion, “Image matching as a diffusion process: an analogy with maxwell’s demons,” *Medical Image Analysis*, vol. 2, no. 3, pp. 243 – 260, 1998. [Online]. Available: http://www.sciencedirect.com/science/article/pii/S1361841598800224

[63] A. F. Bower, *Applied Mechanics of Solids.* Taylor and Francis Group, LLC, 2010.

[64] M. Reuter, H. D. Rosas, and B. Fischl, "Highly accurate inverse consistent registration: a robust approach." *NeuroImage*, vol. 53, no. 4, pp. 1181–1196, 2010.

[65] S. Periaswamy and H. Farid, "Elastic registration with partial data," *Proc of Workshop on Biomedical Image Registration WBIR03*, pp. 102–111, 2003.

[66] C. Hogea, G. Biros, F. Abraham, and C. Davatzikos, "A robust framework for soft tissue simulations with application to modeling brain tumor mass effect in 3d mr images," *Physics in Medicine and Biology*, vol. 52, no. 23, p. 6893, 2007.

[67] E. Konukoglu, O. Clatz, P.-Y. Bondiau, H. Delingette, and N. Ayache, "Extrapolating glioma invasion margin in brain magnetic resonance images: suggesting new irradiation margins." *Medical Image Analysis*, vol. 14, no. 2, pp. 111–125, 2010.

[68] O. Clatz, M. Sermesant, P.-Y. Bondiau, H. Delingette, S. Warfield, G. Malandain, and N. Ayache, "Realistic simulation of the 3d growth of brain tumors in mr images coupling diffusion with biomechanical deformation," *IEEE Trans Med Imaging*, vol. 24, no. 10, pp. 1334–1346, 10 2005.

[69] M. Prastawa, E. Bullitt, and G. Gerig, "Simulation of brain tumors in mr images for evaluation of segmentation efficacy," *Medical Image Analysis*, vol. 13, no. 2, pp. 297 – 311, 2009.

[70] M. Niethammer, G. Hart, D. Pace, and S. Aylward, "Geometric metamorphosis," in *MICCAI*, 2011.

[71] K. Miller and K. Chinzei, "Mechanical properties of brain tissue in tension," *Journal of Biomechanics*, vol. 35, no. 4, pp. 483 – 490, 2002.

[72] G. R. Joldes, A. Wittek, and K. Miller, "Suite of finite element algorithms for accurate computation of soft tissue deformation for surgical simulation," *Medical Image Analysis*, vol. 13, no. 6, pp. 912 – 919, 2009.

[73] A. Wittek, K. Miller, R. Kikinis, and S. K. Warfield, "Patient-specific model of brain deformation: Application to medical image registration," *Journal of Biomechanics*, vol. 40, no. 4, pp. 919 – 929, 2007.

[74] A. Mohamed and C. Davatzikos, "Finite element modeling of brain tumor mass-effect from 3d medical images," in *Proceedings of the 8th international conference on Medical Image Computing and Computer-Assisted Intervention - Volume Part I*, ser. MICCAI'05. Berlin, Heidelberg: Springer-Verlag, 2005, pp. 400–408.

[75] I. Yanovsky, C. Le Guyader, A. Leow, A. Toga, W., P. Thompson, M., and L. Vese, "Unbiased Volumetric Registration via Nonlinear Elastic Regularization," in *2nd MICCAI Workshop on Mathematical Foundations of Computational Anatomy*, X. Pennec, Ed., New-York, États-Unis, Oct. 2008.

[76] A. Wittek, T. Hawkins, and K. Miller, "On the unimportance of constitutive models in computing brain deformation for image-guided surgery," *Biomechanics and Modeling in Mechanobiology*, vol. 8, pp. 77–84, 2009.

[77] P. Pedregal, *Variational methods in nonlinear elasticity.* Philadelphia, PA, USA: Society for Industrial and Applied Mathematics, 2000.

[78] G. Holzapfel, *Nonlinear Solid Mechanics: A Continuum Approach for Engineering.* John Wiley & Sons, 2000.

[79] M. C. Boyce and E. M. Arruda, "Constitutive models of rubber elasticity: a review," *Rubber Chem. Technol.*, vol. 73, pp. 505–523, 2000.

[80] B. A. Hamza, H. Krim, and G. B. Unal, "Unifying probabilistic and variational estimation," *Signal Processing Magazine*, vol. 19, no. 5, pp. 37–47, 2002.

[81] S. A. Maas, G. A. Ateshian, J. A. Weiss, and B. J. Ellis, "Febio: Finite elements for biomechanics," *Journal of Biomechanical Engineering*, vol. 134, no. 1, pp. 011 005–10, 1999.

[82] D. Shen, S. Moffat, S. M. Resnick, and C. Davatzikos, "Measuring size and shape of the hippocampus in {MR} images using a deformable shape model," *NeuroImage*, vol. 15, no. 2, pp. 422 – 434, 2002.

[83] A. Schweikard, H. Shiomi, and J. Adler, "Respiration tracking in radiosurgery without fiducials," *The International Journal of Medical Robotics and Computer Assisted Surgery*, vol. 1, no. 2, pp. 19–27, 2005.